Development of 3D Printed Porous Biomaterials

Guoyao Chen

A dissertation

submitted in partial fulfillment of the

requirements for the degree of

Doctor of Philosophy

University of Washington

2024

Reading Committee:

Buddy D. Ratner, Chair

David S. Bergsman

Jorge A. Marchand

Program Authorized to Offer Degree:

Chemical Engineering

University of Washington

Abstract

Development of 3D Printed Porous Biomaterials

Guoyao Chen

Chair of the Supervisory Committee:

Buddy D. Ratner

Chemical Engineering and Bioengineering

Porous biomaterials play an important role in healthcare applications due to their ability to reduce foreign body reactions (FBR). This study investigates the effects of scaffolds with 40 μm spherical pores (6S scaffolds) and 40 μm cubical pores on FBR mitigation. Using stereolithography (SLA), cubical pore scaffolds were fabricated, with a stabilization protocol developed to address internal and surface contamination during the fabrication process. This protocol enhanced print resolution and consistency, allowing for the successful production of scaffolds with intricate geometries and non-linear edges. *In vivo* evaluations indicated that 40 μm cubical pore scaffolds supported tissue regeneration and vascularization while reducing fibrous capsule formation and collagen deposition, comparable to the performance of 6S scaffolds. These findings suggest that 3D-printed 40 μm cubical pores hold the potential for FBR reduction. Additionally, new PEGDMA-based resin formulations for SLA were explored, achieving resolutions of approximately 20 μm. This study presents an SLA-based methodology for producing porous biomaterials with applications in FBR mitigation and tissue engineering, demonstrating the advantage of 3D printing in biomedical applications.

TABLE OF CONTENTS

LIST OF FIGURES

LIST OF TABLES

Chapter 1. BACKGROUND AND MOTIVATION

1.1 BIOMATERIALS AND FOREIGN BODY REACTION

A biomaterial was formally defined by the Clemson University Advisory Board for Biomaterials as *a systematically and pharmacologically inert substance designed for implantation within or incorporation with living systems*[1]. The main objective of utilizing biomaterials is to enhance human health by restoring the natural functions of living tissues and organs within the body[2]. Biomaterials have diverse applications, including but not limited to, contact lenses[3], bone screws[4], insulin pump catheters[5], nerve guidance conduit[6], and cell scaffolds[7-9], which are widely used in tissue engineering. A variety of materials are used in these applications, such as metals[10] and ceramics[11] for hard-tissue biomaterials, and polymers[11, 12] for soft-tissue biomaterials[13]. Biomaterials can also be fabricated into various shapes and structures, including solid[10], porous[13, 14], woven meshes[15], microspheres[16], etc., to suit different purposes.

While dental implants, one of the most common applications of biomaterials, have been used since 600 A.D. in early civilizations[17], the fundamental concepts and principles of the biomaterial field were established within the last century. Prior to the invention of aseptic surgical techniques by Dr. Joseph Lister in the 1860s, most implantations were unsuccessful due to infections[18].

Nowadays, with the advancement of materials and modern surgical techniques, biomaterials have found their applications in many fields, such as regeneration[19, 20] and organ replacement[21]. However, the implantation of biomaterials can induce a variety of host reactions[22], including injury[23], interactions with blood[24], provisional matrix formation[25],

acute and chronic inflammation[26], granulation tissue development[25], foreign body reaction[27], and fibrosis/fibrous capsule development[28]. The foreign body reaction (FBR), which is composed of macrophages and foreign body giant cells, is the end-stage response of the inflammatory and wound healing responses following implantation.

Porous biomaterials have been developed to reduce the FBR and improve integration into host tissue. These materials have interconnected open pores and serve as scaffolds to support cell attachment[29], proliferation[30], and differentiation[31]. The pore structure of the biomaterials is critical in reducing FBR, with pore size, shape, and interconnectivity affecting immune cell infiltration and extracellular matrix deposition[32]. Surface properties of the biomaterials, such as chemical composition[33], wettability[3], and charge[34], also influence the interaction with surrounding tissue, further modulating the FBR. Research in the Ratner lab showed that 40μm porous biomaterials reduced collagen deposition, increased cellular infiltration, and neovascularization, and influenced macrophage phenotype in a size-dependent manner[35].

The fabrication of porous biomaterials involves the creation of interconnected pores within the material structure, allowing for the exchange of nutrients and waste products between cells and the surrounding environment. Various methods exist for developing porous scaffolds, including salt-leaching[36, 37], gas-forming[38, 39], electrospinning[40], freeze-drying[41], and 3D printing[42-44]. Apart from 3D printing, these methods can be considered as utilizing porogens as sacrificial materials that are later removed from the structure to create the pores. The advantage of using porogens is the ability to create a controlled pore size, shape, and distribution within the biomaterial, tailored to specific tissue types or applications. Porogens are also easily removed from the biomaterial, leaving behind a porous structure to support cell attachment, proliferation, and differentiation[45].

However, the use of porogens also has some disadvantages. One major drawback is that the removal of porogens can lead to residual toxic or immunogenic compounds within the biomaterial, which can elicit a negative immune response and impair its biocompatibility[11]. Furthermore, the fabrication process using porogens can be complex and time-consuming, requiring multiple steps and optimization of the porogen concentration, temperature, and exposure time[45].

In contrast, the 3D printing method can be regarded as a direct fabrication approach, allowing for precise control over the size, shape, and distribution of the pores. This method involves the layer-by-layer deposition of material, enabling the creation of intricate and customized structures with high resolution and accuracy. Furthermore, 3D printing can reduce the risk of residual toxins or immunogenic compounds since the material is not in contact with any sacrificial material[46].

1.2 3D Printing of Biomaterials

Three-dimensional (3D) printing, also is known as additive manufacturing (AM), rapid prototyping (RP), or solid free-form technology (SFF), is a potentially powerful manufacturing method and is recognized as a versatile tool for precise fabrication of various devices in many fields including biomedical engineering, wastewater treatment, energy storage, microfluidics and material science[47]. This technique is recognized as a versatile tool for precise manufacturing of various devices. 3D printing can produce complex architecture following a computer-generated design and can be fabricated using a diverse array of materials including polymers[48], metals[49], bio-inks[50], and ceramics[51]. This has led to the development of this technology for biomedical applications in both research and bio-industrial settings. The growing demand for customized pharmaceuticals and medical devices increases the impact of 3D printing, along with the demand for fast and high-resolution manufacturing processes[44].

As of today, the primary 3D printing techniques used in the biomedical field include photopolymerization-based stereolithography (SLA)[52], two-photon polymerization (TPP)[53], digital light processing (DLP)[54], continuous liquid interface production (CLIP)[55], and extrusion-based systems such as ink-jet[56], and fused deposition modeling (FDM)[57].

SLA is regarded as the first rapid prototyping process and was developed in the late 1980s by Charles Hull[58]. SLA uses a .stl file to interpret a computer-aided design file that is communicated electronically to the 3D printer. Photoinitiation triggers monomers and oligomers to cross-link to form polymers[59]. Compared with other 3D printing methods, while most fabrication techniques have a resolution of 50–200μm, many commercially available stereolithography 3D printers can build objects at an accuracy of 20μm or lower[60]. That is why a lot of in laboratory micron-sized structures with sub-micron resolution have been fabricated using these printers[61]. In the Z direction, the layer thickness can reach a resolution at 50μm, but over-curing is an obstacle in maintaining the layer thickness, a challenge for fabricating high-resolution, multi-layer structures.

The study conducted in the Ratner lab has demonstrated that a porous scaffold with 40μm pore size can reduce collagen deposition, increase cellular infiltration, and promote neovascularization[35, 62-65]. The objective of this research project is to investigate the feasibility of printing such a porous scaffold using an SLA 3D printer, and if possible, investigate the performance of the 3D printed scaffolds.

Chapter 2. CREATING STABLE ENVIRONMENTS FOR HIGH-RESOLUTION 3D PRINTING

2.1 INTRODUCTION

Stereolithography (SLA) 3D printing has emerged as a crucial tool in the production of biomedical devices and biomaterials. However, in the case of porous scaffolds, such as those developed by the Ratner Lab, achieving a high level of printing resolution is essential to fabricate the intended structures. To attain high resolution in SLA 3D printing, several key factors must be considered, including the utilization of resins with high-resolution performance, designing 3D models with high accuracy for the printer, and maintaining a stable and precise printing environment[52].

Resins that are specifically designed for high-resolution printing typically have a lower viscosity and a higher level of detail reproduction. They also tend to have a lower shrinkage rate, which helps to prevent distortion and warping during the printing process[66]. The resin DS2000 from DWS is well-designed for SLA 3D printing, so the resin problem is not discussed here.

Blender software is utilized for designing all 3D models for this project. The software is adept at handling intricate structures with varied porous architectures. However, as the resolution and size of the porous scaffold increase, the 3D model may become overly complex for the printer software to manage. Hence, simplifying the printing structure is a common challenge faced in high-resolution 3D printing. We will delve deeper into this issue in chapter 3.

To ensure that the printer consistently produces stable and accurate prints, it is essential to maintain laser accuracy throughout the entire printing process. Any object that blocks the laser during the polymerization process can have a significant impact on the printing results. This

includes factors such as the printing vat condition, resin degradation rate, presence of voids in the 3D structure, and resin reflow. In this part of the study, we focus on how to maintain an optimal printing vat condition.

The KLOE 3D printing system boasts a laser with a spatial resolution of 5μm, which meets the fundamental requirements for high-resolution 3D printing. Figure 2.1 illustrates the schematic diagram of the KLOE 3D printing system, where the resin between the substrate and the polydimethylsiloxane (PDMS) coating is cured by laser during the printing process. As the PDMS can absorb oxygen during the forming process, the oxygen serves as a photo-inhibitor during the printing process, ensuring that the printed object remains on the substrate rather than the PDMS[67]. Clearly, the printing environment, particularly the surface of the substrate and the PDMS, can significantly impact the printing results.

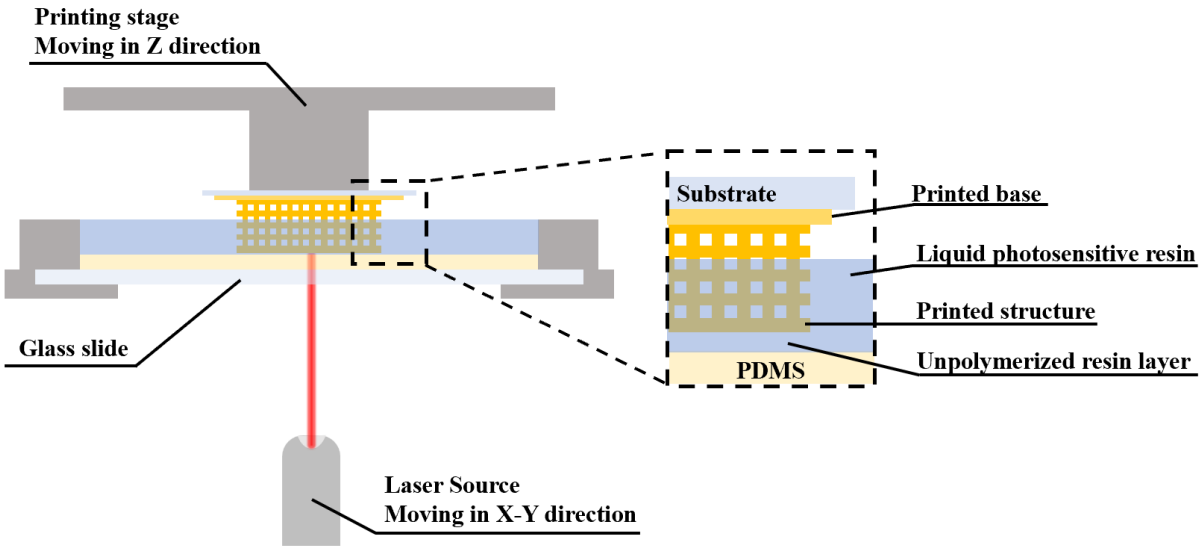

Figure 2.1. schematic diagram of the print stage of the KLOE SLA 3D printer

To ensure the accuracy and consistency of the 3D printing process, three different tests, including sensitivity, focus, and bridge tests, are usually performed on the PDMS coating. However, it has been observed that the test results can vary over time if the same PDMS coating

is continuously used, despite consistent printing parameters. This highlights the importance of stabilizing the PDMS to maintain a stable printing environment. Figure 2.2 demonstrates the significant impact of PDMS status on the sensitivity test results, even with the same printing parameters.

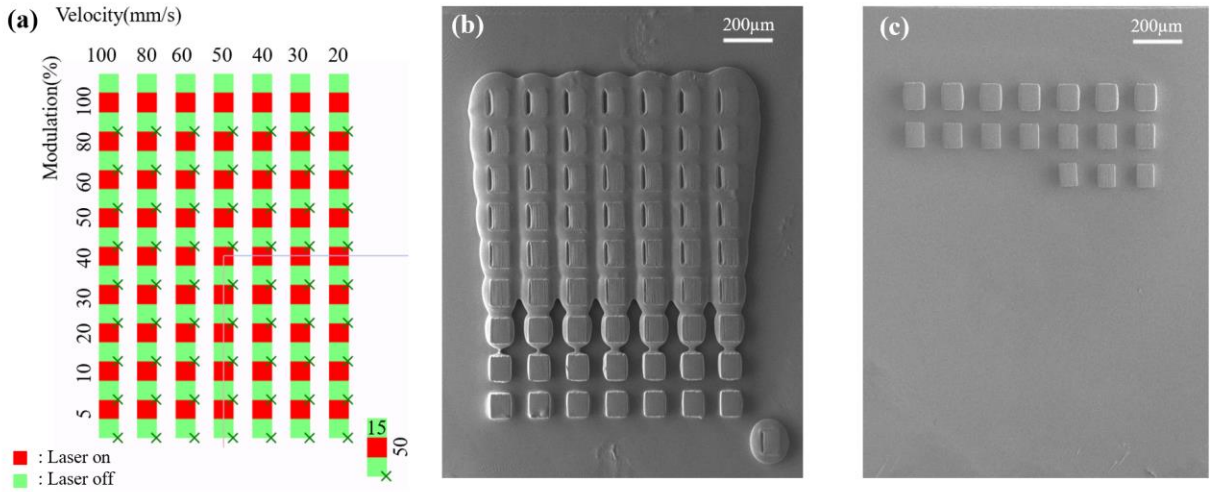

Figure 2.2. (a)Schematic diagram of the sensitivity test, (b) the result with a new PDMS surface and (c) the result the result after repeated reuse of the PDMS

This section of the study aims to identify the main forms of contamination that occur during the printing process and develop methods to address them. Two types of contamination, internal and surface contamination, are frequently observed during experiments. To increase stability and precision in SLA 3D printing, with a focus on improving resolution and generating a stable printing environment with precisely controlled layer thickness, we present a stabilization method for SLA 3D printing using the KLOE high-resolution 3D lithographic laser system as an example.

2.2 METHODS AND MATERIALS

2.2.1 *Design the Porous Structure*

A commercial acrylic-based 3D printing resin, VITRA DS2000 (DWS, Thiene, Italy), was used to fabricate all the scaffolds and non-porous control in this study. To create the PDMS print surfaces used in the monomer vat for 3D printing, a Sylgard-184 silicone elastomer kit (Catalog# 24236-10, Lot# 220808, Dow Chemical Co, Hatfield, PA, USA) was employed.

2.2.2 *Sensitivity test*

The sensitivity test was used to evaluate the performance of different pairings of laser intensity and laser writing velocity. The test pattern used was a 1.5mm (X) × 1.5mm (Y) base, consisting of 63 (7×9) 100μm × 100μm (X, Y) squares with 7 different velocities and 9 different laser intensities (the printer modulations), with a 100μm × 100μm (X, Y) square at the top left corner used as a direction reference. The sensitivity test was performed with a layer thickness of 64μm, using 7 velocities (100mm/s, 80mm/s, 60mm/s, 50mm/s, 40mm/s, 30mm/s, 20mm/s), and 9 modulations (100%, 80%, 60%, 50%, 40%, 30%, 20%, 10%, 5%). The reference squares were printed with a velocity of 15mm/s and a modulation of 50%. After the tests were printed, they were immersed in two subsequent isopropanol rinses for 10 minutes to remove additional resin attached to the surface and dried at room temperature for 10 minutes.

2.2.3 *3D printing of the sensitivity test*

The sensitivity test pattern is an important tool to evaluate the performance achieved with different combinations of laser intensity and writing velocity. The KLOE high resolution 3D lithographic laser system, which uses a 375nm laser to print objects layer-by-layer rapidly, was used to print the sensitivity test pattern. During the printing process, structures were printed upside

down, with the printing stage moving in the Z direction and the laser source moving in the X-Y plane. Before the structure is printed, a base is printed with 100% modulation and 50mm/s velocity to ensure the photo polymerization process is performed on an even surface. The PDMS absorbs oxygen during the printing process, which acts as a photo inhibitor during the polymerization process, creating a layer of unpolymerized resin between the printed structure and the PDMS. After the sensitivity test pattern was printed, it was immersed in isopropanol and rinsed to remove any uncured resin attached to the surface and dried at room temperature.

2.2.4 *Scanning electron microscopy (SEM)*

SEM images were obtained of the printed samples and test specimens subsequent to gold sputtering using an SNE-3200M SEM with an acceleration voltage of 5kV.

2.2.5 *PDMS coating on the vat printing surface*

A 12g mixture of the Sylgard-184 silicone elastomer kit, consisting of a 10:1 ratio of base polymer to cross-linker, was used to coat the polymerization vat and form a layer of PDMS. This layer serves as a photo inhibitor during the polymerization process and allows the printing stage to move up with the polymerized part. The PDMS layer is able to absorb and transmit oxygen, preventing the polymer in contact with it from polymerizing during the printing process.

2.2.6 *Pioneer testing for the PDMS stabilization process*

A total of 2g of mixing ratio of 10:1 between base polymer and cross-linker of the Sylgard-184 silicone elastomer kit was utilized to form a layer of PDMS on each of the 35mm petri dishes. This process was repeated 12 times, and every 4 petri dishes were considered as a set, resulting in a total of 3 sets. After each set of PDMS was coated on the petri dishes, 5g of DS2000 was applied

and left on for 10 minutes, 60 minutes, 24 hours, and 120 hours, respectively. Subsequently, the DS2000 was removed, and the petri dishes were rinsed with isopropanol until no viscous liquid was visible. Next, the petri dishes were placed in the Spectrolinker XL-1500 UV Crosslinker equipped with 6 365nm UV lights (BLE-1T151) on for 9 minutes. Finally, the results of every set were compared under the UV lamp (UVP, UVGL-25 Compact UV Lamp, P/N 95-0021-12) with a wavelength of 365nm.

2.2.7 *Quantification of stabilization process*

A total of 3 g of Sylgard-184 silicone elastomer, with a mixing ratio of 10:1 between the base polymer and cross-linker, was employed to create a layer of PDMS on individual wells of a 6-well plate. This procedure was repeated 20 times, with every 5 wells forming a set, resulting in a total of 4 sets (n = 4). Following the PDMS coating for each set of wells, 5 g of DS2000 was applied to 4 out of 5 wells in each set, and left for durations of 10 minutes, 60 minutes, 24 hours, and 120 hours, respectively; the remaining well served as the blank control. Afterward, the DS2000 was removed, and the wells were washed with isopropanol until residual viscous liquid was no longer visible. Subsequently, the wells were placed in a Spectrolinker XL-1500 UV Crosslinker, which was equipped with 365 nm UV lights (BLE-1T151), for a duration of 9 minutes. Finally, the outcomes of each set were compared using the BioTek multi-mode plate reader with a 400 nm blue filter.

2.2.8 *PDMS stabilization process*

After establishing the printing parameters, a sensitivity test was carried out using DS2000. Following the test, the PDMS coating was immersed in 40mL of DS2000 for 120 hours. The liquid resin was subsequently removed, and the PDMS was soaked in isopropanol for 30 minutes,

followed by a 5-minute rinse with isopropanol. The vat was then placed in a UV chamber (Spectrolinker XL-1500 UV Crosslinker) with 6 365nm UV lights (BLE-1T151) on for 9 minutes. The above steps were repeated until the sensitivity test results stabilized within a range of 42-49 printed squares.

2.3 RESULTS AND DISCUSSIONS

During the printing process, two types of contamination were postulated to affect the PDMS state: internal contamination and surface contamination. Internal contamination occurs when the resin infiltrates the PDMS network and photocured during the printing process with the UV laser, resulting in swelling, as depicted in the figure 2.3 below.

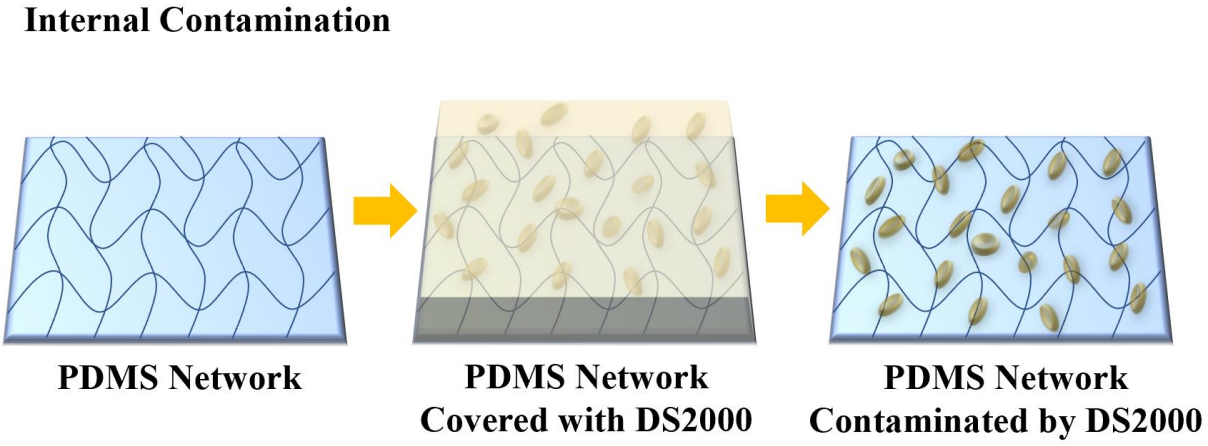

Figure 2.3. the schematic diagram of internal contamination

To address this issue, a preliminary experiment was conducted using small PDMS coatings. The results indicated that the UV absorbance varied with different immersion times, as depicted in the figure 2.4 below. Specifically, the 120-hour immersion time resulted in slightly higher absorbance compared to the 24-hour immersion time, indicating that DS2000 penetrated the PDMS network at a slower rate between 24 and 120 hours, nearing saturation of the network. But

since it was still evolving between the 24 hours and 120 hours period, 120 hours was still chosen as a suitable duration for the stabilization process of the actual-sized PDMS on the printing vat.

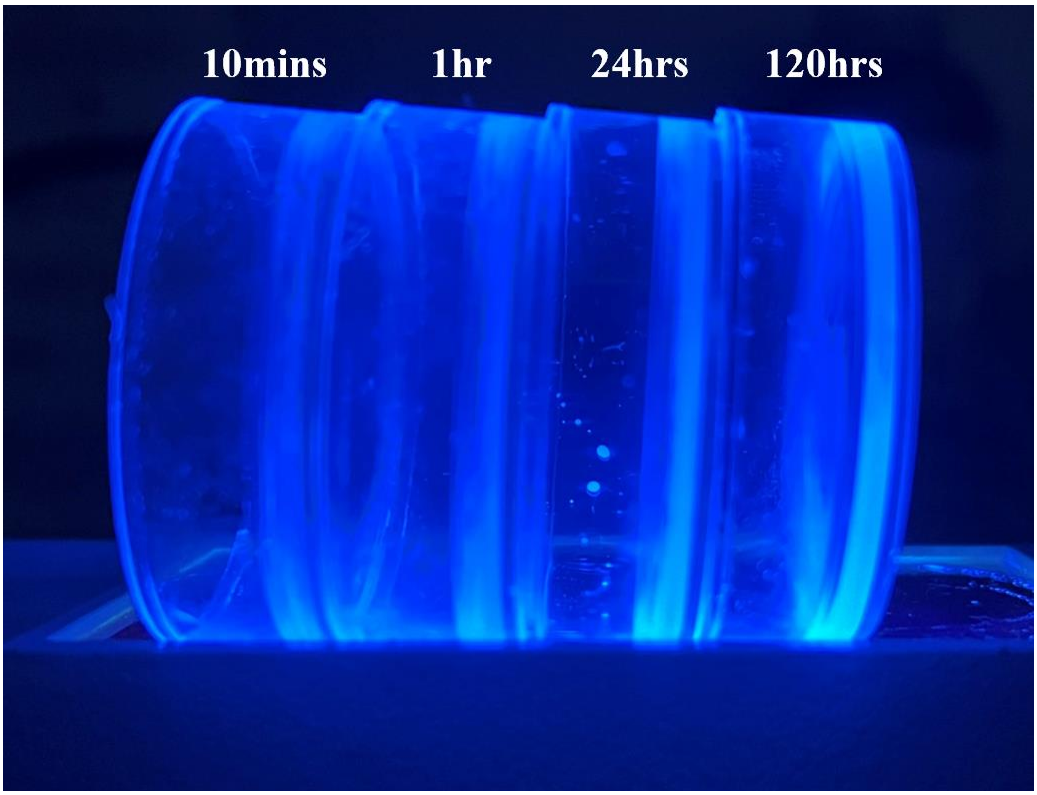

Figure 2.4. the comparison results for the pioneer test, from left to right are the test with 10 minutes, 1 hour, 24 hours, and 120 hours

To better quantify the UV absorbance, we transfer this experiments into a 6-well plate and repeat the same process, then read the data in the UV-plate reader, the result is shown in figure 2.5 below. The rate of penetration declined over time, yet a small degree of penetration persisted between the 24-hour and 120-hour intervals. Consequently, the duration of 120 hours immersion in DS2000 was selected as the optimal penetration time for the stabilization process and was subsequently applied to the PDMS coating on the vat.

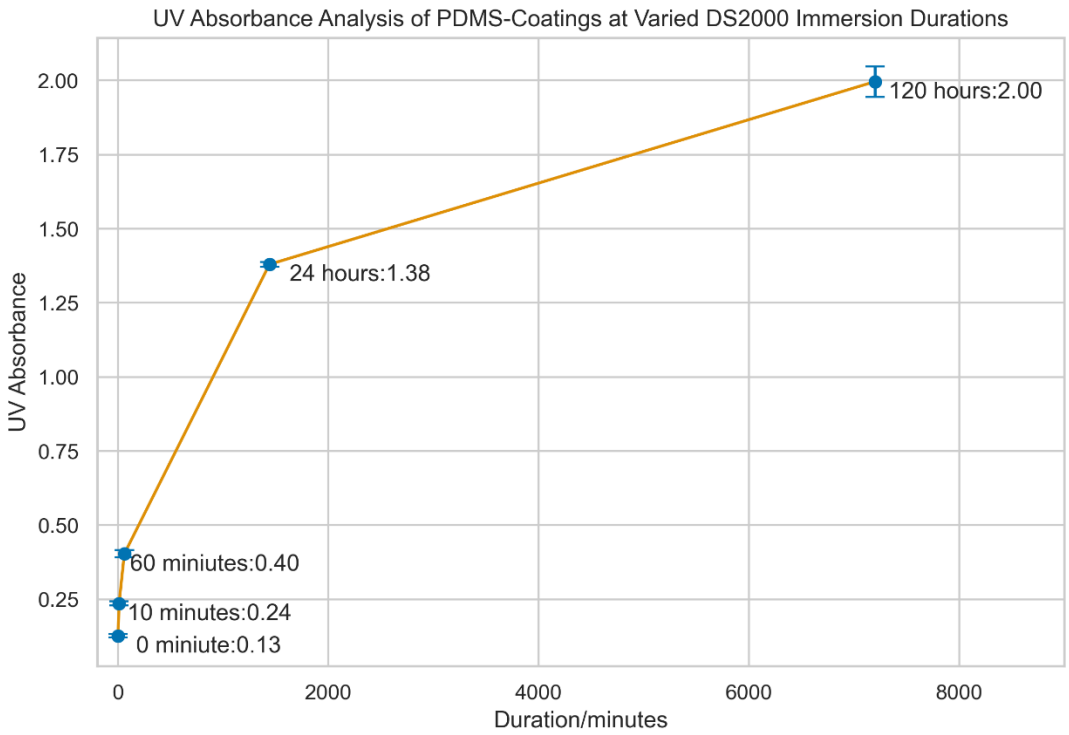

Figure 2.5. UV Absorbance Analysis of PDMS-Coatings at Varied DS2000 Immersion Durations

A stabilization process, also known as pre-saturation, was conducted on a new PDMS surface to address internal contamination, as shown in the figure 2.6. The study revealed that an immersion time of 240 hours in DS2000, followed by 18 minutes of UV exposure, resulted in stable sensitivity test outcomes, with the lowest discernable laser modulation at around 20%. After the 5th sensitivity test, no additional UV exposure was necessary as consistent outcomes were achieved. The first five results are illustrated in Fig. 2.7, and the rest of the results are summarized in figure 2.8. It is apparent that PDMS print surface internal contamination can reach saturation, leading to predictable results. The number of printed squares varied for two reasons: high printing velocity that induced vibration and shear force on the printed squares, causing loosely adhered squares to

detach from the printing base, and surface contamination caused by the base, which varied each time before the squares were printed.

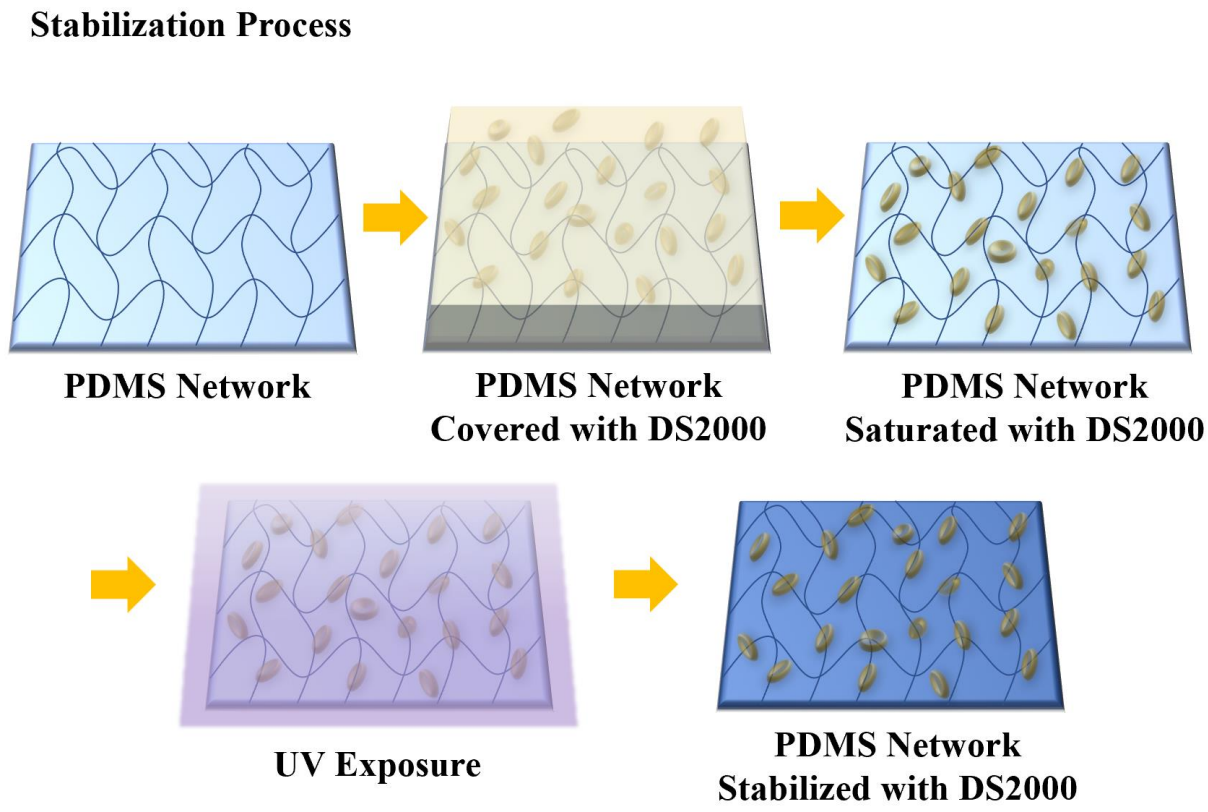

Figure 2.6. the schematic diagram of stabilization process of PDMS

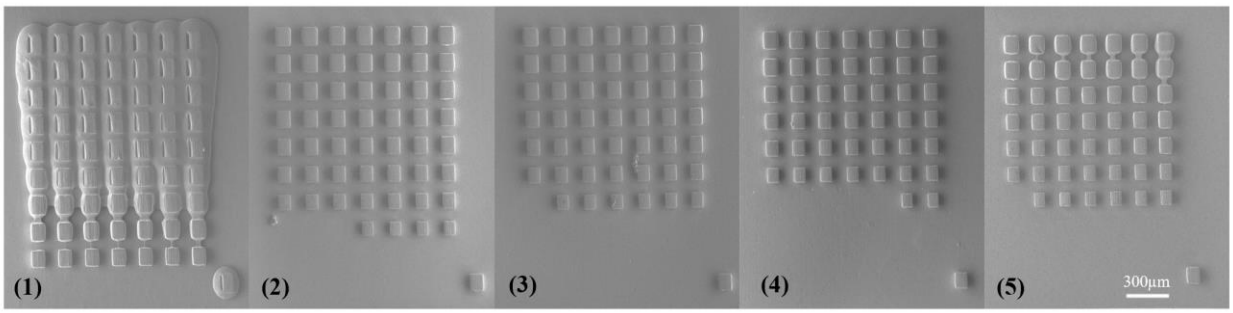

Figure 2.7. the first 5 sensitivity test results for the stabilization process

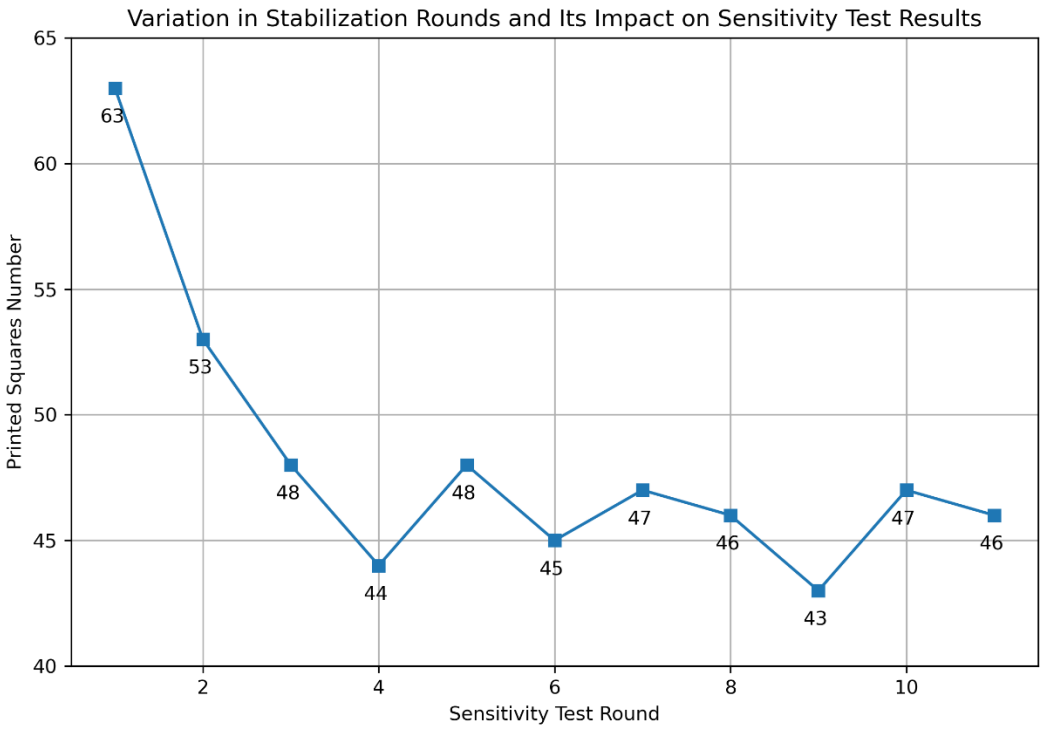

Figure 2.8. the stabilization results for the stabilization process

Surface contamination occurs on the PDMS surface during the printing process, along with over-curing, when the actual layer thickness is greater than the gap between the printed layers and the PDMS. In this case, the curing resin fills the gap and compresses the PDMS surface, as depicted in figure 2.9. During this process, the absorbed oxygen in the PDMS cannot maintain the dead zone, and the curing resin comes into close contact with the PDMS surface, leaving residues attached to the PDMS in the form of spots, as shown in figure 2.10. Although the surface contamination can be washed off by 70% ethanol or isopropanol, it cannot be removed during the printing process, and the contaminated spot blocks the laser, thereby slightly reducing the laser intensity. Theoretically, a well-controlled printing process can fabricate layers precisely, yielding a stable layer thickness, which is one of the main objectives of this study.

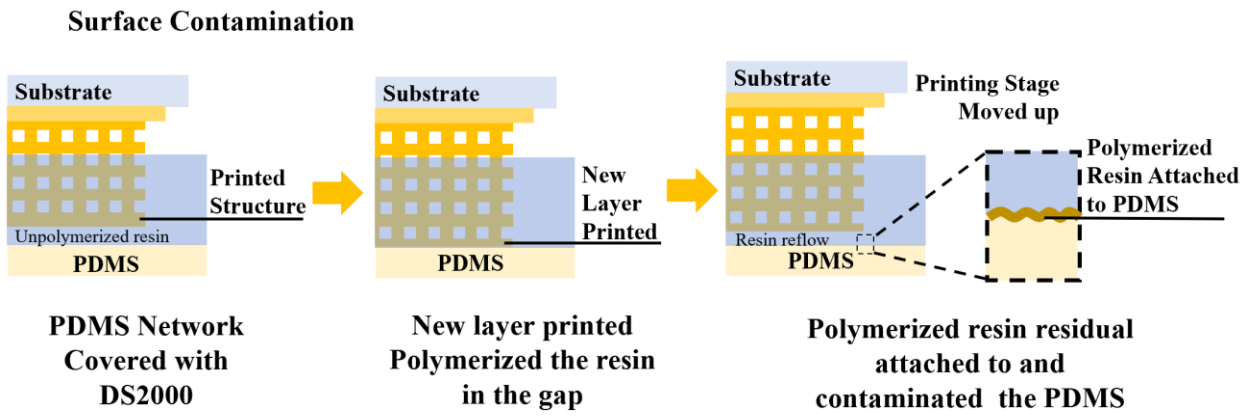

Figure 2.9. the surface contamination

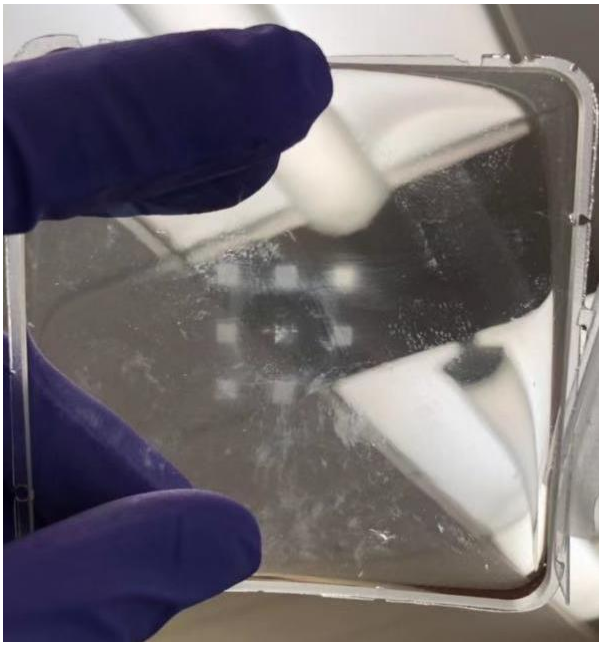

Figure 2.10. the example of surface contamination

Surface contamination, which refers to the adhesion of resin to the PDMS surface of the printer vat, is a common occurrence in vat polymerization. However, if the layer thickness is thick and the over-cured problem is not severe, it would not significantly affect the printing results. Hence, there is not much research on reducing surface contamination on the PDMS surface. However, for high-resolution 3D printing where the layer thickness is thin, surface contamination

can have a significant impact on the printing results. Therefore, it is crucial to address this issue for precise printing.

If surface contamination accumulates during the printing process and forms a coating on the PDMS surface, it can cause the actual laser intensity to change and result in variations in the printed layer thickness within the same structure. This can induce over-curing, perfect curing, and under-curing to occur simultaneously, as shown in the figure 2.10, a porous scaffold formed with Mneger Sponge units was printed. The main part of the structure can be over-cured, while the top few layers may be under-cured. The top layer may even remain unprinted, exhibiting only some edges, highlighting the effect of surface contamination. Furthermore, the top few layers may appear wrinkled and uneven, as the PDMS surface is no longer flat due to the resin residuals sticking to it.

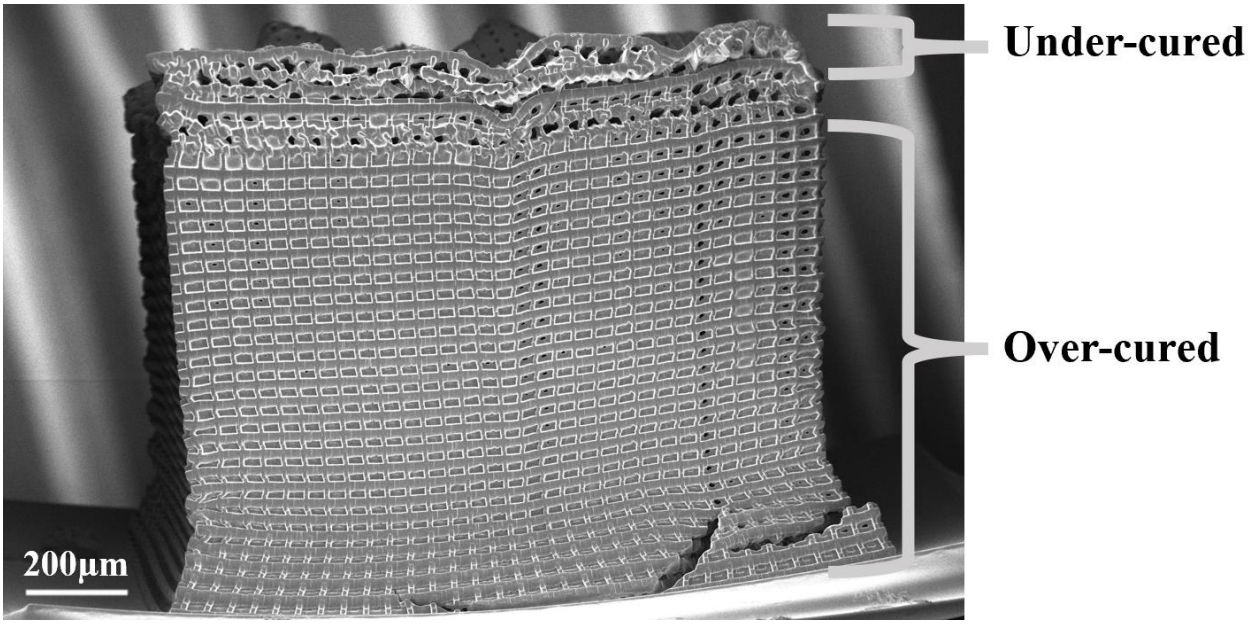

Figure 2.11. the printing result with surface contamination

Additionally, there is a more severe consequence of the accumulation of surface contamination during the printing process. If over-curing is significant enough, the residuals can be compressed together with the PDMS and potentially damage it, as illustrated in the example in

figure 2.12 below. In such cases, the vat must be recoated, and the stabilization process must be redone, which is a time-consuming endeavor.

Figure 2.12. the resin residues stick on the PDMS and making the PDMS no available to use

Currently, there is no effective solution to the problem of surface contamination during the printing process. However, it is possible to reduce its impact by optimizing the printing process and precisely controlling the layer thickness. In doing so, the effect of surface contamination can be eliminated to a negligible level. Further research on this issue will be conducted in later chapters.

2.4 CONCLUSIONS

Achieving a stable printing environment is the initial step towards achieving high-resolution 3D printing and precise layer thickness control. During the printing process, we have observed two primary types of contamination on the printing vat: internal contamination and surface contamination, both of which can significantly impact printing results. By stabilizing the PDMS on the printing vat for 240 hours with resin and exposing it to UV for 18 minutes, we were able to

achieve saturation and consistency in subsequent experiments. However, surface contamination is an unavoidable issue in vat polymerization and will be discussed in greater detail in later sections.

Chapter 3. DEVELOPMENT OF 3D PRINTED 6S STRUCTURES

3.1 INTRODUCTION

Foreign body reaction (FBR) is a complex immune response of the body to the presence of foreign materials. It is a natural defense mechanism that aims to isolate and remove potentially harmful substances. FBR commonly occurs when biomaterials are implanted in the body, such as medical devices like pacemakers, artificial joints, or tissue engineering scaffolds[68]. Despite their numerous benefits, FBR poses a significant challenge as it can result in implant failure, inflammation, and tissue damage[28].

The Ratner Lab has successfully engineered a precision microporous structure with a 40μm pore size (6S structure) that has demonstrated an optimized angiogenesis and reduced scar layer formation *in vivo*[63]. This microporous structure has shown a unique response from the body, distinct from the classic FBR, by attracting macrophages to reside within the porous scaffold and activating them into a pro-healing state that orchestrates the healing process[35]. Various materials with this microstructure have been tested and have exhibited a seamless healing pattern in skin, sclera, bone, and heart stroma. The cellular response to implanted polyHEMA in different pore size scaffolds is shown in figure 3.1 below.

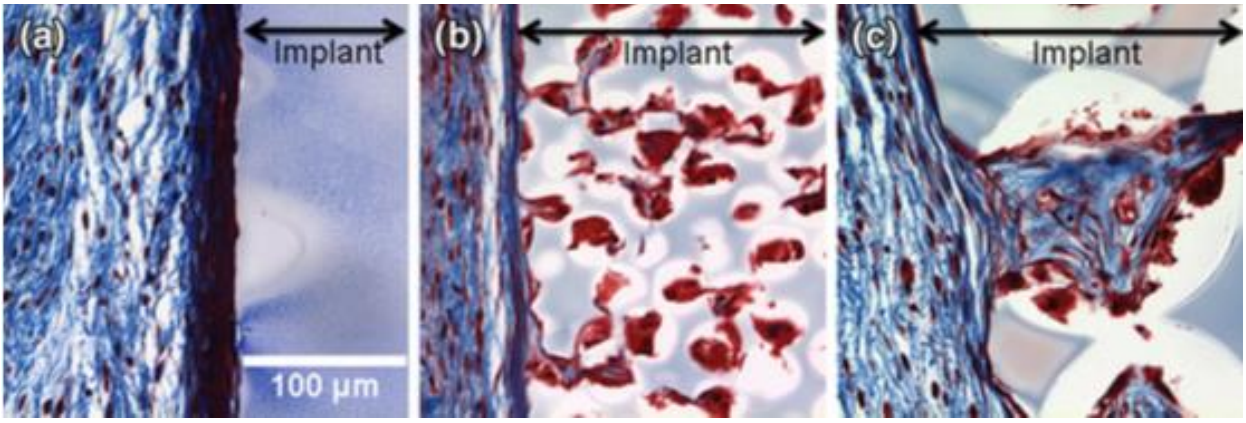

Figure 3.1. cellular response to implanted polyHEMA[35]

The 6S process, including 6 steps, is utilized to synthesize the 40µm porous scaffold, causing the material is also called the 6S scaffold or 6S structure. The flow chart in figure 3.2 depicts the operation of the 6S process. The inner structure of the porous scaffold can also be viewed in figure 3.3 below. Traditional fabrication methods only permit the creation of shapes with molds within the laboratory. To employ this structure in a more complex architecture, a novel manufacturing approach was required. Given that the internal structure is uniform and digitally designed on a computer, a new method was attempted for scaffold production - three-dimensional (3D) printing.

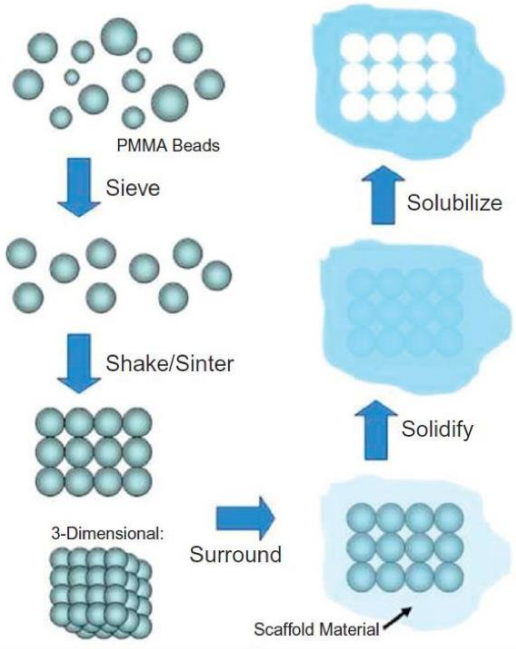

Figure 3.2. 6S process to synthesis the porous scaffold[9]

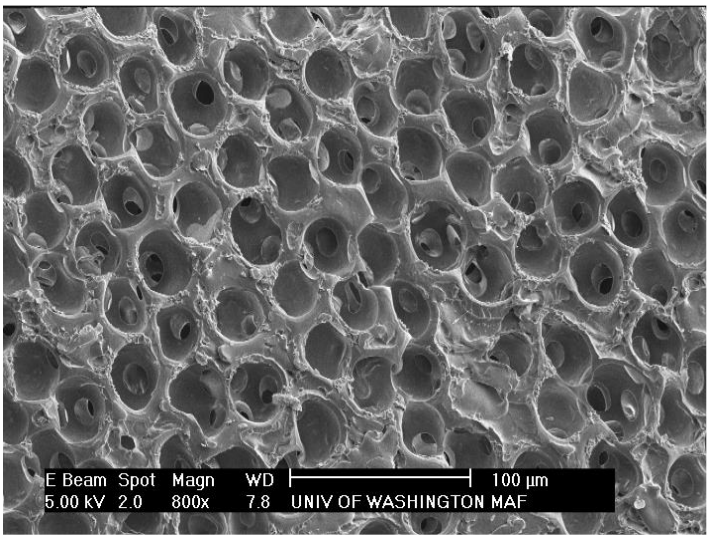

Figure 3.3. the porous scaffold[69]

Previously, we reported that resolving the resin reflow issue allowed for the precise fabrication of the 6S scaffold, measuring approximately 795 (X) × 795 (Y) × 79.5 (Z) μm, or 10 × 10 × 1 units, with a high-resolution top view but an over-cured side view, as illustrated in Figure 3.4 below[70]. However, when attempting to increase the overall dimensions of the structure, we encountered both design and fabrication challenges. The .stl file size grew excessively, rendering it unmanageable for the printer, and the resin reflow problem resurfaced during the fabrication process. Further investigation is required to address these issues effectively.

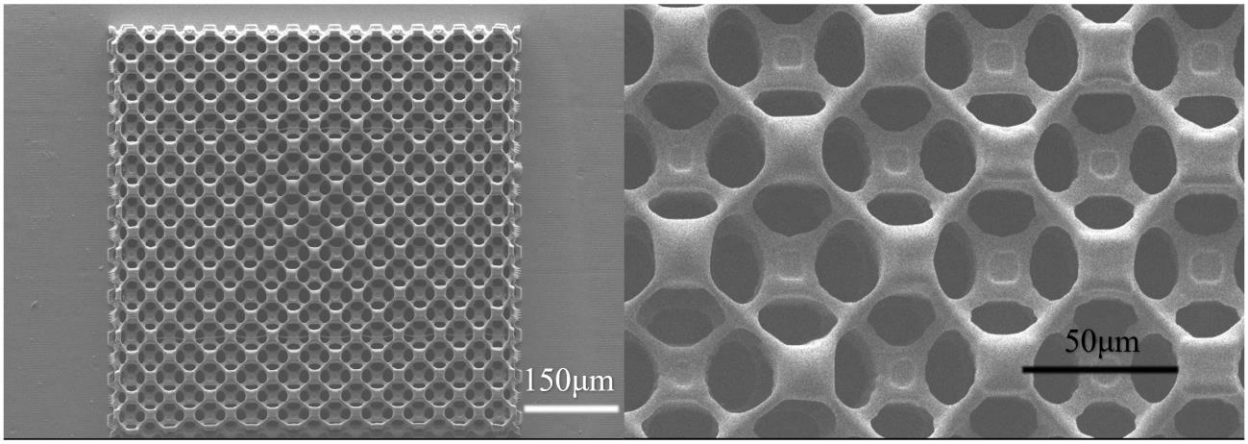

Figure 3.4. the result of 10×10×1 model with 60μm pore size

This section of the study aims to continue to utilize the KLOE 3D printing system and other advanced additive manufacturing method for the precise fabrication of the 6S structure. Given that the internal pore shape of the 6S structure is spherical, a small layer thickness is necessary to maintain the smoothness of the pore surface, and would definitely induce over-curing problem, indicating that the primary objective of this study is to evaluate the printing system's performance and determine whether it can maintain high resolution in the X-Y plane, and the over-cured problem will be addressed in later sections.

3.2 METHODS AND MATERIALS

3.2.1 *Materials and Equipment*

DS 2000 Resin (DWS, 10200075, 1kg) is used as the original printing resin; Acetone (Fisher Chemical, A949-4, 4L) and 2-propanol (Fisher Chemical, A451-4, 4L) are used as cleaning materials for the substrates and vats.

Main equipment used in the experiments is listed below.

KLOE High resolution 3D lithographic laser system, including the high-resolution 3D Printer: Dilase 3D; sec SNE-3200M Scanning Electron Microscope (SEM).

3.2.2 *Design the Simplified 6S Porous Structure*

Blender software was utilized to design the simplified porous scaffold with 40μm pore size. The original design process involved creating a UV sphere with a 20μm radius, duplicating it, and then using the Boolean Union function to merge the two spheres together. The interconnectivity between the two spheres was set to approximately 15μm, with an overlap length of 3μm. This process was repeated, and the spheres were merged together to the desired size. Finally, an object

with the desired dimensions was created, and the Boolean Difference function was used to sculpt the final structure with the merged spheres.

To further simplify the porous structure, Bulk (golf ball) sphere or C60 sphere can be used instead of the UV sphere. A comparison of several different spheres is shown in Figure 3.5.

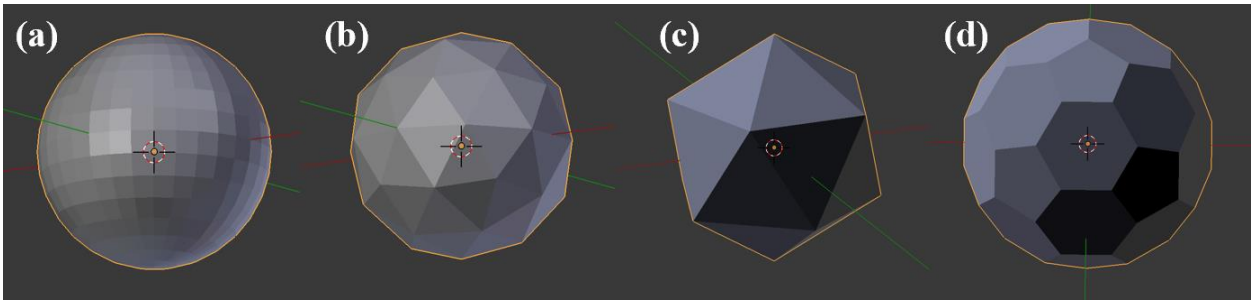

Figure 3.5. several sphere trails in the porous structure, from left to right are: (a) 512 faces UV sphere, (b) 80 faces Bulk sphere, (c) 20 faces icosahedron and (d) 32 faces carbon 60 (C60)

3.2.3 *3D printing of porous scaffolds*

This section utilizes the porous scaffolds designed in section 3.2.2, in lieu of the sensitivity tests performed in section 2.2.3.

3.3 RESULTS AND DISCUSSIONS

3.3.1 *Printing Complex Architectures Formed with the Simplified 6S Units*

As the complexity of the architecture increases, the 3D model files, or .stl files, may become too large for the printer software to handle. For example, the original 6S unit is curved with UV spheres, with each sphere consisting of 512 triangle faces. If the desired architecture is something implantable, the dimensions should be at least 5mm × 5mm × 1mm (X, Y, Z), and would consist of around 200,000 units. According to experimental records, the final file size would be more than 24Gb, which is not processable by the printer.

To simplify the complex structure, the approach outlined in section 3.2.2 was implemented, whereby the original UV spheres were replaced with bulk spheres or C60 spheres. Subsequently, a nerve guidance conduit, consisting of a single layer 6S structure, was designed and printed, as illustrated in figure 3.18 below. The simplified structure was successfully printed, and the software was able to handle it efficiently, resulting in a smooth curve. The object is with the dimension 2.1mm × 2.1mm × 0.053mm (X, Y, Z) was created with a modulation of 0.01% and velocity of 1mm/s, requiring a total forming time of 5 hours. Although the structure was able to be formed well, it was discovered during testing that the speed cannot exceed 1.4mm/s, as noted in previous thesis[70]. As such, it may be necessary to explore alternative methods for achieving higher printing speeds to address this issue.

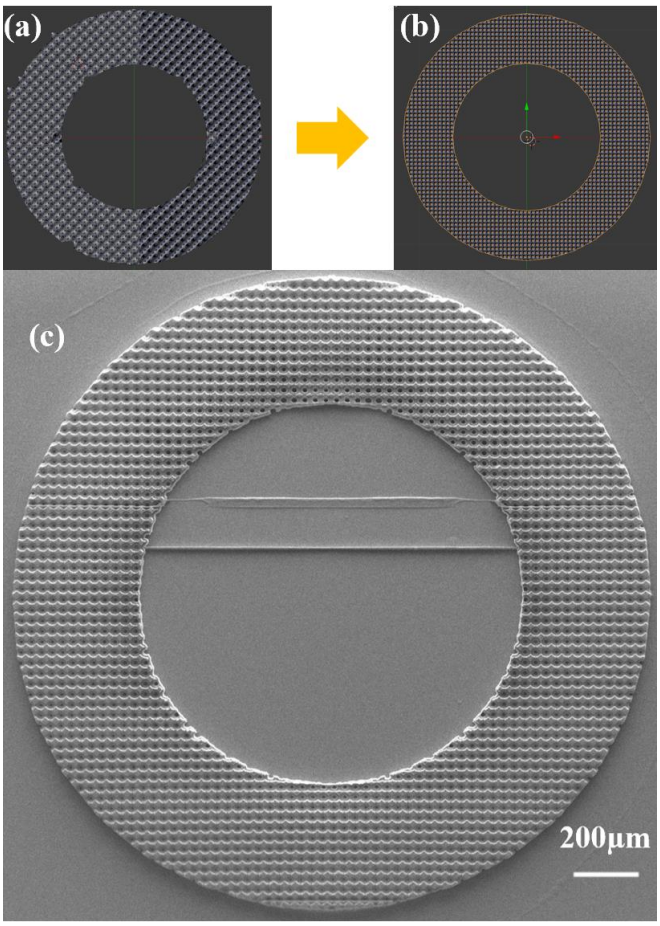

Figure 3.6. the insulin pump catheter models and printing results, (a)the model carved with the original unit, (b) the model carved with the C60 sphere, (c) the result of the C60 insulin pump catheter

3.3.2 *Printing Complex Architectures Formed with the Simplified 6S Units with CLIP (Collaboration with DeSimone Lab, Stanford University)*

As discussed in the previous research, the original 6S unit cannot be printed with a velocity exceeding 1.4mm/s using the KLOE 3D printer when utilizing a structur. In practical terms, this implies that it would take more than a week to print an implantable size 6S scaffold using this approach. To address this issue, the Continuous Liquid Interface Production (CLIP) technique developed in the DeSimone Lab at Stanford University was employed to print the 6S scaffolds.

CLIP is a cutting-edge 3D printing technology that leverages photosensitive resin and digital light projection to create exceptionally detailed 3D objects. The process, depicted in the schematic figure 3.19 below, differs from traditional layer-by-layer 3D printing in that it operates in a continuous motion, allowing for swift and precise production[55, 71]. CLIP's most significant benefit is its impressive speed, as it has the capability of producing objects up to 100 times faster than conventional 3D printing methods. This speed advantage makes it a highly efficient and cost-effective solution for prototyping and small-batch production[72].

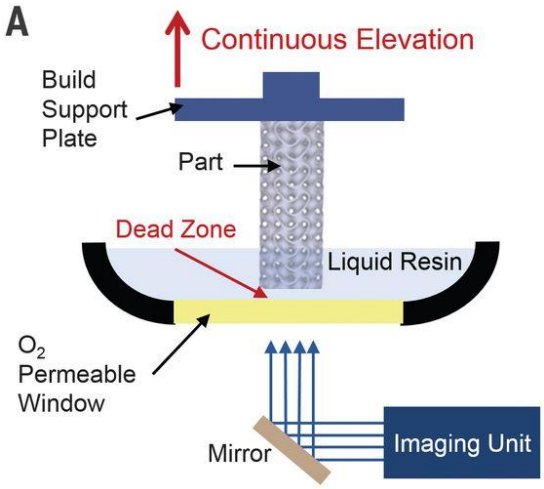

Figure 3.7. Schematic of CLIP printer where the part (gyroid) is produced continuously by simultaneously elevating the build support plate while changing the 2D cross-sectional UV images from the imaging unit. The oxygen-permeable window creates a dead zone (persistent liquid interface) between the elevating part and the window[71].

The high-resolution CLIP was used to print a simplified 6S scaffold with bulk sphere pores, with a dimension of 5mm×5mm×1mm (X, Y, Z). The printing process mainly focused on the initial few layers of the scaffold to achieve the desired resolution. Two types of resin were used in the study: Polyethylene glycol dimethacrylate (PEGDMA, Sigma-Aldrich, 437468, average Mn 750, 250g) with 2.5% diphenyl(2,4,6-trimethylbenzoyl)phosphine oxide (TPO, Sigma-Aldrich,

415952-10g) as a photo initiator, and 0.4% 2-tert-butyl-6-(5-chloro-2h-benzotriazol-2-yl)-4-methylphenol (BLS, Sigma-Aldrich) as a photo absorber. Additionally, EPU-40 (Carbon 3D) resin was also used.

After optimizing the printing parameters, the 6S scaffold with bulk sphere pores was printed, and the result is shown in the figure 3.20 below. The printing time for a 5mm×5mm×1mm dimension structure was only 30 minutes, which is around 300 times faster than the KLOE printer. However, the side view showed that the over-cured problem is still an issue. To address this issue for porous structures, iCLIP was designed[73], and future collaboration with the DeSimone Lab is planned once they set up the new printer.

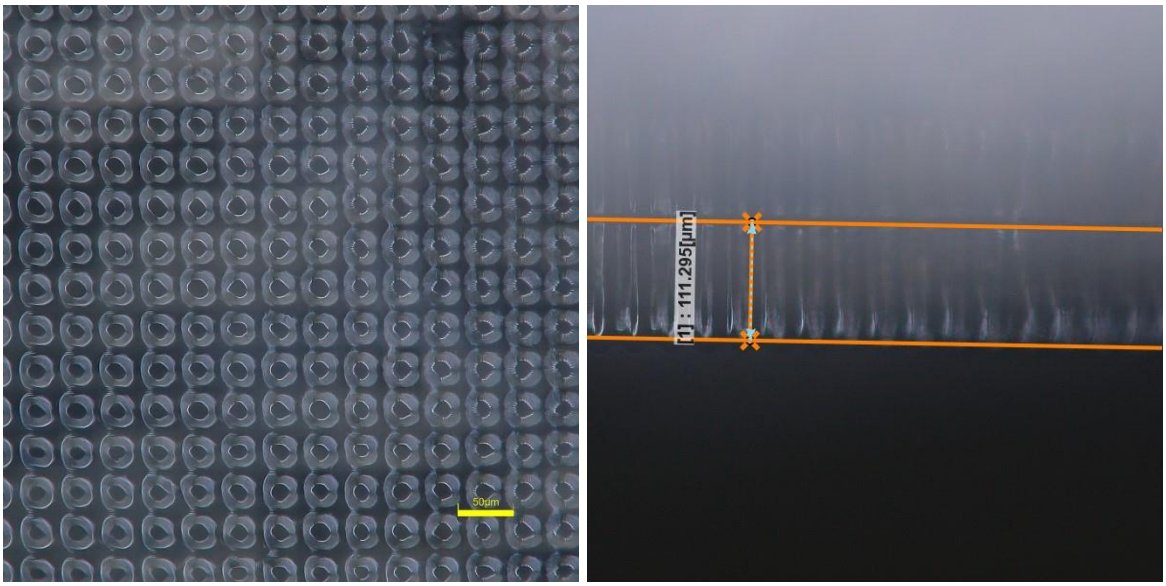

Figure 3.8. the result 6S scaffold with bulk sphere pores, printed with CLIP, the left one is the top view and the right one is the side view

3.4 CONCLUSIONS

The 6S scaffold, a porous biomaterial with 40µm pore size, has been shown to have excellent performance in reducing foreign body reactions upon implantation. Previously we susscessfuly

fabricated the scaffold with a fine top sureface, but while the structure is getting larger and model file has become hard to handle by the printer, the 6S structure was simplified by incorporating bulk spheres and C60 spheres, resulting in a reduction in the model file size and enabling the creation of complex architectures, including a 1 layer nerve guidance conduit formed with the 6S structure.

Collaboration with the DeSimone Lab using CLIP has significantly accelerated the printing process, reducing printing time from approximately 7 days to 30 minutes. However, the over-cured problem in the Z direction still persists, and as such, remains an area of future work.

Chapter 4. DEVELOPMENT OF 3D PRINTED POROUS STRUCTURES WITH DIFFERENT PORE GEOMETRIES

4.1 INTRODUCTION

Porous scaffolds play a critical role in tissue engineering and regenerative medicine applications by providing a supportive structure for tissue regeneration. The shape and size of the pores in the scaffold are crucial in determining its biocompatibility, mechanical properties, and cell behavior[74]. Spherical pores are commonly used in porous scaffolds, such as the 6S scaffold described in Chapter 3. Spherical pores provide a uniform distribution of mechanical forces throughout the scaffold, which promotes even cell distribution and proliferation. However, when the pore size decreases, fabricating the scaffold using 3D printing becomes challenging due to over-curing issues.

Cubical pore shapes offer an alternative structure used in tissue engineering scaffolds that can be more easily fabricated with 3D printing than scaffolds with spherical pores. Cubical pores offer anisotropic mechanical properties that are desirable for specific applications, such as bone tissue engineering[43]. In this study, we designed two different cubical porous units and assembled them into various architectures to develop implantable-sized porous scaffolds that can be easily formed by 3D printing for future in vivo studies. Unlike the previous chapter that focused on the resolution on the X-Y plane, this part of the study aimed to solve the over-cured problem in the Z direction and ensure that the cavities can be printed well in the porous scaffold.

To fabricate the scaffold precisely, we performed the stabilization method described in Chapter 2 for all the PDMS used in this part of the study. We also discussed surface contamination in-depth and proposed a hypothesis to avoid the effects of surface contamination.

4.2 MATERIALS AND METHODS

4.2.1 *Design of a porous scaffold with cubical pores*

Cylinder-shaped porous scaffolds and square-disk-shaped porous scaffolds have an overall size of 5mm(x) × 5mm(y) × 2mm(z). Porous scaffolds with 2 different unit cells were printed, the cubical architecture, and the cube- in-cube architecture, also known as the Menger Sponge. The 2 repeating unit cells are shown in the figure 4.1 and 4.2 below. In order to facilitate clarity and accuracy, the structures formed by the cube-in-cube architecture units will henceforth be referred to as Menger Sponge structures, or MS structures throughout the following text. To better understand the Menger Sponge unit, a corner-view unit and a 2×2×2 assembly structure are also shown in the figure below.

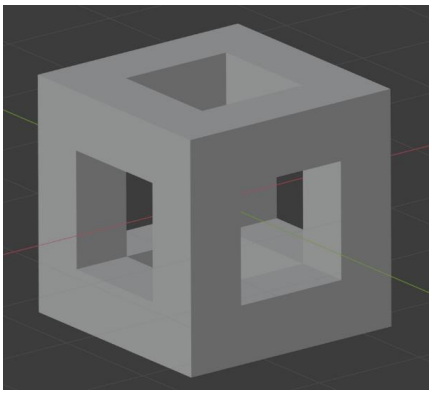

Figure 4.1. the cubical architecture unit

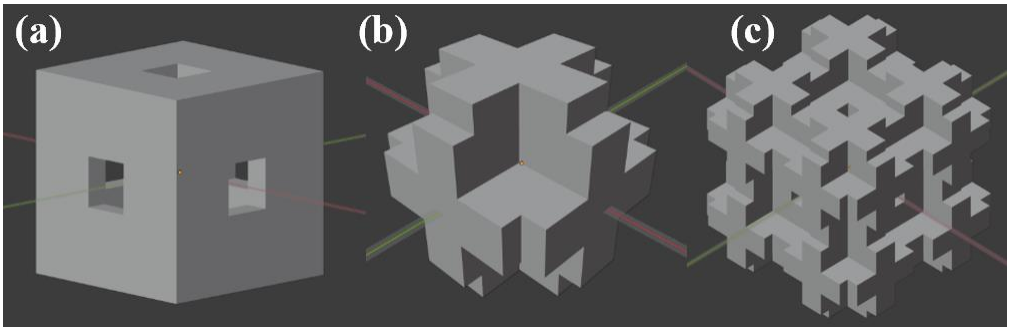

Figure 4.2. the Menger Sponge (MS) architecture unit, from left to right are the original unit, the corner-view unit, and the 2×2×2 assembly structure of the corner-view unit

The porous scaffolds consist of cubical cells with outer side lengths of 80μm and inner side lengths of 40μm. Two sizes of the Menger Sponge cell were printed, one with 96μm side-length internal cubical pores and 32μm interconnected cubical pores in the middle, with an outer side length of 128μm, and the other with 192μm side-length internal cubical pores and 64μm interconnected cubical pores in the middle, with an outer side length of 256μm.

Using the cubical cells, UW-shaped and CDI-shaped structures were assembled. The UW-shaped structure has an overall size of 8mm(x) × 4mm(y) × 0.5mm(z), and the CDI-shaped structure has an overall size of 8mm(x) × 3mm(y) × 0.5mm(z).

4.2.2 *3D printing of porous scaffolds*

This section utilizes the porous scaffolds designed in section 4.2.1, in lieu of the sensitivity tests performed in section 2.2.3.

4.2.3 *The bridge test*

To determine the precise thickness of each layer, a bridge test must be conducted. This involves printing a few thin bridges with a desired velocity and modulation between pillars, where the bridges hang over the base. The velocity and modulation values are obtained from the sensitive test. By capturing SEM images of the side view of the bridge test, we can determine the exact thickness of each layer.

To measure the thickness of the bridge, three random thickness measurements are taken in the middle of the bridge, and the average of these measurements is calculated.

4.2.4 *Critical point dry for the cross-section view*

First, turn on the critical point dry machine (Autosamdri-814, Tousimis Research Cooperation) and open the CO_2 outlet. Fill the chamber with pure ethanol and close it. Press the Advance button and wait for the machine to switch to cooling mode. Wait until the cooling mode light turns off before proceeding.

Next, immerse the sample in pure ethanol for 10 minutes. Transfer the sample to the critical point dry holder. Once the cooling mode light on the machine is off, immerse the holder in the critical point dry machine chamber. Close the chamber and press the Advance button. Wait for the light to switch to Finish.

After the process is complete, remove the sample from the holder and use a blade to cut it in half from the top.

4.2.5 *Measuring the layer thickness and pore size*

The software ImageJ is employed for assessing the layer thickness and pore sizes of the scaffolds. In cases where edges appear straight and distinct, the original scale bar featured in the SEM image is utilized as the reference. However, certain scaffolds exhibit non-linear edges, leading to a perspective effect in the 2D SEM images. Consequently, accurately measuring certain pore sizes using existing SEM scales becomes challenging. To overcome this issue, a new measurement technique is introduced. In proximity to the pores requiring measurement, two parallel lines are randomly selected in the Z-direction, typically along the edges of each layer. Given the known layer thickness, the distance between these reference lines is employed to establish a new scale for pore size measurement. All subsequent pore size data are determined using this approach. To improve data precision, only Z-direction distances are taken into account,

and for pores within the same layer, four random measurements are conducted (n = 4), as shown in figure 4.3 below.

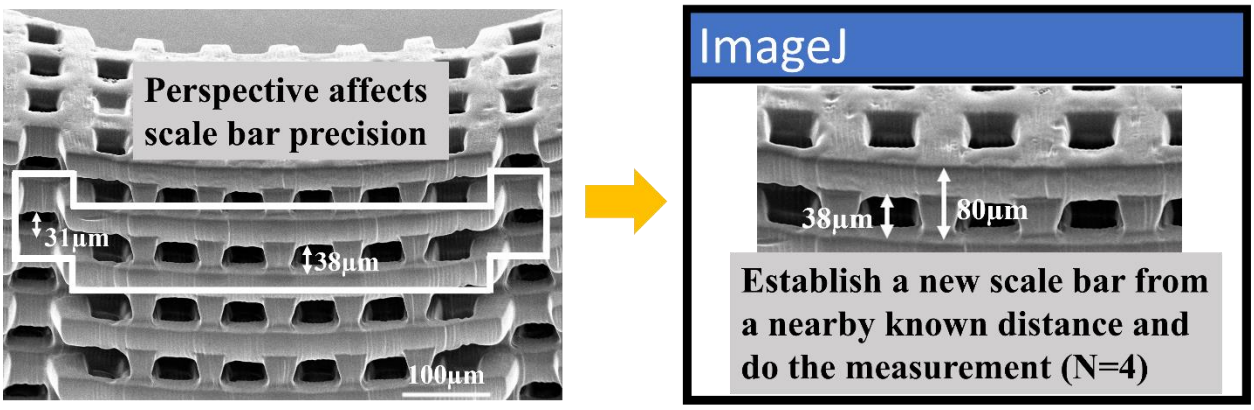

Figure 4.3. schematic for perspective-adjusted measurements with ImageJ

4.3 Results and Discussions

4.3.1 *The MS cells formed structures*

The use of a stabilized PDMS printing surface provides an environment that enables precise control of layer thickness. When printing parameters are well-controlled, surface contamination is not a significant factor in the printing results. Using this stabilized surface, a porous scaffold with cubical pores was fabricated, which can be divided into four repeatable layers that can be transferred into printable slices. Interconnectivity is located in the middle of every square with dimensions one-third of the cubical pores.

In Figure 4.4, a cylindrical-shaped porous scaffold with 192µm side-length cubical pores and 64µm interconnects is presented. The scaffold was fabricated using a printing base developed at 100% modulation and 50mm/s velocity. The cubical-porous scaffold was fabricated at 40% modulation and 60mm/s with a layer thickness of 64µm, resulting in a fabrication time of three hours. Due to the scaffold's high porosity, a significant amount of uncured resin was stored inside

and needed to be washed away. Therefore, after printing, the scaffold was immersed in two subsequent isopropanol baths for one hour and 24 hours.

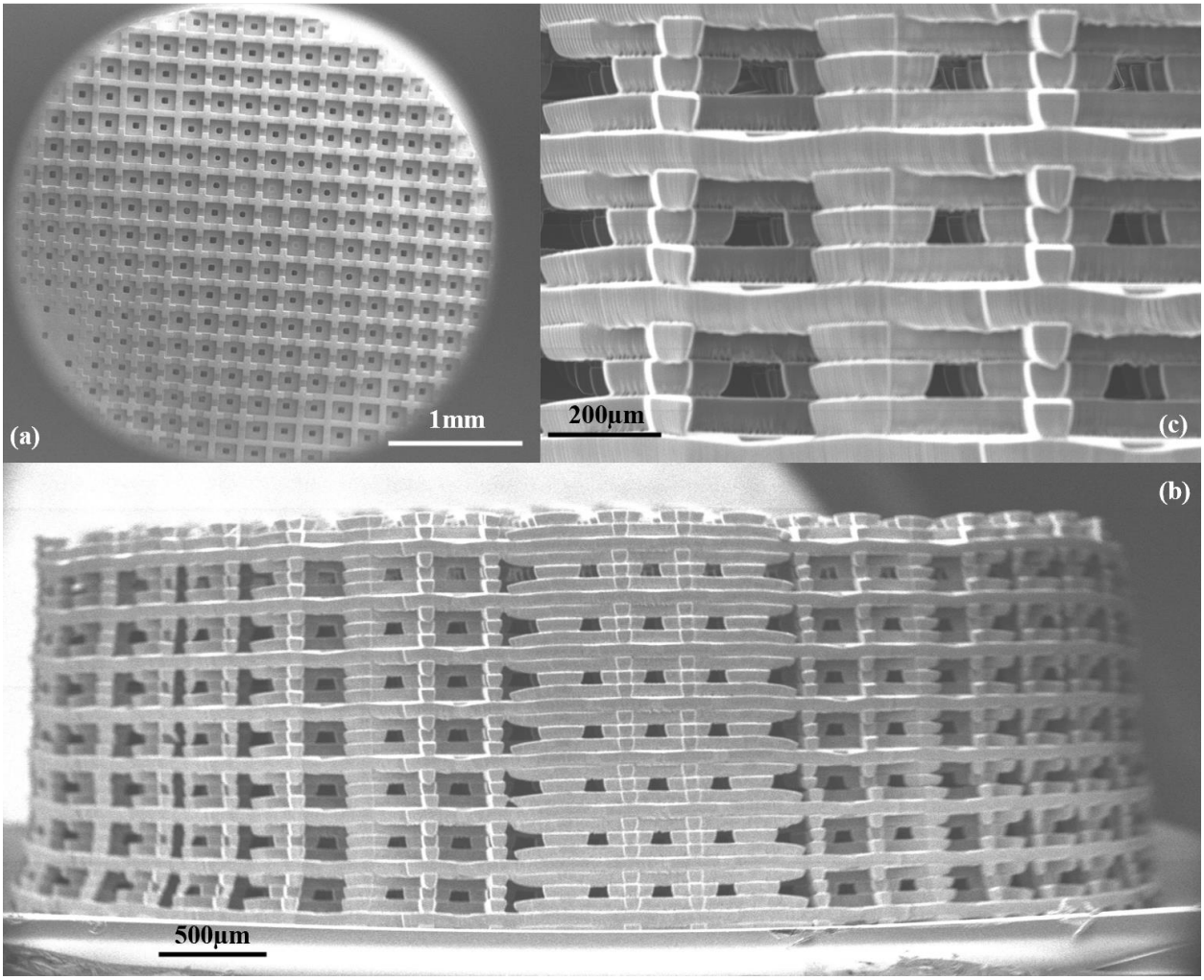

Figure 4.4. (a) the top view of the scaffold with 192µm side-length cubical pores, (b) the side view of the scaffold with 192µm side-length cubical pores and (c) a higher magnification view of the top layers showing the interconnectivity

This example illustrates that, with a stabilized vat coating and precisely controlled layer thickness, structures assembled with repeatable layers can be printed rapidly with micron resolution. The scaffold resolution between layers demonstrated micrometric periodic features

down to 64μm, and the fabrication process was relatively fast compared to two-photon polymerizations[53].

We hypothesize that surface contamination is not present in the scaffold printed with 64μm layer thickness demonstrating that 40% modulation paired with 60mm/s print speed is sufficiently high to achieve a rapid polymerization and cure a layer thickness around 64μm. This keeps the laser intensity uniform during the fabrication and is probably why multiple well-printed structures with KLOE Dilase 3D were all performed under this printing parameters.

In Figure 4.4 (a), some of the interconnects are obstructed by polymerized resin. This could be attributed to resin retained within the scaffold, even after the isopropanol rinsing process and subsequently polymerized due to natural light exposure in the external environment.

The side view in Figure 4.4(b) reveals the structural integrity maintained during the printing process. In Figure 4.4(c), a closer view of the uppermost layers highlights the inner cubical pores of the scaffold, showcasing that most of the structure is uniform. Further insights into layer thickness and pore size measurements are presented in Figures 4.5 and 4.6 below, as 4.5 is the measurement of all layers and 4.6 is the measurement of the pore size. It is evident that both the layer thickness and pore sizes across all layers closely align with the intended dimensions. This example effectively demonstrates that employing a stabilized vat coating and precise layer thickness control facilitates the rapid 3D printing of structures with repeatable layers and micron-level resolution. The scaffold exhibits a resolution between layers that manifests micrometric periodic features down to 64 μm. Importantly, the fabrication process is swift in comparison to two-photon polymerization additive manufacture[53].

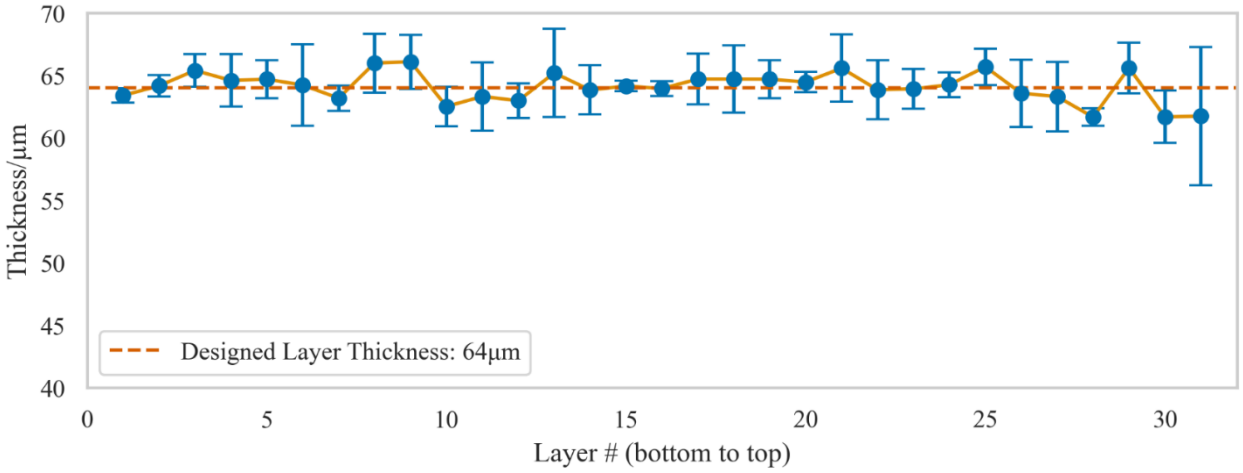

Figure 4.5 the layer thickness of the MS scaffold from bottom to top

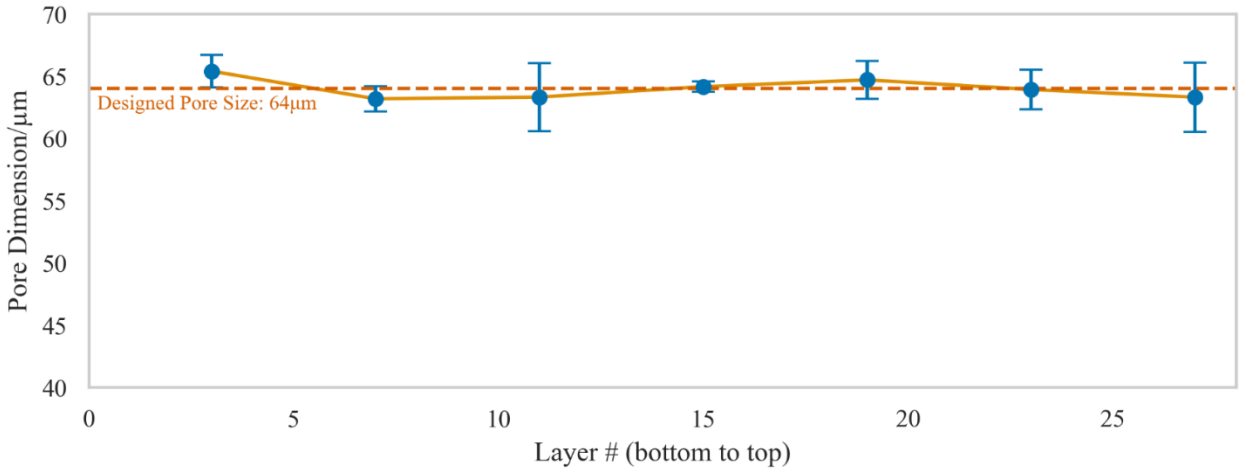

Figure 4.6 the minimum feature (pore size) achieved of the MS scaffold from bottom to top

In figure 4.4, a cylindrical shaped porous scaffold with 96µm side-length cubical pores and 32µm interconnectivity is reported. The architecture starts with a printing base developed at 100% modulation and 50mm/s velocity. The cubical-porous scaffold was fabricated at 30% modulation and 60mm/s with a layer thickness of 32µm, for an overall fabrication time of 6.5 hours. Although the porosity geometry of this structure is similar to the one shown in figure 4.3, because the pore size is only 12.5% of the 192µm pore, a longer post-rinsing time in 70% ethanol was performed. The specimen was immersed in two 70% ethanol rinses for 1 hour and 48 hours. The top layers of

the structure, which are shown in Fig 5b, show an actual layer thickness down to 32μm, but we assume that due to the surface contamination during the printing process, the printed layer thickness changed with the printed height, and the thickness of the majority layers is more than 32μm, as shown in figure 4.4c. This observation suggests that the 30% modulation paired with a velocity of 60mm/s are not sufficient to maintain a good surface with low contamination when printing with 32μm layer thickness. The over-cured problem here causes the surface contamination to gradually accumulate which reflects on later printed layers' actual layer thickness.

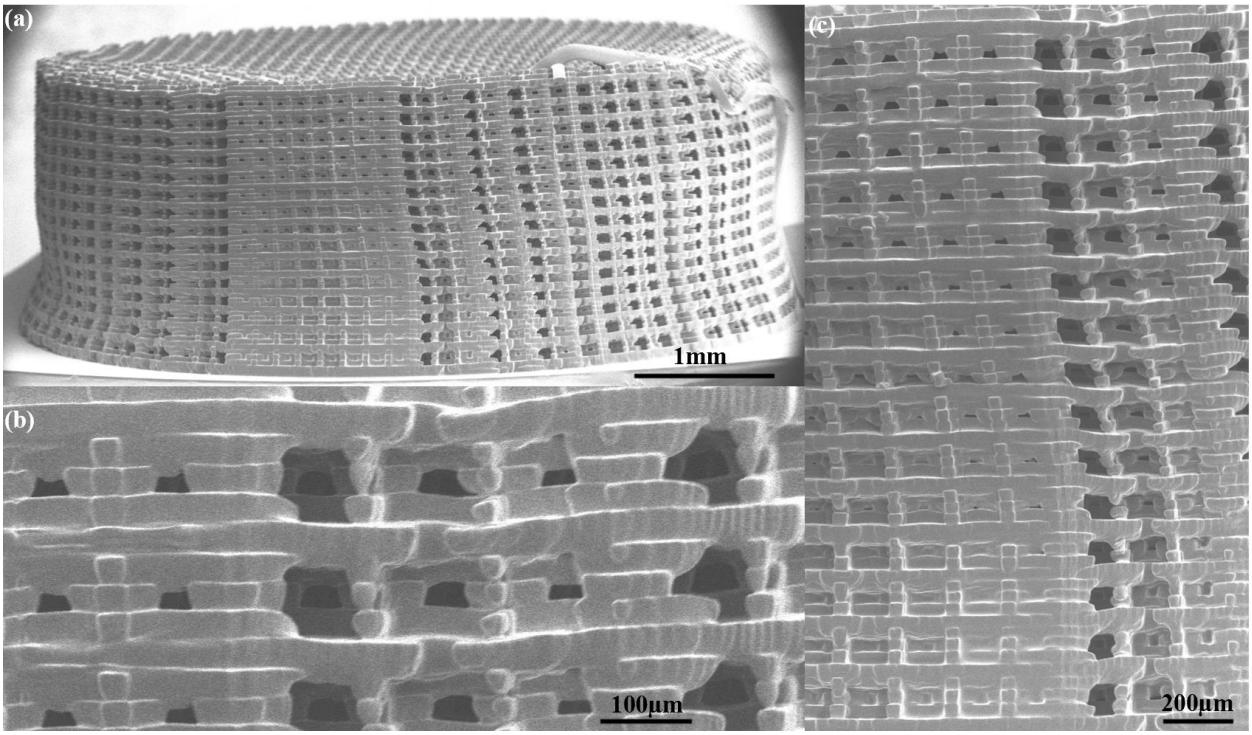

Figure 4.7. (a) side view of the scaffold with 96μm side-length cubical pores, (b) a magnified side view of the top few layers of the scaffold showing the layer thickness is around 32μm and (c) the layer thickness changes along the printed direction suggesting surface contamination accumulated during printing

Furthermore, the analysis of measurable pore sizes in Figure 4.8 below demonstrates fluctuations in the printing environment during the fabrication process, leading to alterations in the actual layer thickness over time.

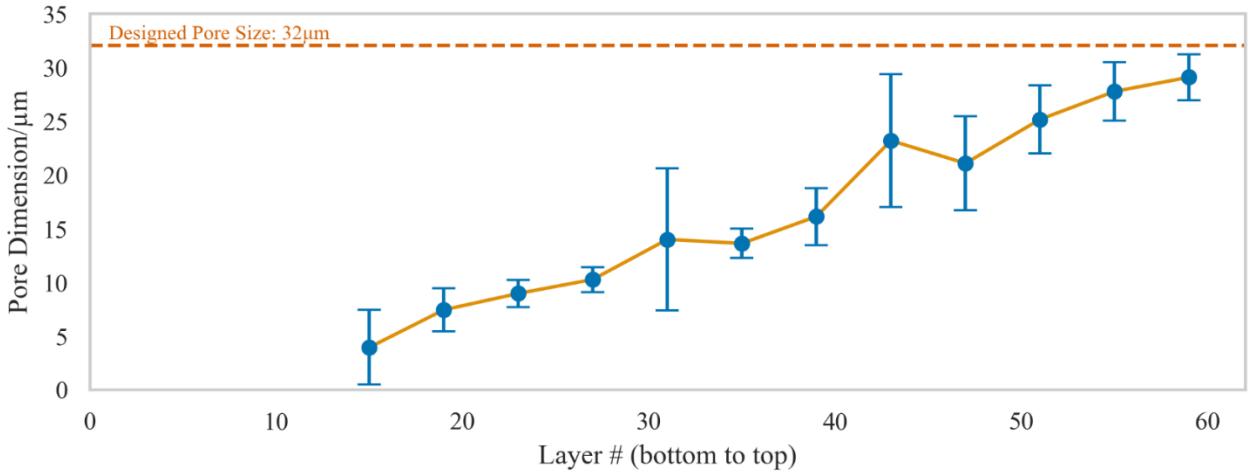

Figure 4.8. the measured pore size of the MS scaffold with 32 µm interconnects from bottom to top

Currently, there is no solution available to address the aforementioned issue. However, optimizing the printing process and determining precise printing parameters can help to mitigate this problem. To achieve this, we conducted a bridge test to identify suitable printing parameters for a layer thickness of 32µm.

The results of the bridge test conducted at velocities of 30mm/s and 60mm/s are depicted in the figure 4.9 and 4.10 below, along with the corresponding bridge thickness measurements. The data analysis revealed that the actual layer thickness did not increase significantly with modulation values above 70%, and the relationship between modulation and layer thickness was non-linear. However, when the modulation was between 10% and 70%, a linear relationship was observed. Based on the bridge test results, we determined that for a desired layer thickness of 32µm, a

modulation of 15% at a velocity of 60mm/s and a modulation of 5% at a velocity of 30mm/s should be used.

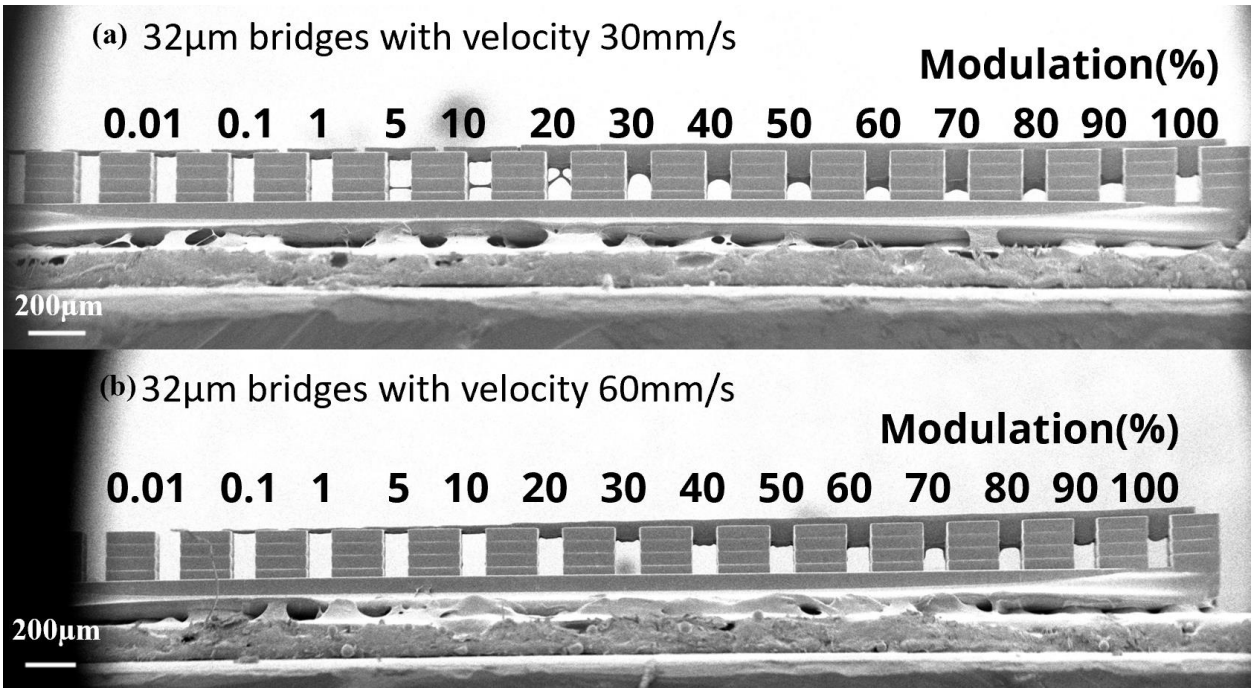

Figure 4.9. (a) the 32µm bridge test with velocity 30mm/s (b) the 32µm bridge test with velocity 60mm/s

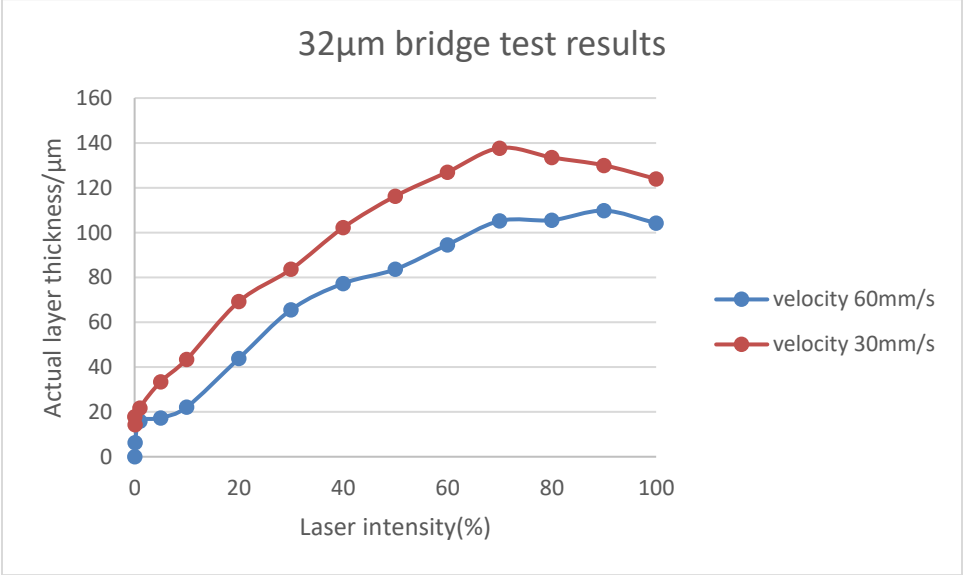

Figure 4.10. the 32µm bridge test results with velocity 30mm/s and 60mm/s in chart

However, when we attempted to print the MS unit structure with 32μm interconnectivity using these parameters, no structure was formed. This indicates that the bridge test results cannot be used as a reference for this particular structure. The reason for this discrepancy is currently unknown, but we hypothesize that it may be due to the relatively large size of the structure, which may require a higher and more stable laser intensity to form the layer. During the printing process, the laser requires an initiation time and a termination time, and if the moving distance is insufficient for the laser to reach a stable performance, the printed layer thickness with the same parameters may vary. Further investigation is necessary to identify the underlying cause of this issue.

Through multiple trials to pair the bridge test results with a larger structure, it was found that the bridge test result is not reliable. As the bridge only has one layer, it is difficult for it to mimic the multiple layers structure, and therefore, surface contamination and over-cured problems cannot be explored with the bridge test. The best way to optimize the printing process is to print the actual structure or at least the first few layers of it if the structure is repeatable in the Z direction, though it is time-consuming, but reliable.

It has been observed that every PDMS has a different performance, resulting in slight variations in printed layer thicknesses despite using the same printing parameters. After several trials, it was found that when the desired layer thickness is 32μm, it is challenging to maintain consistent layer thickness. The results can be separated into two categories: all layers are built and part of the layers are built. Regardless of the categories, all the printing results indicate that surface contamination cannot be ignored and significantly affects the printing result.

Assuming the printer's performance remains consistent, for each distinct structure, all layers would demand a uniform laser dose, i.e., the combination of laser intensity and velocity, to achieve an actual thickness approximating the intended value. If the laser dose surpasses the requisite level,

over-curing occurs, resulting in the physical compression of the PDMS coating and the deposition of residual material, and the residual material would decrease the transparency of the PDMS. This decreased transparency effectively decreases actual laser dose leading to a thinner next layer. This phenomenon is evident in the cylindrical-shaped MS scaffold with 32 μm interconnects, as illustrated in Figure above.

Ideally, by optimizing the laser dose to achieve an appropriate value and targeting a layer thickness of around 32 μm, successful fabrication can be achieved. However, our findings suggest that excessively low laser doses hinder the integrity of the printed structure. A hypothesis emerges that during polymerization, insufficient laser energy prevents complete solidification of the resin, resulting in a semi-solid state with elevated viscosity. Such layers are prone to leaving residues on the PDMS coating during the formation process, leading to increased surface roughness and opacity. This enhanced roughness facilitates adhesion to PDMS during layer-by-layer polymerization, generating a cycle of residue accumulation that significantly impacts the overall printed structure.

Following this hypothesis, if the optimized laser dose for a particular layer thickness falls below the minimum required level for full solidification, the printed structure experiences variable layer thickness along the Z-axis and cannot be accurately produced, as demonstrated in Figures above. In essence, there exists a theoretically achievable minimum layer thickness that can be tightly controlled, and 32 μm falls below this threshold. Guided by this hypothesis and considering our original goal of fabricating 40 μm pore-sized scaffolds, a new geometry has been designed and fabricated to evaluate whether 40 μm exceeds the required minimum layer thickness.

4.3.2 *The cubical units formed structures*

As discussed in Chapter 3, the 6S structures with a pore size of 40μm hold promise for reducing foreign body reactions. However, to determine whether 40μm is above the minimum layer thickness required, it is necessary to conduct further testing. To this end, a cubical unit with a 40μm cubical void was designed and printed, as shown in figure 4.11 below.

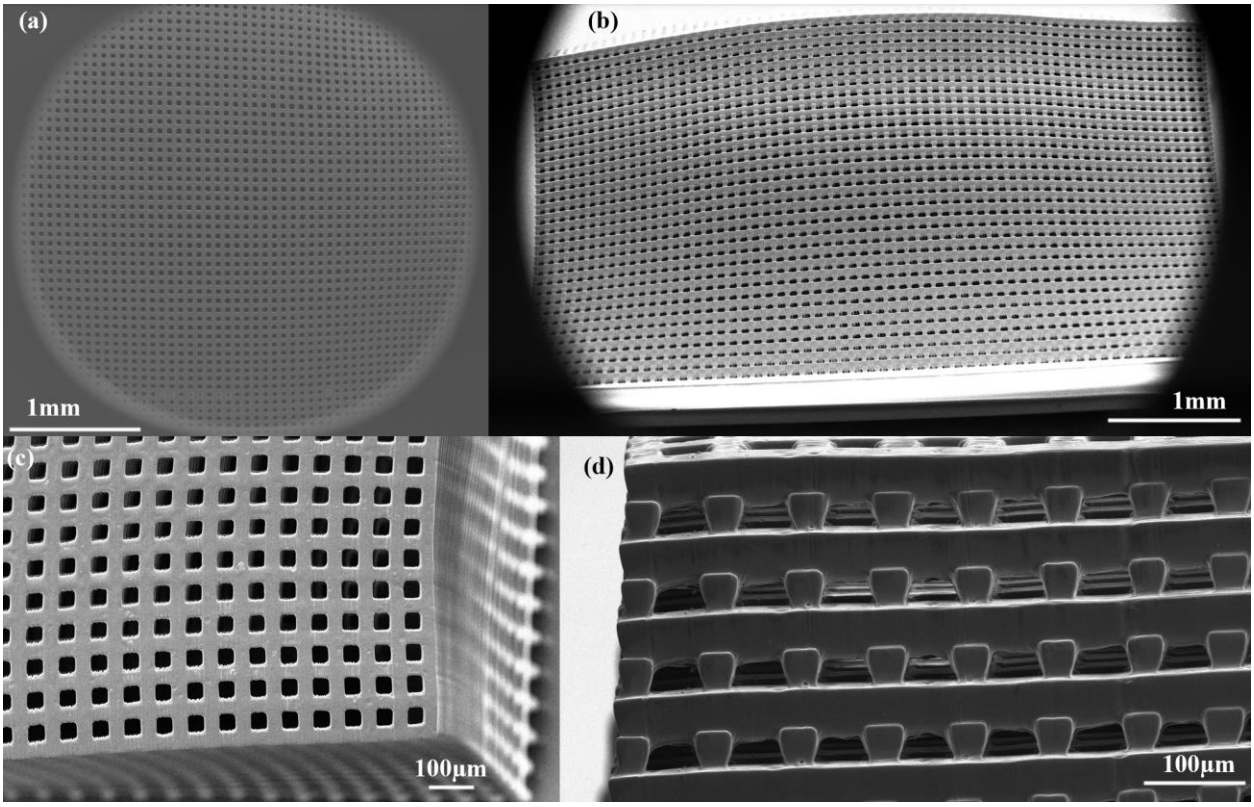

Figure 4.11. the cubical structure printed with 40μm layer thickness, (a) the top view, (b) the side view, (c) the corner of top view, (d) the corner of the side view

The structure was printed with a 100% modulation and 50mm/s velocity base, while the cubical-porous scaffold was fabricated at 38% modulation and 60mm/s, with a layer thickness of 40μm, taking 7 hours to complete. A side view of the structure, figure 4.11 b, reveals a uniform layer thickness and porosity from the bottom to the top. A zoomed-in corner picture allows for measurements of the cubical pore, which were found to be approximately 40μm as intended.

However, the layer thickness was found to be around 40-50µm, indicating some degree of over-curing. The measurements of the pore size of every layer are listed in the figure 4.12 below. Nevertheless, this result demonstrates that the printer is capable of printing porous structures with a 40µm layer thickness. It should be noted that the structure experienced some expansion during the washing process, resulting in a change in shape. This is consistent with the other results presented earlier. Further research is needed to confirm the minimum layer thickness hypothesis, but this experiment shows promising results for printing 6S structures with a 40µm pore size.

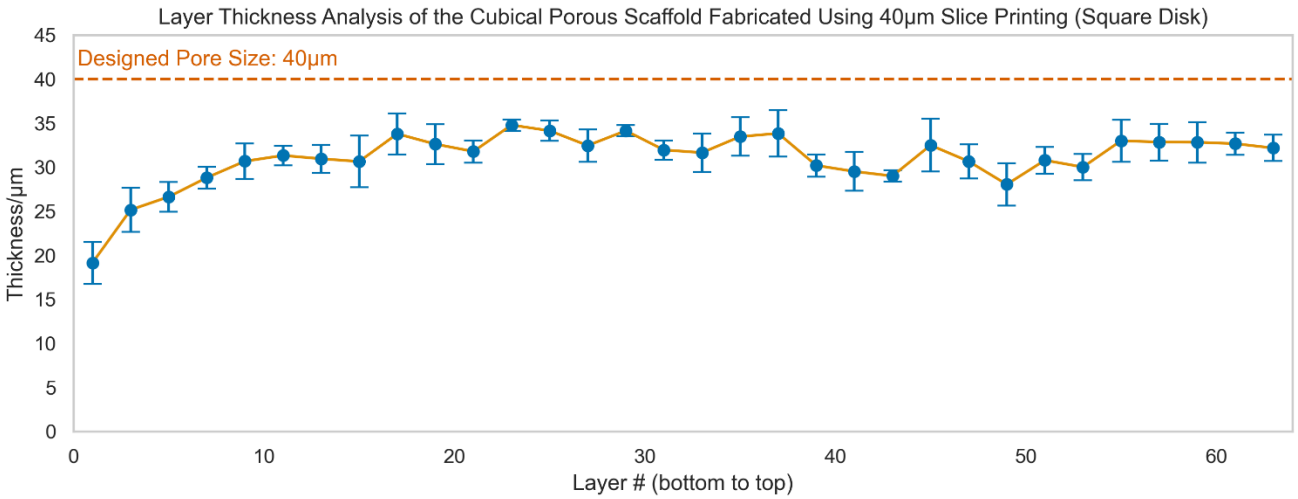

Figure 4.12. the measured pore size of the MS scaffold with 32 µm interconnects from bottom to top

With the objective in mind to create a 40 µm geometric structure that might show superior healing upon implantation, a cubical unit incorporating a 40 µm cubical void was designed and subsequently printed, as depicted in Figure. This unit can be divided into two repeatable printable slices. In contrast to the MS unit, it lacks smaller interconnects, with the pore size serving as the interconnect dimension. While not the original intended architecture, this design serves as an effective means to assess the PDMS print surface performance and identify an optimal layer thickness for precise printer control.

To assess the printer's precision in fabricating 40 µm-thick layers, a cylindrical porous scaffold measuring 5mm (X) × 5mm (Y) × 2mm (Z) was created using cubical units, as depicted in Figures a and b below. The initial layer was used as the base and printed at a modulation of 50% and a velocity of 50 mm/s. The remaining scaffold was printed using a modulation of 35% and a velocity of 60 mm/s, resulting in a consistent layer thickness of 40 µm and a total fabrication time of 5 hours. Following printing, the scaffold underwent two consecutive isopropanol rinses lasting 1 hour and 24 hours. Illustrated in Figure 4.13, the entire structure was successfully printed. Zoomed-in views, presented in Figures 4.13 b and c, provide detailed top and side perspectives of the scaffold, confirming accurate structure replication and pore dimensions as intended. As illustrated in Figure 4.13 d, a cross-sectional view of the scaffold revealed that while the inner structures remained porous, slight over-curing in the middle caused the pore size to be smaller than the outer pores. In Figure 4.14, which is the measurement result, all pore sizes except for the 10th layer demonstrated consistent 40 µm dimensions, possibly attributed to volume shrinkage around that layer. Overall, the printed scaffold demonstrated the printer's proficiency in generating 40-µm-thick layers, surpassing the minimum required layer thickness as hypothesized earlier.

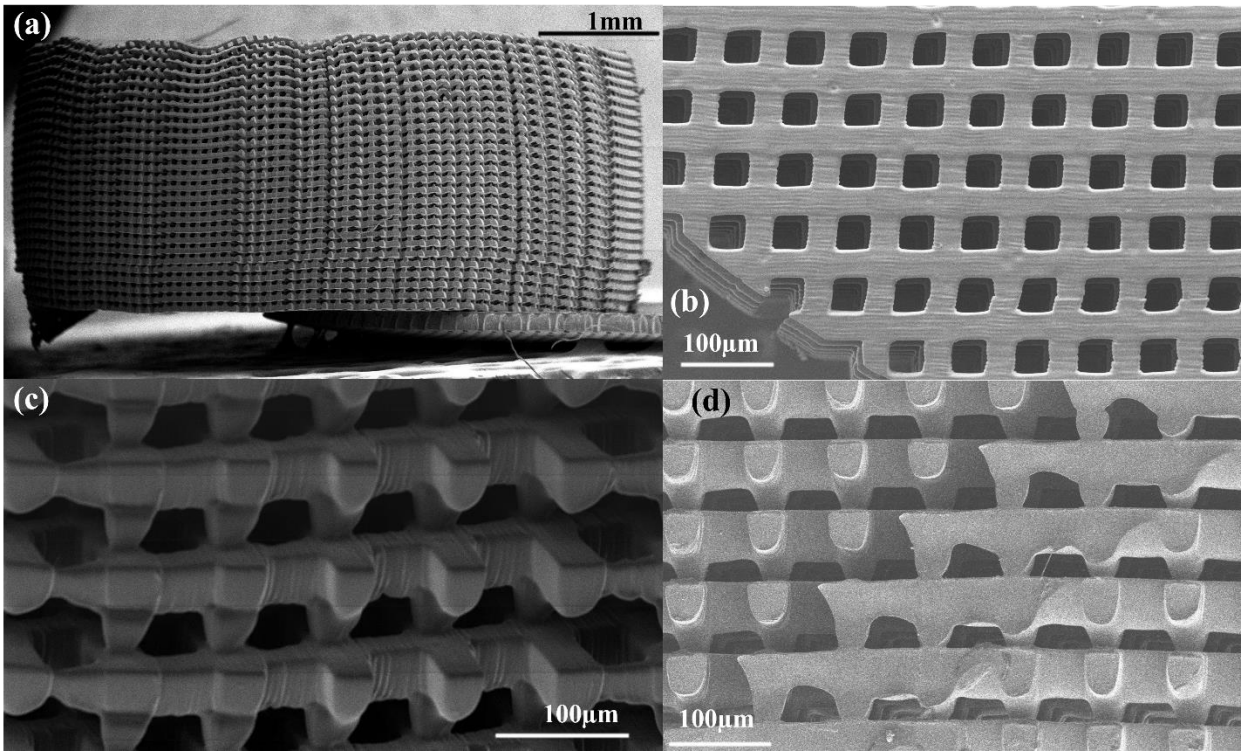

Figure 4.13. the implantable scaffold with cubical pores, (a) the side view, (b) the corner top view, (c) zoom-in side view, (d) the cross-section view after cutting in half

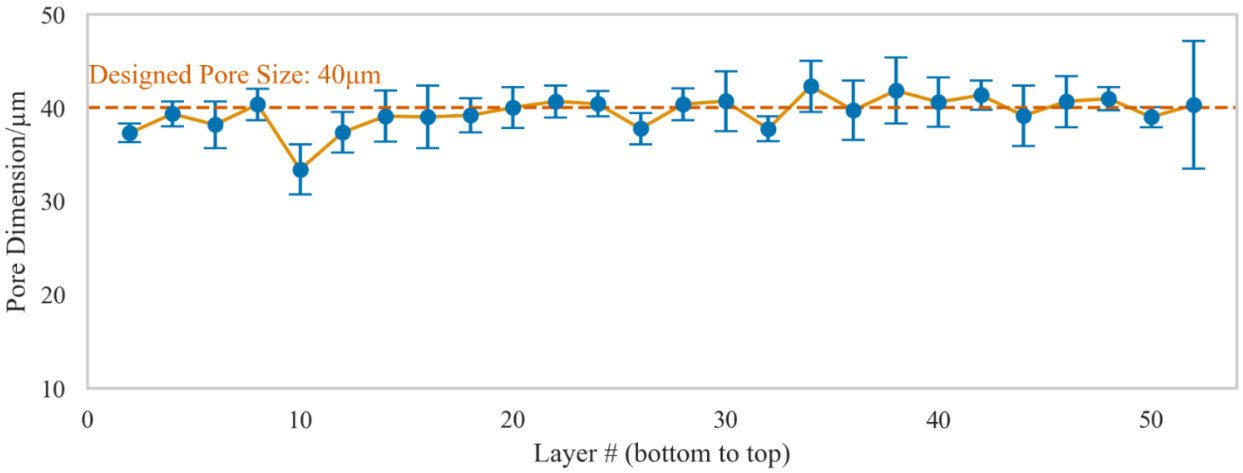

Figure 4.14. the measured pore size of the cubical scaffold with 40 µm layer thickness from bottom to top

Two complex cubical porous structures, a UW-shaped and a CDI-shaped structure, were designed and printed to test the printer's capability of producing cubical porous structures with intricate shapes. The structures were printed with 31% modulation and 60mm/s velocity, and the results are depicted in the figure 4.15 and 4.16 below. It should be noted that the I in the CDI-shaped structure appears slightly altered due to unattached pillars between layers during the printing process, which were subsequently washed out during the washing process, causing changes in the overall structure. Nevertheless, both the UW-shaped and CDI-shaped structures demonstrate that complex structures with non-straight edges on the X-Y plane can be printed with a layer thickness of 40μm. The absence of significant surface contamination with these printing parameters proves that the laser dose is above the minimum amount required to ignore surface contamination.

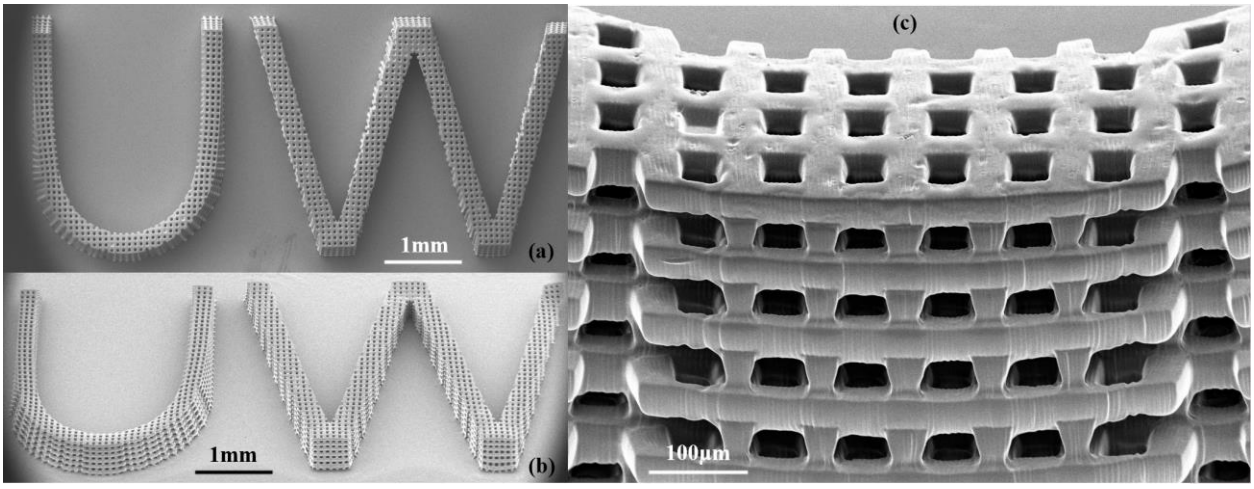

Figure 4.15. the UW-shaped cubical porous structure, (a) the top view, (b) the inclined top view, (c) the zoom-in view of the letter U

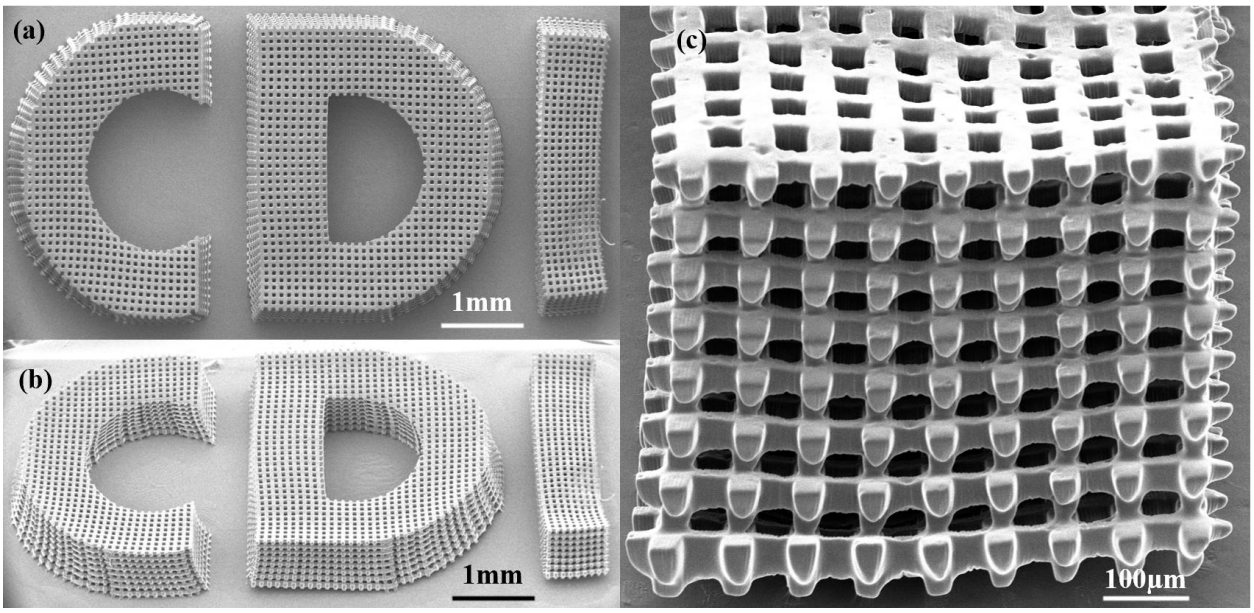

Figure 4.16. the CDI-shaped cubical porous structure, (a) the top view, (b) the inclined top view, (c) the zoom-in view of the letter I

The CDI-shaped and UW-shaped structures were employed to assess the printer's capability in maintaining layer thickness stability during the fabrication of intricate structures with complex X-Y plane edges. The UW-shaped structure features narrow walls, while the CDI-shaped structure incorporates thicker walls. It is noteworthy that, as depicted in both Fig. 16 a and b, the letter "I" within the CDI-shaped structure displays slight distortion due to pillars that were not properly attached between layers during the printing process. These unattached pillars were subsequently removed in the washing step, resulting in deformation. However, both the UW-shaped and CDI-shaped structures showcase the printer's ability to produce intricate designs with non-linear X-Y plane edges using a layer thickness of 40 μm. The absence of substantial surface contamination under these printing conditions indicates that the laser dosage has been optimized to mitigate the impact of surface contaminants.

In order to showcase the printer's capability to print porous structures with non-straight edges in the Z direction, the CDI-shaped structure was rotated 90 degrees and printed vertically using a

modulation of 31% and a velocity of 60mm/s. The resulting structure is depicted in Figure 4.17, which confirms that the printer can fabricate complex porous scaffolds in all three dimensions, namely X, Y, and Z directions.

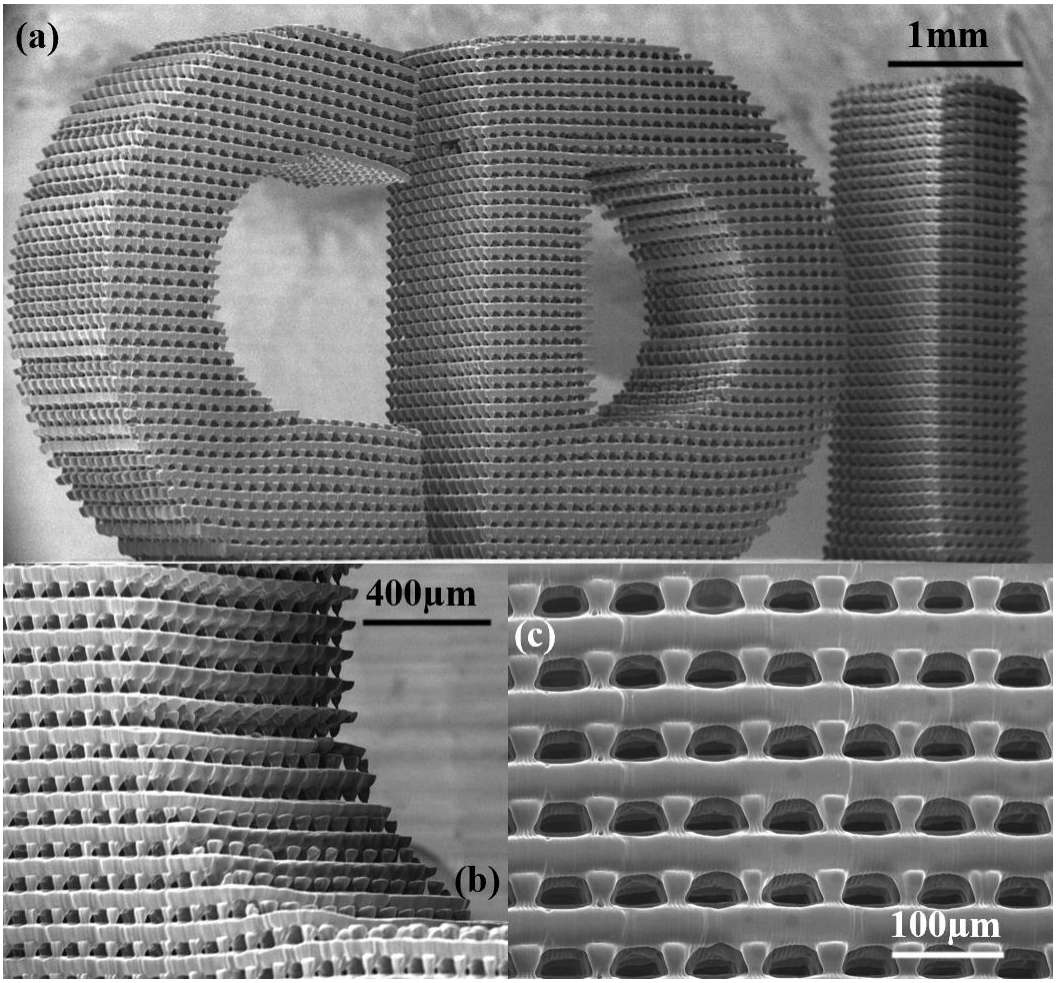

Figure 4.17. the vertical CDI-shaped cubical porous structure, (a) the front view, (b) zoom-in view from the inner side of C, (c) the zoom-in view of the letter I

Based on the results presented above, it can be observed that the printer's ability to print pillar-like shapes with precise control of layer thickness can result in the transformation of the initial rectangular cube design into trapezoidal or triangular side surfaces. This phenomenon can be attributed to the Gaussian wave of the laser beam used in SLA printers, where the wave width is extremely narrow, resulting in a combination of multiple beams that often produce a rectangular

cube shape. However, controlling the layer thickness to prevent over-curing may lead to smaller actual sizes at the upper end of the same layer than the lower end, resulting in trapezoidal or triangular side surfaces, which could compromise the cubical pore shape.

While this suggests that the laser beam is being controlled to the extreme, the presence of surface contamination can lead to insufficient energy at the peak of the wave, resulting in incomplete solidification and layer collapse. Hence, a degree of over-curing is necessary to ensure the overall structure's stability.

The comparison of the pore size measurements for the 3 complex structures printed with the cubical pores is listed in the figure 4.18 below. From Figure 4.18, it is evident that while the layer thickness remains relatively consistent across the three structures, the actual pore size of the narrower walls, represented by the UW-shaped structure, is smaller compared to the thicker walls of the CDI-shaped structures. This discrepancy suggests that the UW-shaped structure, despite being printed with the same laser intensity, encounters over-curing issues. This phenomenon could be attributed to the fact that, with areas already polymerized by the laser, smaller structural dimensions will experience a higher frequency of laser exposure nearby. This increased frequency raises the likelihood of additional laser energy affecting those regions, leading to over-curing.

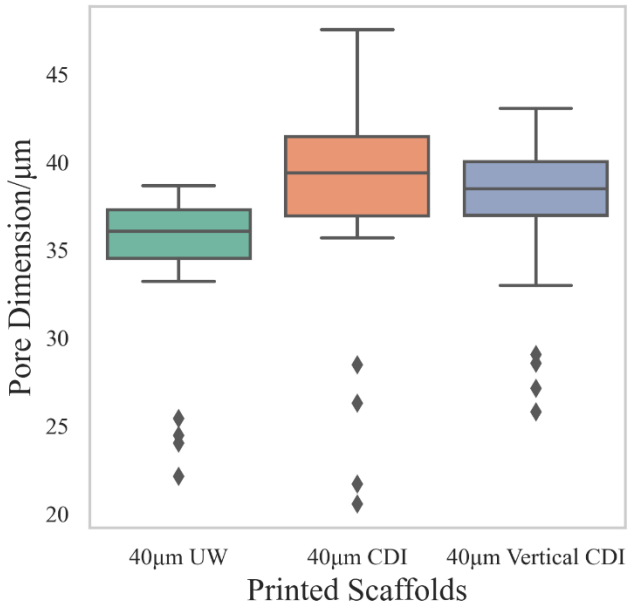

Figure 4.18. Box plot for cubical pore size distribution of these 3 structures

Consequently, even though the theoretical layer thickness may be the same across different structures, the required laser intensity varies due to their distinct dimensions. Through experimentation, we noted that the structures can be reprinted with a range of laser intensities and the result is stable. Remarkably, the actual layer thickness exhibits relatively small variation between layers, with no layer thickness fluctuations as shown in Figure 4.14, suggesting that the surface contamination can be ignored in this instance.

The comparison of actual cubical pore size distribution, as depicted in Figure 4.19, reveals that under identical printing conditions, a 32 µm layer thickness does not consistently maintain the designated value. However, a modest 25% increase in the designed layer thickness to 40 µm significantly enhances stability. Despite some fluctuations in actual layer thickness under the same printing conditions, structural stability remains unaffected. Furthermore, elevating the layer thickness to 64 µm results in further improvement in stability.

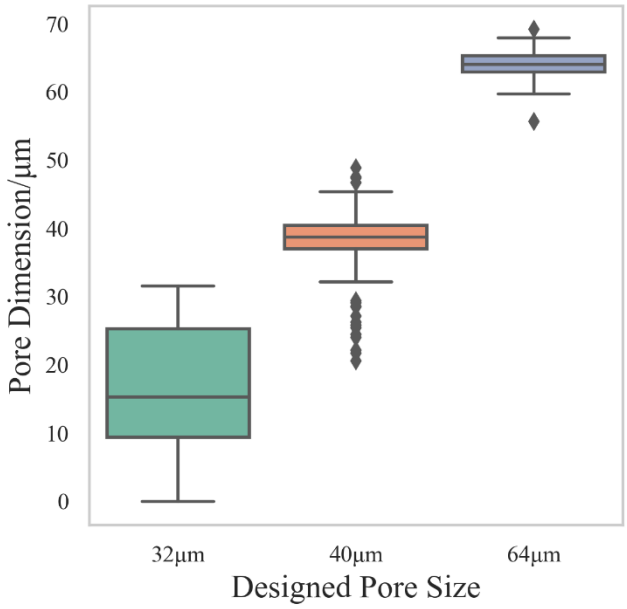

Figure 4.19. Box plot for cubical pore size distribution of different printing layer thicknesses

Currently, our research endeavors are focused on investigating printer stability and reproducibility when printing structures with dimensions below 40 μm. Nevertheless, the viability of maintaining a layer thickness of 40 μm has been convincingly demonstrated through the successful printing of these three intricate structures.

4.4 CONCLUSIONS

In this chapter, we have demonstrated the effectiveness of the methods proposed in Chapter 2 in addressing both internal and surface contamination issues when using SLA printers. These methods have been shown to be compatible with most vat polymerization techniques using PDMS vat coating and can help achieve optimal performance. We have fabricated two cylindrical-shaped porous scaffolds with Menger Sponge units using our improved method, one with 96μm side-length cubical pores with 32μm interconnects, and the other with 192μm side-length cubical pores with 64μm interconnects.

Our results show that micrometric periodic features down to 64μm and actual layer thickness down to 32μm can be achieved using SLA techniques. However, when the layer thickness is reduced to 32μm, surface contamination becomes a significant issue. Our hypothesis is that the building laser intensity for 32μm is below the minimum laser intensity required to avoid surface contamination, and we recommend further research to verify this hypothesis.

The present study has successfully fabricated a square-disk-shaped scaffold with a 40μm pore size, utilizing the improved method proposed in Chapter 2. Our research has demonstrated that our method can effectively produce structures with 40μm slices while accounting for the challenge of surface contamination.

Furthermore, our improved method has exhibited the capability of fabricating complex architecture with non-straight edges in all three spatial directions (X, Y, and Z) utilizing a 40μm layer thickness. The UW-shaped and CDI-shaped models were successfully printed, and their structures demonstrated sufficient robustness against the printing process.

We also have successfully fabricated a porous scaffold with cubical units at micron resolution with a size and shape appropriate for animal implantation. This scaffold was printed with 40μm layers, and the potential for its use in material science, biomedical engineering, and device design was demonstrated. The animal study is described in Chapter 6.

In conclusion, our improved method for addressing internal and surface contamination issues in SLA printing has shown promising results, and further research can lead to even more advanced fabrication techniques in the future.

Chapter 5. DEVELOPMENT OF PHOTO-CURING RESIN FOR HIGH-RESOLUTION 3D PRINTING

5.1 INTRODUCTION

To enhance the potential of SLA 3D printing in biomedical applications, it is essential to develop a more suitable resin, as the primary material used in previous chapters, DS2000, is a dental resin that may not be applicable in situations requiring more elastic materials. In this context, we formulated several new resin options and evaluated their resolution performance using the KLOE 3D printing system as alternatives to DS2000.

Resin formulations for SLA 3D printing consist of three primary components: a monomer or liquid-polymer, a cross linker, a photo-initiator, and various additives[75]. The monomer or liquid-polymer is responsible for the bulk properties of the material, such as strength, toughness, and flexibility. The cross linker is added to promote crosslinking or the formation of chemical bonds between resin molecules, leading to a solid polymer network. The photo-initiator initiates the curing process when exposed to specific wavelengths of light, such as ultraviolet or visible light.

Polymer resins used in SLA 3D printing are typically based on acrylate or epoxy chemistry[76]. Acrylate-based resins are commonly used due to their fast curing time[77], low viscosity[78], and high accuracy[78], making them ideal for printing intricate parts with fine details. Epoxy-based resins, on the other hand, are more durable and have higher temperature resistance, making them suitable for printing parts that require high mechanical strength or heat resistance[79].

Poly(ethylene glycol) dimethacrylate (PEGDMA) is a hydrophilic crosslinking agent commonly utilized in vat photopolymerization, including SLA 3D printing, for fabricating biomaterials and tissue engineering scaffolds[80]. PEGDMA is known for its flexibility in tuning mechanical properties and porosity by varying its molecular weight and concentration, allowing for the creation of structures with desirable strength and elasticity, and it is been widely used in the biomedical field. Its high degree of crosslinking potential enhances the structural stability of printed parts, and also make it a suitable material for as the main material in a SLA formulation.

In our previous research we developed multiple formulation with 2-hydroxyethyl methacrylate (HEMA), while HEMA is a hydrophilic monomer commonly used in the production of dental and medical devices and is often used in SLA 3D printing resin formulation[70]. But among our previous experiments, the result is always blur and do not have a good sharpness of the contour, one possible reason for this might be the chain length. In this part of our study, we will use PEGDMA instead of HEMA, since over all its average chain length is higher than HEMA.

Photo-initiators used in SLA 3D printing include various types of organic or inorganic compounds that absorb light at specific wavelengths, such as benzophenone, Irgacure, or Darocur[81]. These compounds break down into free radicals when exposed to light, initiating the polymerization reaction that converts the liquid resin into a solid object. The main photo-initiators used in DLP or SLA are Diphenyl(2,4,6-trimethylbenzoyl)phosphine oxide (TPO), Omnirad 819, and Omnirad 1173[82]. The TPO is used in this part as the photo-initiators.

To reduce the photo sensitivity of the resin, additional chemicals such as photo inhibitors and photo absorbers are helpful. Photo inhibitors, also known as UV stabilizers or light stabilizers, absorb or reflect the UV radiation that initiates the polymerization process[67]. These compounds can be added to the resin formulation in varying concentrations depending on the desired level of

inhibition[76]. Butylated hydroxytoluene (BHT) is commonly used as a photo inhibitor in resin formulations for SLA 3D printing. It is a common antioxidant that prevents the photopolymerization process from occurring prematurely, which could result in unwanted solidification of the resin during storage or transportation. BHT works by scavenging free radicals that are generated during the photopolymerization process, which can cause chain termination and inhibit polymerization.

Photo absorbers play a crucial role in controlling the curing process of resin formulations that are sensitive to light. These compounds absorb the light and convert it into heat, which triggers the curing or hardening of the material[76]. In the context of SLA 3D printing, Tinuvin® 326, or BLS is a commonly used photo absorber in resin formulations. It is a chemical compound that converts UV light into heat and facilitates the curing process.

The purpose of this study is to experiment with the materials mentioned above to develop a resin formula that can print porous scaffolds quickly and accurately. The objective of the study is to achieve the optimal combination of monomer, crosslinker, photo-initiator, and photo absorber to produce a resin that can be used for the efficient and precise printing of porous scaffolds.

5.2 MATERIALS AND METHODS

5.2.1 *Materials*

All chemicals used in this study is mentioned here: Poly(ethylene glycol) Dimethacrylate (PEGDMA, Polysciences, 15178-100, 100 g), butylated hydroxytoluene (BHT, Spectrum, B1196, 125g), Diphenyl(2,4,6-trimethylbenzoyl)phosphine oxide (TPO, Sigma Alderich, CAS # 75980-60-8, 50 g), 2-tert-Butyl-6-(5-chloro-2H-benzotriazol-2-yl)-4-methylphenol (Tinuvin 326, or BLS, Sigma Alderich, 422479-50, 50g). The tested and analyzed resin formulations are listed in the tables

below. To better evaluate the performance, the DS2000 we used in the previous section is used here as a positive control.

Table 5.1. Tested PEDMA based formulas

formula #	PEGDMA	TPO	BLS	BHT
1	100%	1.00%	2.00%	0.00%
2	100%	2.00%	2.00%	0.00%
3	100%	1.00%	0.40%	0.00%
4	100%	2.00%	0.40%	0.00%
5	100%	0.50%	0.40%	0.00%
6	100%	1.50%	0.40%	0.00%
7	100%	2.00%	0.80%	0.00%
8	100%	1.50%	0.40%	0.05%
9	100%	1.00%	0.40%	0.05%
10	100%	2.00%	0.40%	0.05%

5.2.2 *Printability test*

To assess the printability of the formulation and minimize fabrication variability associated with differing laser parameters (modulation and velocity), a sensitivity test was conducted. Printability is confirmed if at least one square is successfully printed. The methodology for the sensitivity test is detailed in Section 2.2.3. However, due to formulation degradation and its impact on PDMS, some data currently lack repeatability.

5.2.3 *Resolution test (bar thickness test)*

To evaluate the resolution of the formulation, optimal parameters from the sensitivity test were used to 3D print single-layer bars of varying widths: 200 μm, 100 μm, 50 μm, 25 μm, 12 μm, and 6 μm, with a layer thickness of 40 μm. The schematic is presented in the figure 5.1 below.

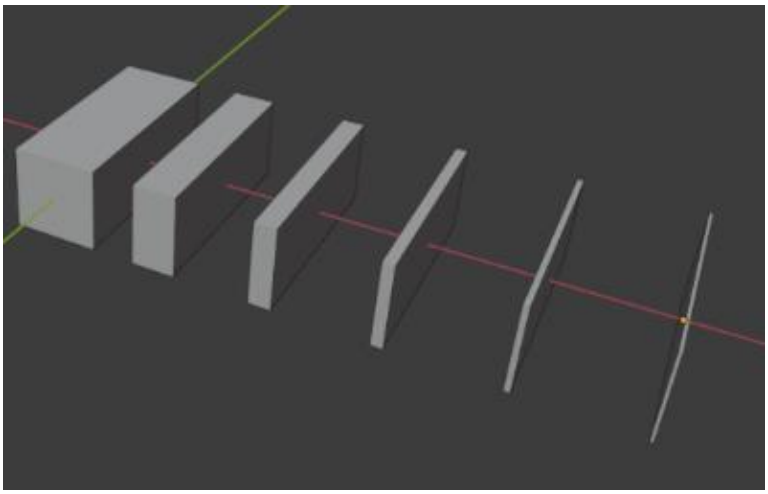

Figure 5.1. Schematic of the bar thickness test

5.2.4 *Bridge test*

To evaluate the controllability of the formulation, the bridge test described in section 4.2.3 is utilized here.

5.3 RESULT AND DISCUSSION

The printability and bar thickness results for the 10 formulations are shown in the table 10.2 below. In the resolution section, the highest visible resolution (listed in the bar section in the table below) denotes the smallest designed bar width that remains visible; however, this does not imply that the formulation achieves that precise resolution. In most cases, the surfaces of the printed bars appear blurred, making accurate measurement challenging, particularly for bars required higher resolution. This issue is especially pronounced for formulations #8 through #10, where the bar dimensions are difficult to assess.

Table 5.2. Printability and bar thickness tests results of PEDMA based formulas

Formula #	PEGDMA	TPO	BLS	BHT	Printability	Bar
1	100%	1.00%	2.00%	0.00%	No	\
2	100%	2.00%	2.00%	0.00%	No	\

3	100%	1.00%	0.40%	0.00%	Yes	6μm
4	100%	2.00%	0.40%	0.00%	Yes	6μm
5	100%	0.50%	0.40%	0.00%	No	\
6	100%	1.50%	0.40%	0.00%	Yes	6μm
7	100%	2.00%	0.80%	0.00%	No	\
8	100%	1.50%	0.40%	0.05%	Yes	100μm
9	100%	1.00%	0.40%	0.05%	Yes	100μm
10	100%	2.00%	0.40%	0.05%	Yes	100μm

The printability is defined as the ability of at least one combination of laser intensity and velocity to produce a square with visible, measurable edges on the sensitivity test, and is a specific definition in our study. This criterion integrates the essential requirements for a 3D printing resin: the ability to form bulk structures and achieve fine resolution, making it suitable for SLA printers. Leveraging the SLA printer's process of line-by-line, layer-by-layer fabrication, we can print a series of squares with varying laser doses on the same surface. Though smaller in size, this approach enables finer detail resolution, which helps us identify and eliminate factors that could lead to manufacturing failures.

Our results indicate that PEGDMA with the photo initiator (TPO) concentration of 1–2%, 0.4% photo absorber (BLS), and 0–0.05% photo inhibitor demonstrates printability suitable for high-resolution SLA printing. Additionally, formulations without BHT exhibit better bar thickness results and higher print resolution.

The measured widths of all visible bars from the bar thickness test are shown in the figure below. Only the results from formulations #3, #4, and #6 are meaningful and repeatable across three parallel tests, while formulations #8–#10 exhibit blurred surfaces, making certain bar widths unmeasurable. Although some formulations produced bars that were both visible and measurable, a comparison with DS2000 highlights persistent issues in our formulations, including surface blurriness and limited edge sharpness

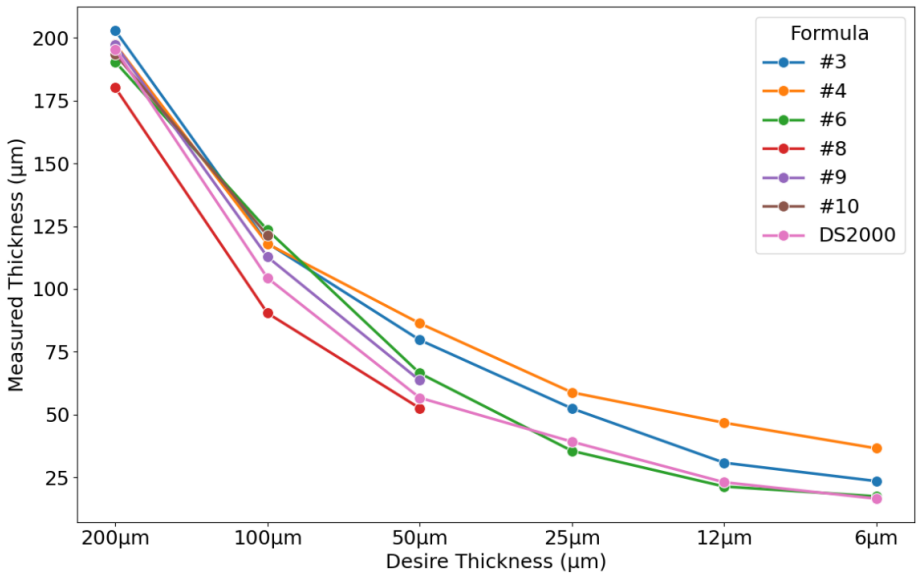

Figure 5.2. Measurement results for the bar thickness tests for different formulas

In the bar thickness test, some formulations lack a clear edge when bar widths are below 100 µm, resulting in missing data points for these measurements. Most formulations successfully print bars between 200 µm and 50 µm; however, none of the formulations containing BHT achieve visible, measurable edges for bars below 50 µm, whereas all BHT-free formulations produce visible results. Notably, formulation #6 shows comparable resolution to the positive control, DS2000. However, when attempting to print a 6 µm bar with DS2000, the measured width is approximately 16 µm. Previous research suggests that the DS2000's maximum resolution on the KLOE SLA printer is around 5 µm, indicating possible over-curing in the X-Y plane, which could be causing the bars to appear thicker than their intended dimensions.

The examples from the bar thickness test are shown in figure 5.3 below. It is evident that the results from formulations #8–#10 exhibit significant blurriness compared to the control and the other formulations. This suggests that BHT may play a critical role in reducing the resolution of our resin system.

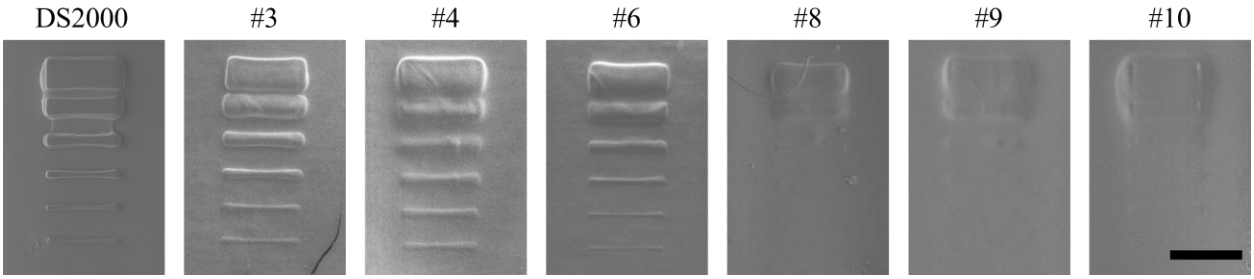

Figure 5.3. Examples of the bar thickness test result (scale bar = 500 μm)

While the overall results indicate that formulation #6 performs the best, one of our initial tests revealed that formulation #3 achieved the highest resolution, with a bar thickness of only 8.43 μm, as shown in the figure 5.4 below. However, this result was not repeatable in subsequent trials. This finding underscores that, although the resin formulation exhibits high resolution and good printability, it lacks sufficient stability for consistently fabricating structures with high repeatability. Consequently, the data presented in our resolution tests may require further validation to confirm its reliability.

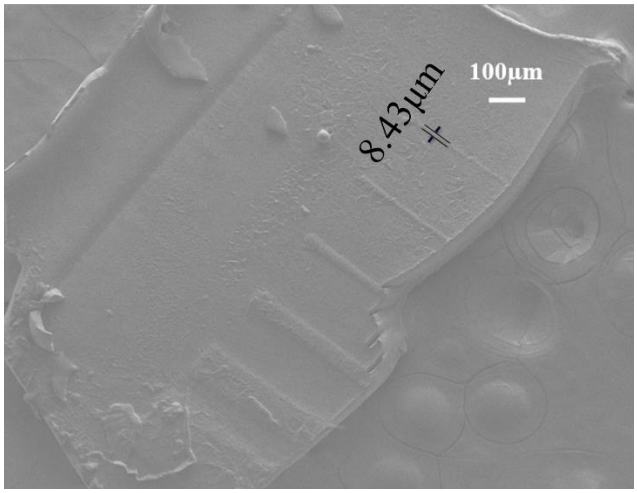

Figure 5.4. result of the #3 formulation's bar thickness shows the thinnest bar with the width 8.43 μm

Only formulations #3, #4, and #6 underwent the bridge test to evaluate their controllable performance, with part of the results displayed in the figure below. Both #3 and #6 demonstrate

low controllability, as the actual layer thickness increases significantly with only a small variation in laser intensity. In contrast, formulation #4 exhibits a wider controllable range. However, due to poor repeatability in the bridge test, meaningful measurements cannot be obtained for these formulations.

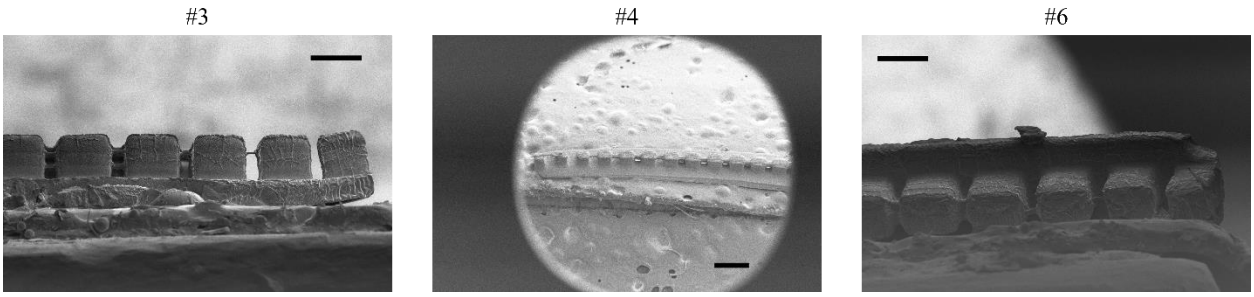

Figure 5.5. result examples of the first round of bridge test (#3 and #6 scale bar = 200 μm, #4 scale bar = 500 μm)

Among the three formulations, #4 contains the highest concentration of photo initiator, suggesting that a concentration greater than 2% may be beneficial for improved control. However, when comparing the bar thickness test results, #4 exhibits the lowest resolution compared to formulations #3 and #6. This indicates a potential trade-off between resolution and controllability, highlighting the need for further investigation into this formulation system.

Based on all the experiments conducted, we found that while some results indicate that our formulations exhibit high resolution and good controllability, most outcomes lack the ability to be reliably re-validated. This inconsistency may stem from fluctuations in the concentration of the main components during the printing process, which can lead to a decline in performance after a manageable duration. To enhance the reliability of our formulations, the development of a buffer system may be necessary, and this will be a focus for further study.

5.4 PRELIMINARY CONCLUSIONS

The options for high-resolution resins suitable for vat photopolymerization, particularly in biomedical applications, are limited. In this study, we systematically evaluated a series of formulations using Poly(ethylene glycol) dimethacrylate (PEGDMA) as the primary material, butylated hydroxytoluene (BHT) as the photo inhibitor, Diphenyl(2,4,6-trimethylbenzoyl)phosphine oxide (TPO) as the photo initiator, and 2-tert-Butyl-6-(5-chloro-2H-benzotriazol-2-yl)-4-methylphenol (BLS) as the photo absorber. Formulations containing 1-2% TPO and 0.4% BLS exhibited strong performance in resolution, achieving a maximum resolution of approximately 8 μm, comparable to the high-resolution SLA resin DS2000. Additionally, the PEGDMA formulation with 2% TPO and 0.4% BLS demonstrated good controllability, highlighting the potential of this formulation system for further applications in high-resolution vat photopolymerization. While re-validation remains a challenge for high-volume use of these formulations, their capability to achieve high-resolution results presents a promising opportunity for further development in the field of vat-based 3D printing, and the stability of the formulation will remain as a future study.

Chapter 6. EVALUATION OF THE IN VIVO PERFORMANCE OF POROUS SCAFFOLDS

6.1 INTRODUCTION

Porous scaffolds play a critical role in tissue engineering[62, 65, 83] and regenerative medicine applications[64, 84, 85], as they provide a supportive structure for tissue regeneration[35, 63], reduce the foreign body reaction (FBR)[30, 86-88], and enhance integration into host tissue[15, 89]. These materials feature interconnected pores that facilitate cell attachment, proliferation, and differentiation, while permitting the exchange of nutrients and waste[22]. The pore structure within these biomaterials is crucial in minimizing FBR, with pore size, shape, and interconnectivity significantly influencing immune cell infiltration and extracellular matrix deposition.

There are various methods for fabricating porous structures. Typically, creating porous biomaterials involves forming an interconnected pore network. Common scaffold fabrication techniques include salt-leaching[36, 37], gas-foaming[38, 39], electrospinning[40, 90], freeze-drying[41, 91], and 3D printing[54, 92]. Apart from 3D printing, these methods generally don't provide precision control of porous structure.

In contrast, 3D printing, or additive manufacturing, offers a direct fabrication approach, allowing precise control over pore size, shape, and distribution[93]. This layer-by-layer method facilitates the creation of intricate, customizable structures with high resolution and accuracy[94]. However, traditional 3D printing methods fail in producing high resolution scaffold with porous structure in the tens of micron level.

Multiple reports from the University of Washington indicate that scaffolds with 40 μm interconnected spherical pores can reduce foreign body capsule (FBC) formation, enhance cell infiltration, and promote vascularization, probably by modulating macrophage phenotypes in a pore size-dependent manner[35, 64, 65, 89, 95]. However, this scaffold fabrication used a porogen method (illustrated in Fig. 1a), which is time-consuming and requires custom-made molds for complex shapes, limiting its broader applicability. Previously, we reported success in fabricating scaffolds with 40 μm interconnected cubical pores. Considering the importance of pore shape and size in cellular response, it is valuable to determine whether scaffolds of similar pore size but different shapes elicit comparable tissue responses. Such findings could provide insights into the scaffold's potential as a customizable and effective tissue regeneration solution.

In this study, we demonstrated the first application of high-resolution 3D printing in manufacturing precision porous scaffolds and their structure dependent, enhanced biocompatibility. Specifically, we employed the original porogen method to fabricate scaffolds with 40 μm spherical pores (as a positive control for good biocompatibility) and used an advance vat photopolymerization 3D printing to produce scaffolds with 40 μm cubical pores, as well as non-porous slabs (as a negative control). These scaffolds were then implanted into a mouse model to assess the FBR to different scaffold structures, as shown in Fig. 6.1. Explants were examined using basic histology to analyze the cellular response. 3D printed scaffolds with 40 μm cubical pores substantially reduce the thickness and density of FBC, promote regenerative cell infiltration and vascularization compared to non-porous slabs, in a similar fashion to the traditionally fabricated scaffolds with 40 μm spherical pores. With the additional versatility of printing in all macroscopic shapes and forms combined with enhanced biocompatibility of 40 μm microporous

structure, the high-resolution 3D printing demonstrated in this study has the potential of revolutionizing customized tissue engineering, biomedical devices, and regenerative medicine.

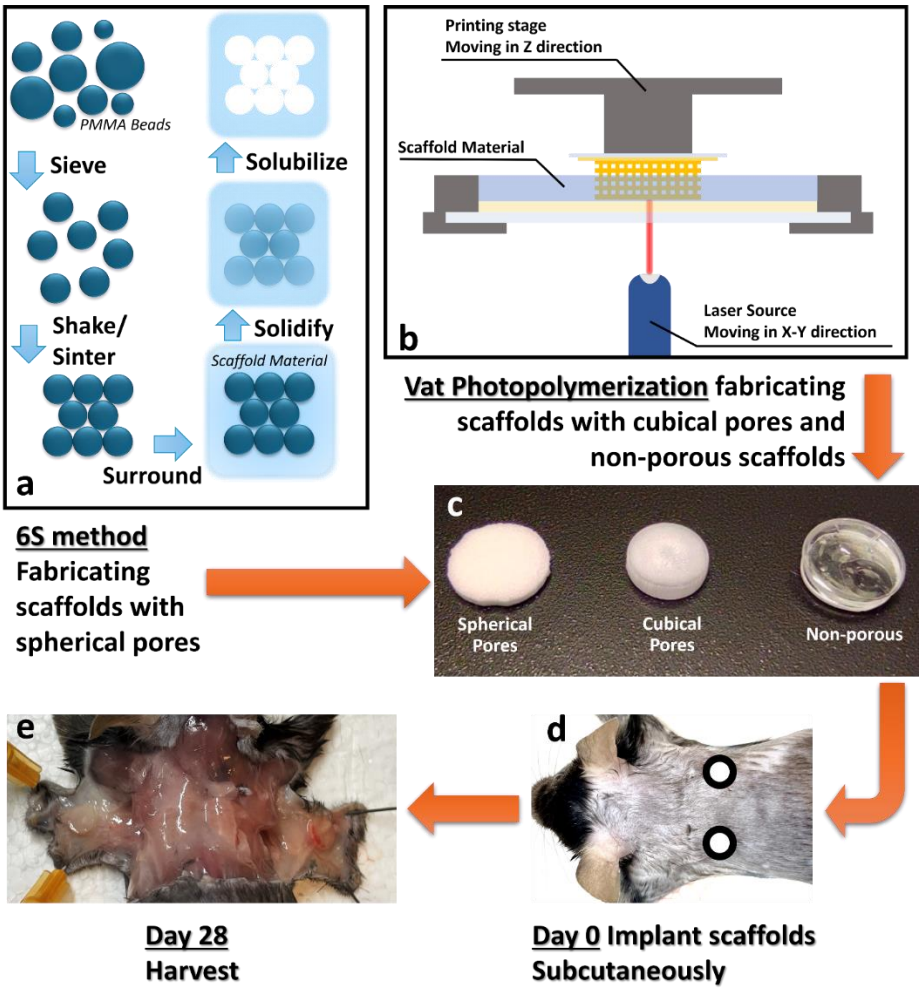

Figure 6.1. Schematic overview of the study process. (a) Diagram of the 6S fabrication method, illustrating the step-by-step production of porous scaffolds with spherical pores. (b) Schematic of the vat photopolymerization technique used to create scaffolds with 40 µm cubical pores and non-porous scaffolds. (c) Image of the implant samples, showing (from left to right) the 6S spherical pore scaffold, the cubical pore scaffold, and the non-porous scaffold. (d) Schematic representation of the subcutaneous implantation sites in the mouse model. (e)

Example of an explant, demonstrating integration of the implants with the surrounding tissue, cubical pores scaffold on the left while spherical scaffold on the right.

6.2 EXPERIMENTAL SECTION

6.2.1 *Materials*

A commercial acrylic-based 3D printing resin, VITRA DS2000 (DWS, Lot# 2302721, Thiene, Italy), was used to fabricate all the scaffolds and non-porous control in this study. To create the PDMS print surfaces used in the monomer vat for 3D printing, a Sylgard-184 silicone elastomer kit (Catalog# 24236-10, Lot# 220808, Dow Chemical Co, Hatfield, PA, USA) was employed. The porogen, or beads, for fabrication of precision-engineered porous scaffolds are poly(methyl methacrylate) (PMMA) beads (40 µm, Microbeads AS, Skedsmokorset, Norway).

6.2.2 *Fabrication of precision-engineered porous scaffolds with spherical pores*

Scaffolds with uniform 40 µm spherical pores were fabricated using an optimized version of a previously developed protocol. 40 µm PMMA beads were poured into a 75 × 25 × 1 mm^3 rectangular mold, which was made using glass slides separated by a 1-mm-thick Teflon spacer and secured with metal binder clips. The filled mold was placed in a glass beaker and sonicated for 30 minutes to achieve close packing of the spherical beads.

Following sonication, the packed microspheres were sintered at 179 °C for 24 hours, so that they become interconnected. To confirm that the interconnections between the spheres were approximately one-third of their diameter, the breaking edge of the heat-treated microsphere templates were examined using scanning electron microscopy (SEM). The qualified templates were then infiltrated with DS2000 monomer solution and degassed twice in a -25 mm Hg vacuum, each time for 5-minute interval to remove air bubbles. The templates were subsequently exposed

to 365 nm UV light in an XL-1500 UV Crosslinker (Spectro-UV, Spectroline) for a total of 12 minutes, with 6 minutes of illumination on each side.

After crosslinking, a razor blade was used to remove the thin films that had formed between the scaffold and the glass substrates. The scaffold was then soaked in acetone six times at 15-minute intervals, followed by gradual changes to 70% ethanol over three days, with three changes at 2-hour intervals. This ethanol was gradually replaced with deionized water under the same conditions. The scaffolds were stored in a 4 °C refrigerator. Prior to implantation, 1 mm-thick 6S scaffolds were punched out using 5 mm skin biopsy punches (Acu-Punch®, Acuderm Inc) and kept in PBS solution with penicillin-streptomycin at 4 °C.

6.2.3 *Fabrications of non-porous slab and porous scaffolds with cubical pores via 3D printing*

The non-porous slabs and scaffolds with 40 μm cubical pores were fabricated using a KLOE high-resolution 3D lithographic laser system, a vat photopolymerization 3D printer equipped with a 375 nm laser. Non-porous slabs were 3D printed using vat photopolymerization, with a fabrication layer thickness of 60 μm, a laser intensity (modulation) set to 70%, and a velocity of 60 mm/s. Nine solid scaffolds were fabricated simultaneously as a batch, with an approximate fabrication time of 15.5 hours per batch. Cubical porous scaffolds were fabricated using a layer thickness of 40 μm, laser intensity (modulation) set between 33% and 35%, and a velocity of 60 mm/s, with each implant taking approximately 2.5 hours to complete. 24 samples were successfully fabricated. After printing, the samples were subjected to two isopropanol rinses—first for 10 minutes, followed by 24 hours—to effectively remove any uncured resin from the surfaces. The samples were then air-dried at room temperature for an additional 24 hours. This washing process can be adjusted according to the complexity of the scaffold structure.

6.2.4 *Scanning electron microscopy (SEM)*

3D printed samples and test specimens sputter coated with gold were imaged using a SNE-3200M Scanning Electron Microscope (SEM) with an acceleration voltage at 5 kV.

6.2.5 *Pore size measurements via ImageJ*

ImageJ software was utilized to assess the pore sizes of the scaffolds based on SEM images and the corresponding scale bars. Since the outer surface of the scaffold is the primary interface with surrounding tissue post-implantation, only the pore size of this outer surface was measured. Three samples of each scaffold type—those with 40 µm cubical pores and those with 40 µm spherical pores—were randomly selected, and pores were randomly chosen and measured on each sample.

6.2.6 *In vivo experiment in mice*

All animal experiments were approved by the University Animal Care and Use Committee (IACUC) and conducted in accordance with the National Institutes of Health guidelines for the care and use of laboratory animals. Male C56Bl/6 mice, (aged 10-12 weeks, weighing 20-25 g, vendor Charles River) were maintained in standard housing in a temperature and humidity-controlled vivarium on a 12-hour light-dark cycle. For implantation surgeries, each mouse was anesthetized via 3-5% isoflurane inhalation and both right and left scapular regions were shaved and disinfected with alternating washes of betadine and 70% ethanol. Bilateral subcutaneous pockets were created through blunt dissection, each pocket receiving a single randomized implant. Incisions were closed with wound clips. A single dose of 0.05mg/kg buprenorphine was administered intraperitoneal to manage post-operative pain. The mice were then returned to

housing. Weight and health were monitored for 4 weeks, during which no signs of discomfort, inflammation, or weight loss were observed.

Implant surgery was performed on 9 mice and 1 mouse was culled during the 4-week incubation period due to a compromised incision site. Mice were euthanized via CO2 overdose followed by cervical dislocation. The implant site was then shaved and the implants along with surrounding skin and underlying tissue were harvested, laid flat in histology cassettes, and submerged in 4% formalin solution for 24-48 hours at room temperature with gentle agitation. The final harvest yielded 3 pairs of disks comparing cubical pores to non-porous scaffolds and 5 pairs of discs comparing cubical to spherical pores.

6.2.7 *Implant harvesting and processing for histology*

The fixed implants were then transferred into 50% ethanol, followed by 70% ethanol, for 30 minutes each with gentle agitation. Subsequently, the implants were dehydrated, cleared, and paraffin-infiltrated using a tissue processor (Shandon Citadel 2000). They were processed through 95% ethanol (1 × 30 min), 100% ethanol (3 × 30 min), xylene (3 × 35 min), and paraffin (2 × 1 hour).

Next, the implants were submerged in liquid paraffin and subjected to a -25 inch Hg vacuum at 60 °C for 15 minutes to enhance paraffin infiltration. The implants were then removed from the vacuum, bisected through their diameters, and embedded in paraffin with the cut surfaces facing down, aligned perpendicular to the future sectioning blade. Embedded blocks were refrigerated overnight and kept on ice prior to sectioning into 5 µm thick slices using a microtome (LEICA RM 2135). Ribbons of approximately five sections were cut and floated on 33 °C deionized water. Blocks were placed on ice between cuts to maintain low temperature, which hardens the paraffin and improves consistency between the paraffin and the polyurethane. For quantitative analyses,

two or three sections—at least 120 µm apart—were collected on the same glass slide (Superfrost Plus). The slides were air-dried before being baked at 53 °C for 30 minutes. After cooling to room temperature, the sections were deparaffinized and rehydrated by sequential immersion in xylenes (3 × 5 min), 100% ethanol (2 × 3 min), 95% ethanol (3 min), 70% ethanol (3 min), 50% ethanol (3 min), and finally DI water (3 min). Histological staining was performed following rehydration.

One implant with spherical pores could not be located during the harvesting procedure. Consequently, the final harvested implants included 8 scaffolds with 40 µm cubical pores, 4 scaffolds with 40 µm spherical pores, and 3 non-porous slabs. As there are several prior studies comparing scaffolds with 40 µm spherical pores to non-porous scaffolds, this study will primarily focus on evaluating the performance of the 40 µm cubical pore scaffolds.

6.2.8 *Imaging the stained tissue sectioning*

All stained tissue sections were imaged using a Nikon E800 Upright Microscope, capturing images at magnifications of 4×, 10×, and 20×. Each image was saved in two versions: one with a scale bar and one without.

6.2.9 *FBC Thickness Measurement*

Masson's trichrome (Sigma-Aldrich, REF: HT15-1KT) staining was performed on tissue sections from all explants. For each implant, six high-magnification fields were analyzed. A perpendicular line was drawn from the outer surface of the capsule to the interface with the implant using ImageJ, and measurements were taken using the scale bar associated with the section images. Six random measurements per section were obtained and averaged.

6.2.10 *Calculation of the collagen index (CI) and CI difference*

The collagen index (CI) was measured in all Masson's trichrome-stained sections. For each section, color information was collected from the skin, the FBC on the topside of the implant, and the FBC from the underside of the implant using the web application Trigit[96]. Utilizing the μ setting and the RGB color space, three rectangular pixel test points were taken from each tissue layer of interest while avoiding voids: the topside FBC, the underside FBC, and the skin. The resulting sets of red (R), green (G), and blue (B) values were recorded and averaged. The collagen index (CI) was calculated using Formula 1[97]. The schematic diagram of this method is shown in Figure 4a.

$$CI = \frac{B + G}{2R + B + G} \tag{6.1}$$

To eliminate the host response differences between different subcutaneous positions and measurement errors, we use the CI difference here to perform a better comparative analysis, which uses skin CI minus the FBC CI. The skin CI is also collected on the same tissue section to ensure the staining conditions remain the same. The formula is shown in Formula 2 below.

$$CI\ Difference = Skin\ CI - FBC\ CI \tag{6.2}$$

Since the skin normally contains more collagen than the FBC, we use the CI difference to evaluate the host response to the implant and the FBR extent. A higher CI difference indicates a lower level of collagen in the FBC, which means a less dense capsule.

This average data was then applied in the CI equation to calculate the collagen level for each area of the section, using three random measurements taken from each area. To further evaluate the FBC, the CI difference between the skin and the FBC was calculated for each section (3 measurements per section, with 3 sections per implant).

6.2.11 *H&E analysis of cellularization*

Rehydrated sections were stained with hematoxylin and eosin (H&E) following the manufacturer's protocol. To quantitatively analyze the degree of cellularization, H&E-stained slides were imaged and assessed using ImageJ. Due to the loss of some middle areas during the sectioning and staining processes, not all sections were analyzed. For each applicable section, three random measurements were taken by drawing a region of interest that focused on the pore area while avoiding transparent scaffold material. The area of this region was measured and calibrated using the scale bar on the section image, and the number of nuclei within that area was counted. Cell density was calculated as the number of nuclei per unit area. At least one section from each implant was selected for analysis.

6.2.12 *Data analysis and presentation*

After all data were collected, averages were calculated for each implant type and summarized using biological replicates to compare the performance of different scaffolds. Specifically, the sample sizes were as follows: scaffolds with 40 μm cubical pores (N = 8), scaffolds with 40 μm spherical pores (N = 4), and non-porous scaffolds (N = 3). All FBC measurements (technical replications) was also shown as plotted to show the distribution of the data points.

When comparing three scaffold types, an ANOVA test was conducted to assess overall statistical differences, while a t-test was used to evaluate statistical differences between pairs, if the ANOVA test shows a significant difference. For comparisons involving only two types of data, a Student’s t-test was performed to analyze statistical differences. The significance levels of the statistical results are represented in all plots as follows: $p > 0.05$, ns (not significant); $p < 0.05$, *; $p < 0.01$, **; $p < 0.005$, ***; and $p < 0.001$, ****.

6.3 RESULTS AND DISCUSSIONS

6.3.1 *Fabrication of precision-engineered porous scaffolds using 3D printing and traditional method*

To provide a chemically identical control for implant study, nonporous slabs (Fig. 6.1 c) were 3D printed via vat photopolymerization under identical conditions with the cubical porous scaffolds. The nonporous slabs were transparent and colorless (Fig. 6.1 c). Due to volume shrinkage during the drying process, samples may experience some mirror deformation or cracking; however, given the non-porous nature of the overall structure, minor cracking is acceptable and can still be used for implantation.

While 3D printing of solid scaffold disks is not as rapid as mold fabrication, it offers a rigorous control identically processed compared to the 3D printed scaffolds.

The schematic diagram of the scaffold with cubical pores is presented in Fig. 6.2. In this diagram, a represents the scaffold unit cell used to construct the entire scaffold file, with outer cube dimensions of 80 (X) × 80 (Y) × 80(Z) μm, inner pore dimensions of 40 (X) × 40 (Y) × 40 (Z) μm, and wall tunnel dimensions of 40 (X) × 40 (Y) × 20 (Z) μm. The final cylindrical implant model is depicted as Fig 6.2 b, measuring 5 (X) × 5 (Y) × 1 (Z) mm.

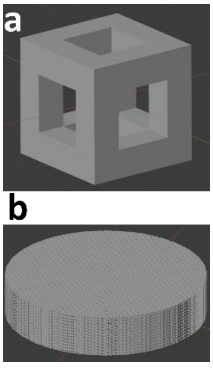

Figure 6.2. Digital schematic diagram of the 3D printed scaffold with 40 μm cubical pores, where a represents the cubical unit and b denotes the overall scaffold

The fabrication of the cubical pore scaffold with a 40 µm pore size has been detailed in our previous manuscript. The SEM images show precision printed, interconnected, cubical porous structure of the 3D printed scaffold (Fig. 6.3). The top view of the 3D printed scaffold (Fig. 6.3 a) shows a perfect realization of the designed cubical pore structure, with the multi-layer structure beneath the top surface is visible, indicating the overall porosity of the scaffold. The cross-section views of the scaffold (Fig. 6.3 a & b) confirm that this structure remains consistent throughout the entire thickness of the scaffold. The well printed, open, and uniform pore structure has a high potential for cellular ingrowth.

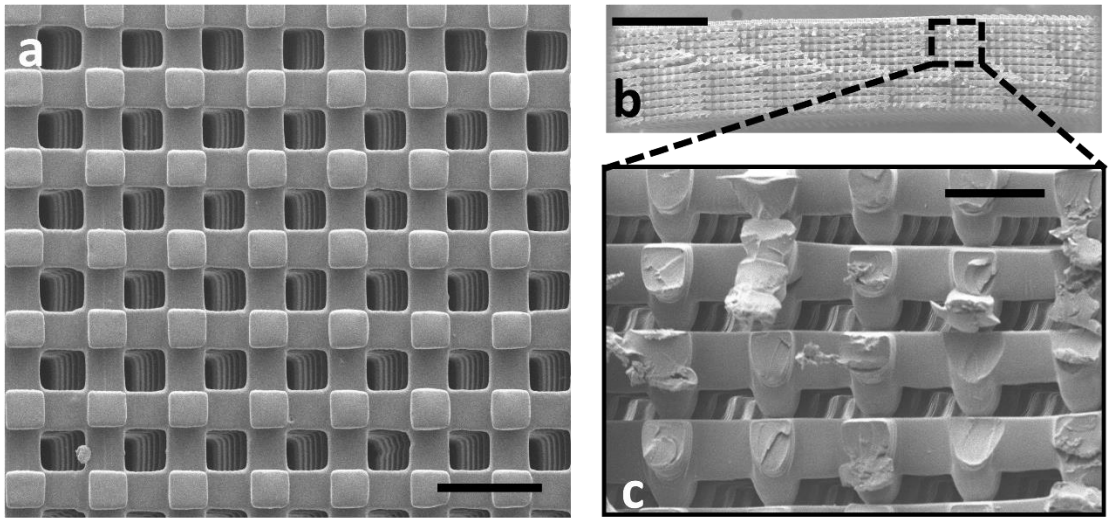

Figure 6.3. SEM images of the scaffold with 40 µm cubical pores: a shows the top view (scale bar = 100 µm), b presents the cross-sectional view (scale bar = 1 mm), and c provides a zoomed-in view of the cross-section (scale bar = 50 µm)

An examination of the cross-section of the scaffold with spherical pores (Fig. 6.4) reveals uniform, interconnected 40 µm pores throughout the whole scaffold. This porous structure has been repeatedly demonstrated to reduce FBC and optimize vascularization and cell infiltration.

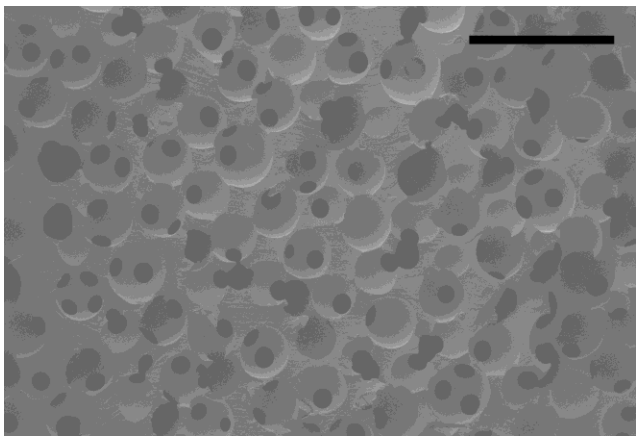

Figure 6.4. Cross-sectional view of the 6S scaffold (scale bar = 100 µm)

Quantitative measurements of both cubical and spherical pore scaffolds (Fig. 6.5) shows that the main dimensions are approximately 35-37 µm, with no significant difference between the two scaffold types.

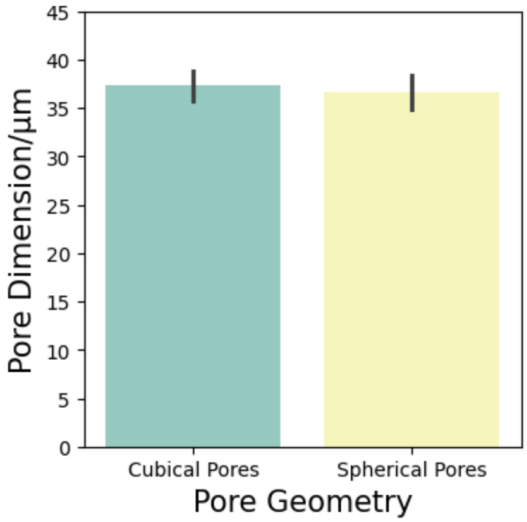

Figure 6.5. Comparison of pore dimensions between cubical pores and spherical pores

The use of 3D printing represents a significant advancement in the fabrication of precision-porous scaffolds, especially when compared to previous methods that were both time-consuming and lacked accuracy. No prior technique has demonstrated the ability to fabricate scaffolds of this

type with such high precision. Our approach marks a groundbreaking breakthrough, enabling the creation of high-resolution (<50 μm) porous scaffolds with exceptional consistency.

Most existing research on 3D-printed scaffolds for tissue engineering studies has focused on bone regeneration, where bone-forming cells typically require larger pores for integration, with optimal pore sizes ranging from 100–250 μm[98-100]. These larger pores are easier to fabricate using 3D printing techniques. However, research involving scaffolds with pore sizes below 100 μm is limited due to technical challenges. Although some research using inkjet 3D printing[56, 101] or melt electro writing[102] has achieved resolutions below 100 μm, these methods primarily focus on 2D structures or random structure, with irregular changes in the Z direction or no outlets on the scaffold's sides. Vat photopolymerization is currently the most suitable technique for fabricating scaffolds with regular, organized pores in all X, Y, and Z directions. However, due to challenges in cost, time, and repeatability, research on high-resolution scaffolds for *in vivo* studies remains limited, further underscoring the novelty of our study.

The fabrication time for the scaffolds with cubical pores is approximately 2.5 hours. While this is relatively fast compared to traditional methods, it may still be considered time-consuming for large-scale industrial applications. However, emerging 3D printing technologies like CLIP (Continuous Liquid Interface Production)[73] and CLEAR (Continuous-curing after Light Exposure Aided by Redox Initiation)[103], as highlighted in the reference research paper, offer potential avenues for significantly accelerating the fabrication process. Adapting these novel techniques to the fabrication of precision-porous scaffolds could lead to substantial time savings and open up new possibilities for creating complex and functional medical implants.

In summary, two distinct scaffold designs were successfully fabricated using different fabrication methods, their dimensions are comparable with each other with different pore shapes (cubical vs spherical).

6.3.2 *3D printed scaffold reduces FBC thickness*

To investigate the effects of pore shape (or the lack of pores) on FBCs thickness, histological sections of explants were stained with Masson's trichrome, and thicknesses of FBCs were measured. The stained section examples are shown in figure 6.6.

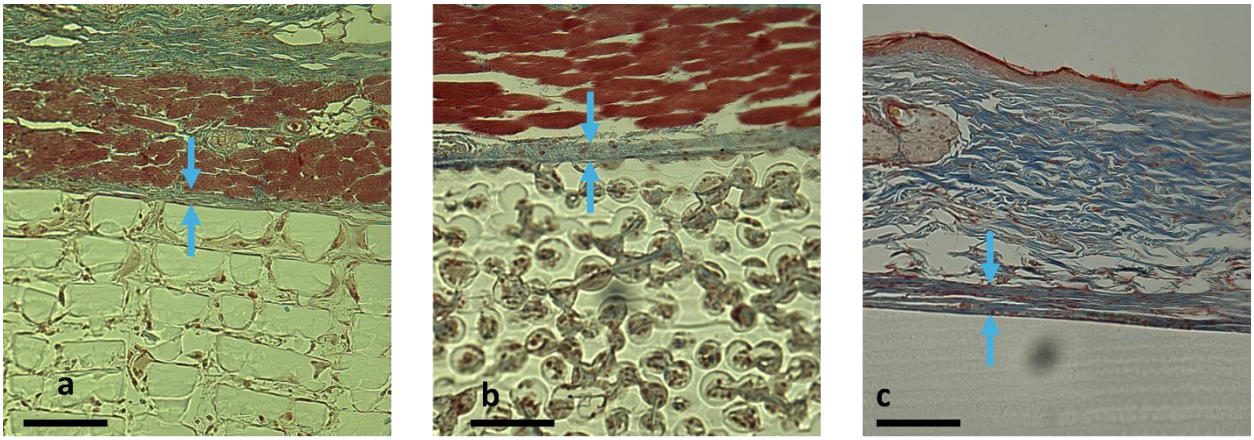

Figure 6.6. Representative microscope images of Masson's trichrome-stained sections for scaffolds with 40 µm cubical pores, 6S scaffolds with 40 µm spherical pores, and non-porous scaffolds are displayed in panels (a), (b), and (c), respectively, and the FBCs are pointed by blue arrows (scale bar = 100 µm).

Collagen layers (blue) surrounding both cubical (Fig. 6.6 a) and spherical (Fig. 6.6 b) porous scaffolds appear to be thinner and less dense, compared to the typical FBC surrounding solid implant (Fig. 6.6 c) characterized by a denser and thicker collagen layer. The reduced blue staining indicates lower collagen levels. This observation suggests a good capacity for both porous scaffolds to mitigate the FBR.

The average thickness of the FBC surrounding the scaffolds, based on biological replicates (Fig. 3d1), was measured at 37.1 ± 6.8 µm (n=8) for cubical pore scaffolds, 35.3 ± 18.3 µm (n=4) for spherical pore scaffolds, and 55.5 ± 10.8 µm (n=3) for non-porous scaffolds. The distribution of all FBC thickness measurements is illustrated in Fig. 3d2, providing a comprehensive representation of the data. Notably, the FBC surrounding the solid implants was substantially thicker than that of the cubical pore scaffolds and the spherical pore scaffolds, although there is no statistical difference was found within the 3 scaffold types, primarily due to the limited number of samples.

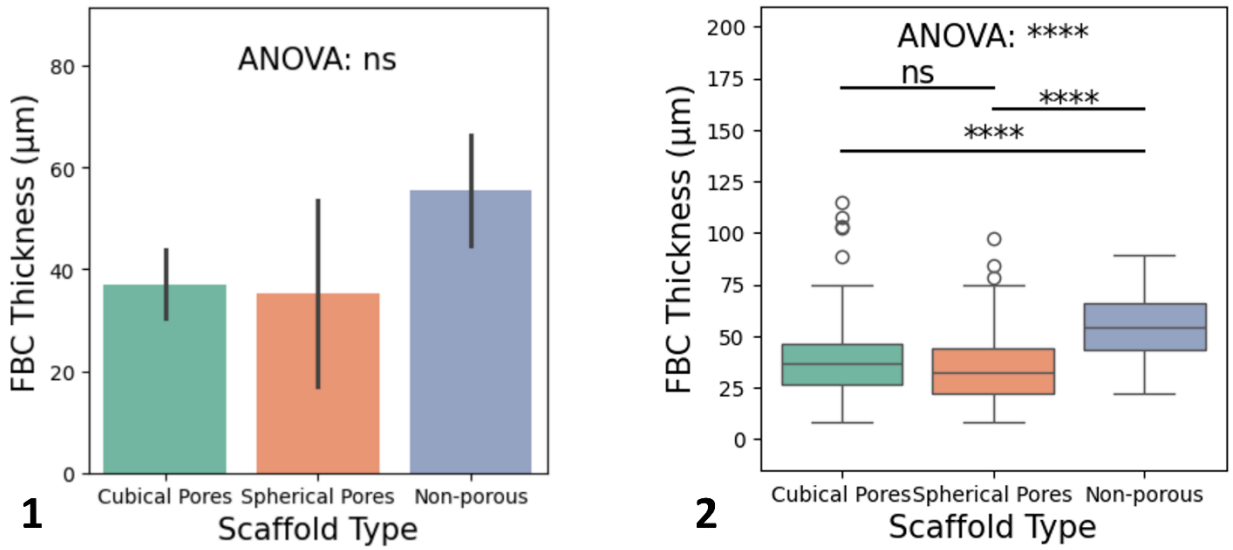

Figure 6.7. The statistical analysis results for FBC thickness, where 1 is based on biological replicates, and 2 shows the distribution of all measurements (technical replicates), indicates that there is statistical difference between the porous scaffolds and the solid implants based on all the measurement results, and there is no statistical difference between 2 porous scaffolds.

Although the ANOVA test did not show statistical significance when comparing the three scaffold types, the average FBC thickness reveals that the solid implants had an FBC thickness approximately 1.5 times greater than that of the scaffolds with 40 µm cubical pores, indicating a

substantial difference between these scaffold types. Previous research has consistently shown that scaffolds with 40 μm spherical pores reduce FBC thickness compared to solid implants[63, 65]. This further supports the conclusion that scaffolds with 40 μm cubical pores have the potential to mitigate FBC formation, given their similar response to the spherical pore scaffolds.

Focusing on the distribution box plot in Fig. 6.7.2, which encompasses all collected samples (6 measurements from each tissue section, with 3 sections per implant), both porous structures exhibit a reduction in FBC thickness compared to solid implants, and shows a statistical difference between difference scaffold types. While Fig. 6.7.2 shows that the main distribution of FBC thickness for porous implants is lower than that of solid implants, some measurements indicate relatively thick FBCs (>100 μm). This observation highlights that FBC formation is influenced not only by implant structure but also by other factors[65]. Analysis of outlier data points reveals that most are closer to the edges of the implants, where sharp corners may contribute to FBC formation. A thicker FBC can help to mitigate the damage caused by the sharpness of these edges, resulting in a smoother overall surface that may reduce discomfort for the mice. However, most of the data falls within a small range with normal distribution, demonstrating the reliability of the measurements.

6.3.3 *3D printed scaffolds reduce collagen level around implant*

To better evaluate the FBC, the color information of the skin, topside FBC, and underside FBC were measured, and the CI value (normalized blue and green intensity) were calculated according to Formula 6.1.

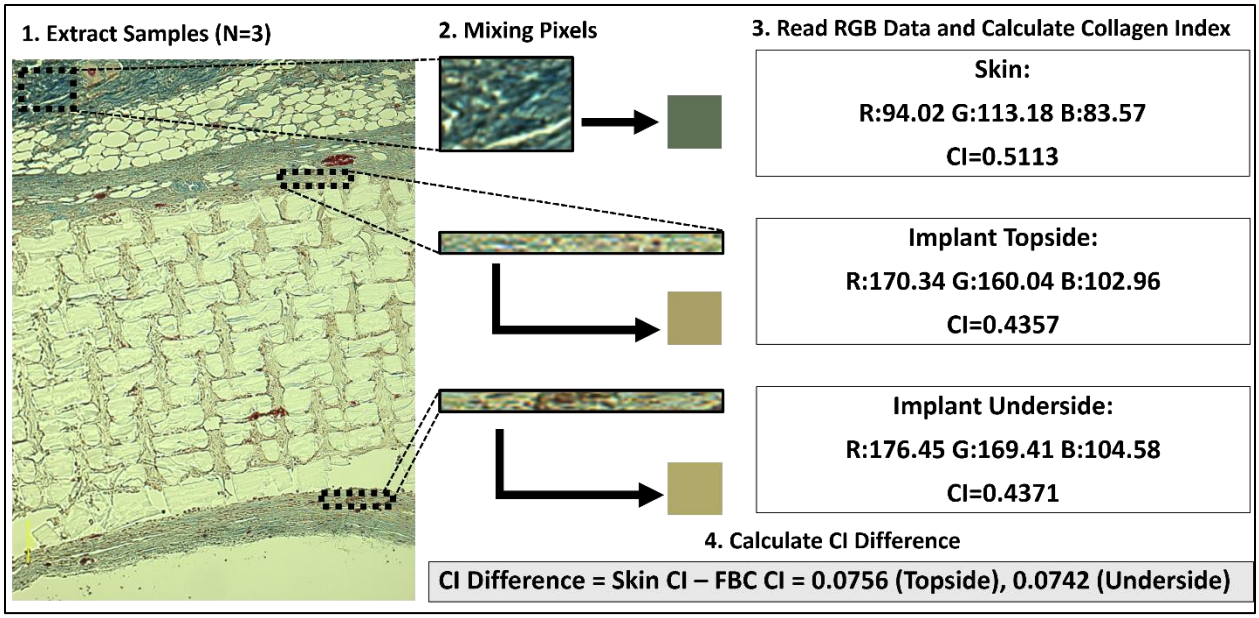

Figure 6.8. Schematic diagram illustrating the calculation of the CI and the CI difference

To isolate the effect of host collagen level, we use the CI difference (skin CI minus the FBC CI) here to perform a better comparative analysis. The skin CI is also collected on the same tissue section to ensure the staining conditions remain the same. The formula is shown in Formula 6.2.

Since the skin normally contains a higher density of collagen than the FBC, when using the CI difference to evaluate FBR extent, a higher CI difference indicates a lower level of collagen in the FBC.

The CI has been used in a previously published report[97], it provides a normalized value reflecting the proportion of collagen in the tissue. By using a ratio of blue and green (collagen) to the total color spectrum (including red, representing other tissue components), it accounts for variations in staining intensity and provides a consistent measure across different samples.

A higher collagen index indicates a greater proportion of collagen in the tissue surrounding the implant, suggesting a more pronounced FBR. This can be interpreted as an increased fibrotic response and potentially a greater degree of encapsulation.

Our study goes beyond simply analyzing the CI within the FBC. We focus on the transition of collagen levels from the surrounding skin tissue to the tissue immediately adjacent to the implant, and that's the main reason we calculated the CI difference. A larger difference in CI between these two regions indicates a mitigation of collagen deposition around the implant, suggesting that the implant surface possesses properties that reduce the fibrotic response. This approach provides a more nuanced understanding of the implant's impact on collagen deposition and its potential for improved biocompatibility.

The quantitative comparisons of the CI difference between the 3 implant groups (cubical porous scaffold, spherical porous scaffold, and non-porous slab) in terms of the topside collagen and underside collagen are shown in Figures 6.9 and 6.10, respectively.

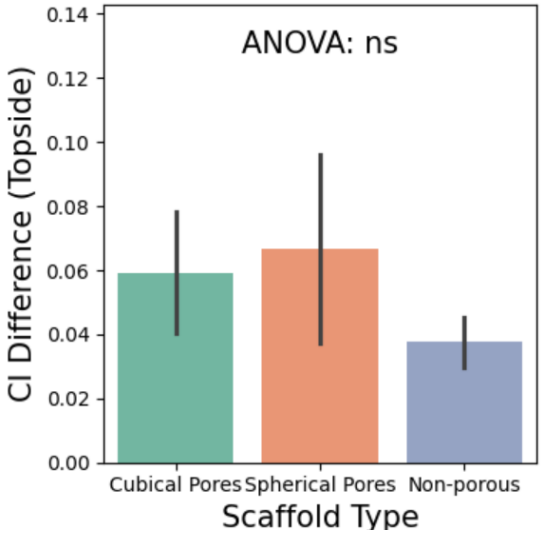

Figure 6.9. Statistical analysis of the CI difference between the skin and topside FBC based on biological replicates

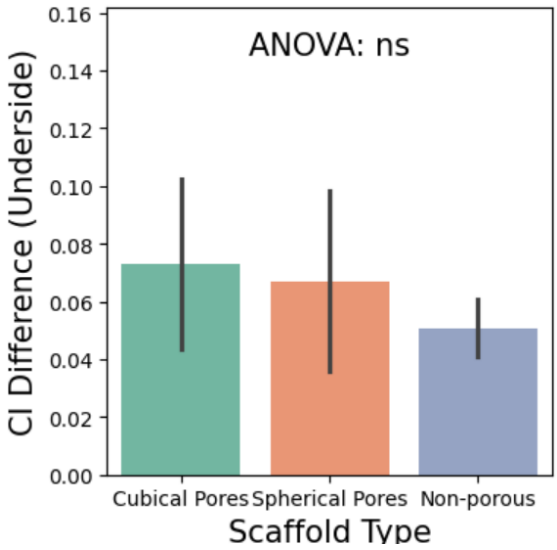

Figure 6.10. Statistical analysis of the CI difference between the skin and underside FBC based on biological replicates.

The CI differences for both porous scaffolds are substantially higher than that of the solid implant. This result indicates that the porous structure can reduce the collagen level of the FBC, and demonstrates that the collagen levels around both porous scaffolds are lower than that of the classical FBC around the solid implants, which is more close to the collagen level of the skin.

It is important to note that the CI is theoretically an indicator for evaluating collagen levels. However, since the red component in the overall color index does not correlate with collagen, its inclusion in the CI calculation as a normalization factor may actually reduce the accuracy of assessing collagen density. Despite this limitation, because it normalizes the overall collagen content, we continue to utilize it as an index in this context. Further discussions are needed to explore its potential applications.

The FBC is a critical indicator of biocompatibility, aligning with the modern definition of biocompatibility as “the ability of a material to locally trigger and guide host proteins and cells toward non-fibrotic, vascularized reconstruction and functional tissue integration.”[62] After 28

days of implantation, the FBR typically reaches its final stage, marked by the development of the FBC (or fibrous capsule)[14]. This fibrous capsule is generally avascular[104], and its presence hinders integration with surrounding tissue—an outcome often desired for most biomaterials.

Previous studies have shown that precision porous implants with 40 μm spherical pores promote the formation of a thin capsule while facilitating abundant vascularization within the pores. These implants also demonstrate high compatibility with local tissue, with minimal collagenous growth, unlike solid implants, which tend to form a thick, dense FBC[65]. This dense capsule acts as a barrier, potentially defunctionalizing biomaterials with solid surfaces. The collagen levels observed in our study, which indicate a similar response between 2 porous implants, suggest that regardless of pore geometry, 40 μm pores can effectively reduce fibrous capsule formation and mitigate collagen deposition around the implants, which aligns with existing literature demonstrating the positive impact of increased porosity and surface area on tissue integration and the reduction of fibrous capsule formation around porous scaffolds[105]. While these results are preliminary, they suggest that cubical pores, which are more easily and rapidly fabricated using 3D printing techniques compared to spherical pores and traditional fabrication methods, may offer significant advantages in mitigating the foreign body response. This observation highlights the potential of 3D-printed scaffolds with cubical pore geometries to enhance biocompatibility and promote successful tissue integration.

6.3.4 *3D printed scaffolds promote cell infiltration*

To assess cellularization of implants, histology sections were stained with H&E and were quantified using ImageJ.

From representative H&E stained sections (Fig.6.11 a-c and Fig. 6.12), we can observe that the cells are able to grow all the way through both cubical and spherical porous implants. The

percentage of the area occupied by mature tissue ingrowth (characterized by pink staining section area) is almost the same in the two different porous scaffolds, indicating reconstructive healing in porous scaffolds, regardless of pore geometries.

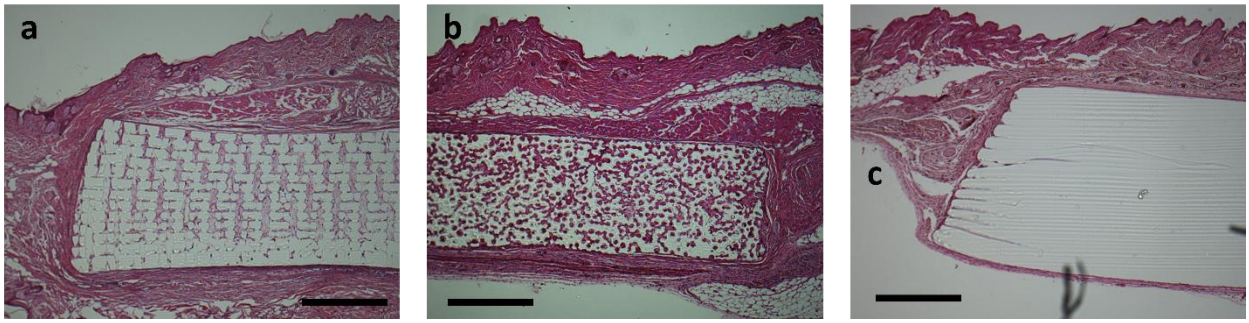

Figure 6.11. (a), (b), and (c) are the representative images of the H&E stained section of the scaffold with 40 µm cubical pores, the 6S scaffold with 40um spherical pores, and the non-porous scaffold respectively, showing both porous scaffolds have the ingrowth rate close to around 100% (scale bar = 500 µm)

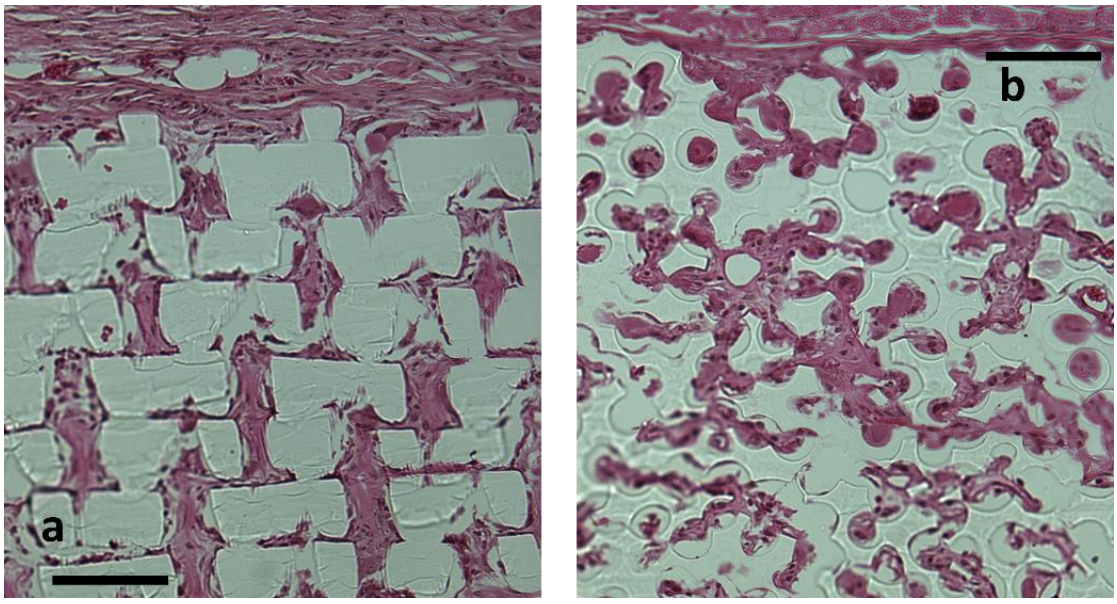

Figure 6.12. representative images of the H&E stained section of the scaffold with 40um cubical pores (a), the 6S scaffold with 40um spherical pores showing its cellular ingrowth (b) (scale bar = 100 µm)

By comparing the H & E staining results and the Masson's trichrome results, we can see both porous scaffold's inner structures have pink staining in H & E, but no blue or less dense blue in the trichrome staining. This suggests that the in pore pink areas are not or lower collagen or fibrous connective tissue, and this indicates a reduced FBR in the porous scaffolds. By comparing with the dense layer around the non-porous scaffold, the absence of significant collagen deposition and reduced signs of a chronic foreign body reaction indicate the porous scaffolds triggered a shift from a pro-inflammatory to pro-healing response. Lack of collagen ingrowth demonstrates that instead of forming a collagen barrier, the surrounding tissues directly integrate with the implant, and this is a sign that the implants are more biocompatible compared with the solid implant, and capable of supporting healing rather than triggering ongoing inflammation.

The nuclei density in ingrowth areas in porous scaffolds is shown in Fig. 6.13, where the nuclei density for cubical porous scaffolds is 1990.9 ± 409.9 nuclei/mm^2, and for spherical porous scaffolds is 2449.6 ± 105.8 nuclei/mm^2. Although there is no statistical difference between the different pore geometries, the p value we calculated is 0.057, showing that it is close to have a significant difference between the different pore geometries. We can also see the spherical pores have slightly higher nuclei density compared with cubical pores base on the plot. This may indicate the spherical geometry of the pores is slightly more potent in attracting cells growth. But since there is no significant statistical difference, and by comparing the data with our previous research, we believe the nuclei density within both cubical pores and spherical pores are relatively comparable. This rigorous cells have infiltration of the pores demonstrates that the scaffolds are pro-healing. The body is not isolating the implant from the rest of the body.

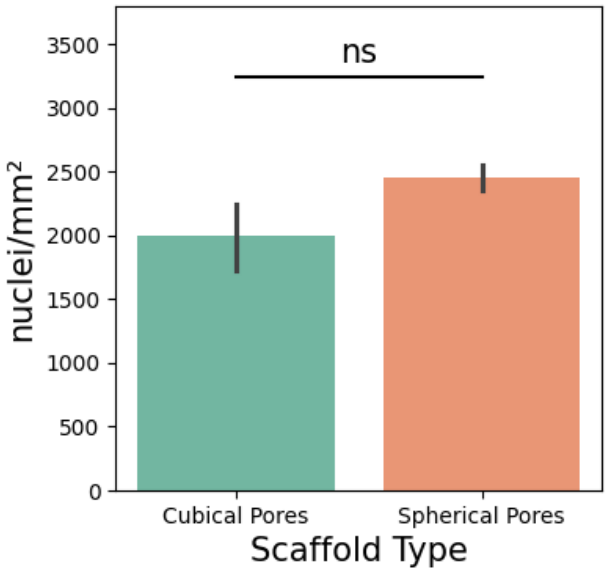

Figure 6.13. statistical analyzation of the nuclei in two different pore geometries

A porous structure with a high nuclei density within its pores typically indicates tissue integration rather than FBC encapsulation, as observed in solid implants[106]. Cells infiltrating the scaffold's pores contribute to matrix deposition and tissue remodeling, progressively filling the scaffold with native tissue over time. This level of cellular integration is generally advantageous for long-term scaffold functionality, particularly in tissue engineering applications where the scaffold is intended to integrate with surrounding tissue. These observations support the hypothesis that the porous scaffold with a 40 µm pore size promotes a pro-healing environment, regardless of pore geometry.

6.3.5 *3D printed scaffolds enable blood vessel ingrowth*

The H&E results already demonstrate that both porous scaffolds have high level of cell infiltration and in-pore nuclei densities. Angiogenesis, or the ingrowth of blood vessels is crucial in enabling nutrient and oxygen exchange within the scaffold, supporting sustained cell viability and potentially aiding in tissue regeneration.

As shown in Fig. 6.14, ingrowth capillaries (tubular structures containing a large number of red blood cells, indicated by red arrows) were observed in both porous scaffolds with different pore geometries. In the cubical pore scaffolds, some capillaries were located more than 400 µm from the nearest edge, with red blood cells present, indicating growth toward the central area of the implant. This demonstrates that capillaries can successfully grow into the cubical pore scaffolds, supporting tissue regeneration, and may also have the potential to promote angiogenesis throughout the majority of the scaffold.

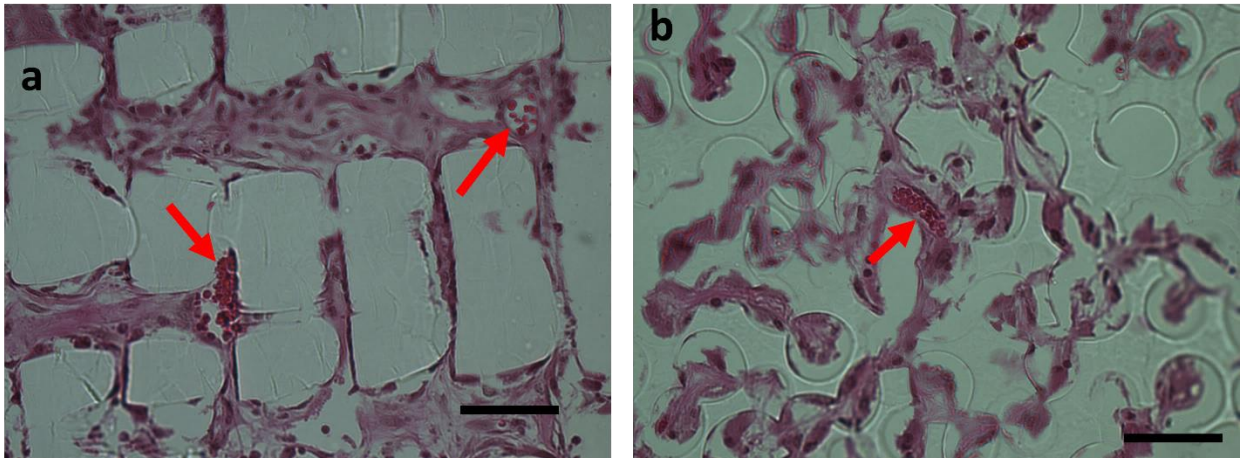

Figure 6.14. H&E evidence of vascularization deep inside both types of scaffolds. Representative images of H&E-stained sections for the scaffold with 40 µm cubical pores (a) and the 6S scaffold with 40 µm spherical pores (b), respectively, illustrating the scaffolds' ability to support vascular ingrowth (indicated by red arrows) (scale bar = 50 µm).

When using 3D printing to fabricate porous scaffolds, surface pore sizes are typically larger than 100 µm, which often leads to the formation of a dense fibrous capsule and poor angiogenesis[107, 108]. While different materials can mitigate FBC formation[109, 110], these approaches are limited by the specific properties of the materials and are not broadly applicable. In contrast, our result shown in both Fig. 3a and 5a indicate that scaffolds with 40 µm cubical

pores not only reduced FBC thickness but also promoted cellular and vascular ingrowth. Solid implants made from the same material resulted in thicker FBCs, demonstrating that 40 μm cubical pores can effectively reduce the FBR without the need for specialized materials. This highlights their potential for broader applications, including biomedical devices and organ regeneration[111].

One of the main reasons for researches to investigate porous scaffolds is the interconnected pores has the potential for vascularization. Its importance stems from its fundamental role in delivering oxygen and nutrients to cells, while simultaneously removing metabolic waste products[89]. Without an adequate blood supply, engineered tissues or implanted devices cannot survive or integrate effectively with the host's body. Previous reports suggest that, in the absence of supporting capillaries, oxygen and nutrients can only penetrate up to approximately 150-200 μm[85]. However, this distance can be significantly increased with scaffolds featuring 40 μm cubical pores, as they can support vascular ingrowth extending at least 400 μm.

Moreover, blood vessels actively participate in cell signaling and tissue integration by transporting growth factors, hormones, and immune cells, fostering communication between the implant and the host[112], and macrophages are one of the key immune cells involved in the FBR. Previous studies have shown that macrophages tend to polarize into the M2 phenotype when infiltrating 40 μm spherical pores, a process linked to enhanced vascular ingrowth and the induction of a pro-healing response within the pore[35]. Further study in our scaffold with cubical pores to quantify macrophage phenotypes would provide valuable insights.

Our data indicate that both porous scaffolds with 40 μm cubical and spherical pores can induce vascular ingrowth, regardless of pore geometry. This finding, consistent with previous studies on porous biomaterials, highlights the potential of cubical porous scaffolds for developing biomedical devices with reduced FBR and enhanced tissue integration[12, 35, 62, 113]. By encouraging the

ingrowth of blood vessels, scaffolds or devices with 40 μm cubical pores should be capable of reducing the risk of device failure due to poor integration or inflammation, ultimately leading to better patient outcomes and fewer complications[114]. This, along with the observed vascular ingrowth, demonstrates that 40 μm cubical pores hold high potential in the biomedical field.

6.4 CONCLUSIONS

Porous scaffolds exhibit substantial potential for reducing foreign body reaction and supporting tissue regeneration, particularly the porous scaffold with 40 μm interconnected spherical pores. In this chapter, we used vat photopolymerization 3D printing to fabricate porous scaffolds with 40 μm interconnected cubical pores to emulate this pro-healing effect. Chemically identical 3D printed cubical porous scaffolds, traditionally fabricated spherical porous scaffolds, and non-porous slabs were then implanted subcutaneously in mice to compare cellular responses. The porous scaffold with 40 μm cubical pores demonstrated performance comparable to the scaffold with 40 μm spherical pores, effectively reducing FBC thickness and the collagen density within the FBC, compared to non-porous slabs. Within the pores, both cubical and spherical pore structures with a size of 40 μm facilitate rigorous cellular ingrowth and supported vascularization, indicating the high biocompatibility of the cubical porous scaffold.

A porous, biocompatible scaffold fabricated using the versatile 3D printing has high potential for customized tissue engineering and regenerative medicine applications. The ability to fabricate this scaffold into various shapes allows for tailored designs that accommodate specific anatomical structures, making it ideal for personalized implants and complex scaffold architectures. This combination of biocompatibility, porosity, and shape adaptability positions it as a valuable platform-technology for advancing patient-specific therapies, improving healing outcomes, and fostering innovation in both soft and hard tissue repair solutions.

Chapter 7. FUTURE PLANS

7.1 PRINTING 6S SCAFFOLD WITH HIGH-RESOLUTION CLIP

As discussed in Chapter 3, the collaboration with DeSimone lab has demonstrated the potential to print 6S scaffolds. Therefore, this will be prioritized as the first task of future work. Successful printing of 6S scaffolds will lead to the animal study of these scaffolds.

7.2 VERIFYING THE SURFACE CONTAMINATION HYPOTHESIS

As discussed in Chapter 4, we have hypothesized that surface contamination cannot be ignored if the laser dose is lower than a certain amount. New experiments might need to be conducted to test this hypothesis.

7.3 TESTING AND ANALYZING PHOTO-CURING FORMULATIONS

As discussed in Chapter 5, the performance of PEGDMA-based resins is still being evaluated. The development of a high-resolution resin in the future will allow for the printing of porous scaffolds and the initiation of *in vivo* studies.

7.4 MACROPHAGE POLARIZATION TEST

As discussed in Chapter 6, the polarization of macrophages within the scaffold can influence the foreign body response (FBR) in different directions, including pro-inflammatory and pro-healing pathways. In this context, quantifying the polarization rate of macrophages can provide valuable insights into the cellular performance and overall response to the scaffold.

Chapter 8. ACKNOWLEDGEMENTS

It's surreal—I can hardly believe I'm about to complete my PhD. From the beginning, I never anticipated how challenging this journey would be. I received my PhD offer from the University of Washington on April 15, 2020 (yea the last day~), while still completing my master's degree there. It was the early days of the COVID-19 pandemic in the U.S. To celebrate, I ordered four dishes from the only open Chinese restaurant within walking distance, ate, and cried. I'd just broken up, and I remember trying to convince my partner that I'd stay in Seattle and we could still be together—obviously, it didn't work out. In hindsight, that moment hinted at the tough road my PhD would become.

Starting a PhD during a pandemic was anything but easy. For one, I could only meet with my PI, Dr. Buddy D. Ratner, over Zoom. Buddy's calm, reassuring presence and vast knowledge are powerful in person, but something was lost over video—the vibe, perhaps? Or maybe it was my anxiety with English over a screen; it seemed harder to communicate.

He assigned me my project, a novel approach to 3D printing biomaterials, was incredibly exciting but required access to our 3D printer, a beautiful machine stationed in our lab—a lab I had limited access to due to COVID restrictions. Our lab manager, Sharon Creason, organized a sign-in system to minimize contact. She's not just a manager but the linchpin of the Ratner lab, maintaining structure and bridging the gaps when Buddy is busy. Sharon's expertise in animal studies has also been invaluable; nearly all ongoing animal research in our lab involves her input. During the pandemic, she managed everything, keeping us compliant, afloat, and healthy, until I brought the first COVID case to the group on January 19, 2022—Buddy's 75th birthday. We'd gathered to present Buddy with drawings we'd made as gifts, and the next day, I realized I was sick. Fortunately, due to Sharon's strict protocols, no one else in the lab got infected.

One person I did unknowingly infect, however, was my close friend, Bo Yuan (原博). Bo is a lifelong friend (not just because he's now a millionaire), and though he never mentioned his infection, I'm sure he'd remind me of it someday, perhaps over dinner—though I'd pretend to pay and leave! Bo supported me through my prelim, my general exam, and my struggle with severe depression. I couldn't have gotten through it all without him. But still, I would not pay the check.

We survived the pandemic, and I still remember the day I went to sign in, only to see Sharon's bold note: "NO LOGGING REQUIRED." It felt like time had blurred during those years. But I clearly recall the graduation of several lab members, including my mentor, Dr. Lars Crawford, and Dr. Le Zhen, who left an impressive legacy, designing the original structure for my research and setting up critical protocols. Their pioneering work is an essential part of my project's foundation.

Globally, the pandemic came to an end, along with the most challenging relationship of my life—a time I could not have endured without the support of my cat, GuoGuo (锅锅). Though the details are now blurred, my college friends Lixu Huang (黄丽旭), Weiwei Li (李薇薇), and Lin Gan (甘霖) had warned me about its toxicity—they were right, and I was an idiot, leaving my own research behind. I remember they supported me as I nearly failed my transport course late 2018, and I know they'll continue to be there, whether in China, Australia, or the UK.

During these years, I learned a great deal from Dr. Runbang Tang, Dr. Julia King, Dr. Prabhleen Kaur, and Dr. Sherry Liu, the first few PhD graduates from our lab after the pandemic. They joined the lab a couple of years before me, and I benefited immensely from their experiences on how to be a PhD, as my PhD life was still struggling.

If I count 2018, the year I joined UW as a master's student, as the start of my project, it took four years until I reached significant milestones in 2022, now Chapters 2 and 4 of my dissertation. That year, my PhD trajectory felt clearer, and I completed my first first-author paper. I also had

the chance to mentor an undergraduate, Adia Kirkham, who contributed to Chapter 5. I feel sorry for might not be able to finish this as a paper, but her work was crucial to that chapter's existence.

In early 2023, I collaborated with Dr. Joseph DeSimone at Stanford, a leader in 3D printing. This ongoing collaboration is incredibly meaningful, and I hope to continue it, perhaps through my master's student, Yuto Koga, who will further develop my work in Chapter 3 and 6.

In March 2023, I passed my general exam with the support of a remarkable committee: Dr. Buddy Ratner, Dr. David Bergsman, Dr. Jorge Marchand, and Dr. Jonathan Liu. Their insights removed critical obstacles and guided me through the final stages of my PhD. My journey would have been significantly harder without them.

Summer 2023 was unforgettable, thanks to Yi Zhang (张怡), one of my closest friends, with whom I traveled all around Seattle. My research also gained momentum, with support from my labmates, Dr. Kan Wu and Kyung-Hoon Kim. I' ve lost count of the nights we spent working together, only to end up at Haidilao for late-night hotpot, making the most of our student discount.

Our lab was also making great progress, establishing a great research enviroment, alongside Shijie Zhang, Dr. Meghan Wyatt, and of course, Louis Chen—our little academic brother.

Then I met Charlie. Everything seemed to shift into high gear. With his encouragement (and occasional nudging), I secured an internship and return offer from Intel, completed my animal study and second paper, and now, I'm on the brink of earning my PhD—all within one year. His energy and support feel like that of a driven family member.

At the end of 2023, I finally have a chance returned to China, reuniting with my bros Tingxi Wu (吴庭熙), Xuanyou Lin (林炫佑), and Guanxuan Li (李冠轩), and my family—my father Jinshui Chen (陈金水), my mother Shangdi Chen (陈上弟), and my sister Danxia Chen (陈丹霞). Their support has been my strength over the years.

The acknowledgments section is the last chapter I wirte of my dissertation, and writing it brings a sense of closure but also sadness, as I realize it marks the end of my student life. While I'm grateful for all the amazing people I mentioned here and their love, I find it hard to say goodbye. Each name mentioned in these acknowledgments has been pivotal in my PhD journey and in my life; I'll never forget them.

But as with all things, my PhD life must come to an end, just as my dissertation does.

Before the end, I want to express gratitude for the financial support of the Center for Dialysis Innovation (CDI), funded by the Northwest Kidney Center, and to the Departments of Chemical Engineering and Bioengineering at the University of Washington for their steadfast support.

Finally, Buddy, I just want to say that being one of your students has truly been one of the luckiest and most meaningful experiences of my life. Thank you for welcoming me into the group and guiding me through these transformative six years.

Thank you all for helping make my challenging PhD journey a little easier.

谢谢。

(PS: Yes, it's exactly 100 pages.)

Chapter 9. REFERENCES

[1] J.B. Park, R.S. Lakes, Introduction to biomaterials, Biomaterials, Springer1992, pp. 1-6.
[2] J. Park, R.S. Lakes, Biomaterials: an introduction, Springer Science & Business Media2007.
[3] T. Goda, T. Shimizu, K. Ishihara, Bioinspired biomaterials for soft contact lenses, (2015).
[4] Evans, S. Lewin, Factors affecting pull-out strength of cannulated cancellous bone screws, (2009).
[5] Chen, Xingyu, Yang, Dongqiong, Functional zwitterionic biomaterials for administration of insulin.
[6] A.R. Nectow, K.G. Marra, D.L. Kaplan, Biomaterials for the Development of Peripheral Nerve Guidance Conduits, Tissue Engineering Part B Reviews 18(1) (2012) 40-50.
[7] C.M. Bidan, K.P. Kommareddy, M. Rumpler, P. Kollmannsberger, P. Fratzl, J.W.C. Dunlop, Geometry as a Factor for Tissue Growth: Towards Shape Optimization of Tissue Engineering Scaffolds, Advanced Healthcare Materials (2012).
[8] G. Khang, S.J. Lee, M.S. Kim, H.B. Lee, Biomaterials: tissue engineering and scaffolds, Encyclopedia of Medical devices and instrumentation (2006).
[9] L. Zhen, B. Ratner, Precision-engineered Porous Material with Tunable Mechanical Property for Vascular Graft Application, 2016.
[10] F. Likibi, M. Assad, C. Coillard, G. Chabot, C. Rivard, Bone integration and apposition of porous and non porous metallic orthopaedic biomaterials, Annales de chirurgie, 2005, pp. 235-241.
[11] M. Sari, P. Hening, I.D. Ana, Y. Yusuf, Bioceramic hydroxyapatite-based scaffold with a porous structure using honeycomb as a natural polymeric Porogen for bone tissue engineering, Biomaterials research 25(1) (2021) 1-13.
[12] E.L. Calleros, F.I. Simonovsky, S. Garty, B.D. Ratner, Crosslinked, biodegradable polyurethanes for precision-porous biomaterials: Synthesis and properties, Journal of Applied Polymer Science 137(25) (2020) 48943.
[13] B.D. Ratner, A.S. Hoffman, F.J. Schoen, J.E. Lemons, Biomaterials science: an introduction to materials in medicine, Elsevier2004.
[14] B.N. Brown, B.D. Ratner, S.B. Goodman, S. Amar, S.F. Badylak, Macrophage polarization: an opportunity for improved outcomes in biomaterials and regenerative medicine, Biomaterials 33(15) (2012) 3792-3802.
[15] J.E. Sanders, S.E. Lamont, A. Karchin, S.L. Golledge, B.D. Ratner, Fibro-porous meshes made from polyurethane micro-fibers: effects of surface charge on tissue response, Biomaterials 26(7) (2005) 813-818.
[16] T. Bertrand, J. Peixinho, S. Mukhopadhyay, C.W. Macminn, Dynamics of swelling and drying in a spherical gel, Physical Review Applied (2016).
[17] A. Bobbio, The first endosseous alloplastic implant in the history of man, Bulletin of the History of Dentistry 20(1) (1972) 1.
[18] S. Newsom, The history of infection control: Joseph Lister, British Journal of Infection Control 3(2) (2002) 21-23.
[19] J.M. Anderson, Biocompatibility and bioresponse to biomaterials, Principles of regenerative medicine, Elsevier2019, pp. 675-694.
[20] Y. Su, I. Cockerill, Y. Wang, Y.-X. Qin, L. Chang, Y. Zheng, D. Zhu, Zinc-based biomaterials for regeneration and therapy, Trends in biotechnology 37(4) (2019) 428-441.

[21] S.V. Murphy, A. Atala, Organ engineering–combining stem cells, biomaterials, and bioreactors to produce bioengineered organs for transplantation, Bioessays 35(3) (2013) 163-172.
[22] B.D. Ratner, Biomaterials science: an interdisciplinary endeavor, Biomaterials science, Academic Press1996, pp. 1-8.
[23] S. Liu, Y.-Y. Xie, B. Wang, Role and prospects of regenerative biomaterials in the repair of spinal cord injury, Neural regeneration research 14(8) (2019) 1352.
[24] A. De Mel, B.G. Cousins, A.M. Seifalian, Surface modification of biomaterials: A quest for blood compatibility, International journal of biomaterials 2012 (2012).
[25] M. Rubert, J.R. Vetsch, I. Lehtoviita, M. Sommer, F. Zhao, A.R. Studart, R. Müller, S. Hofmann, Scaffold pore geometry influences bone-like tissue formation in dynamic cell culture conditions, bioRxiv (2020) 2020.04.24.060525.
[26] J.M. Anderson, S. Jiang, Implications of the acute and chronic inflammatory response and the foreign body reaction to the immune response of implanted biomaterials, The Immune Response to Implanted Materials and Devices: The Impact of the Immune System on the Success of an Implant (2017) 15-36.
[27] R. Trindade, T. Albrektsson, P. Tengvall, A. Wennerberg, Foreign body reaction to biomaterials: on mechanisms for buildup and breakdown of osseointegration, Clinical implant dentistry and related research 18(1) (2016) 192-203.
[28] J.M. Anderson, A. Rodriguez, D.T. Chang, Foreign body reaction to biomaterials, Seminars in immunology, Elsevier, 2008, pp. 86-100.
[29] J. Li, S. Li, C. Van Blitterswijk, K. De Groot, A novel porous Ti6Al4V: characterization and cell attachment, Journal of Biomedical Materials Research Part A: An Official Journal of The Society for Biomaterials, The Japanese Society for Biomaterials, and The Australian Society for Biomaterials and the Korean Society for Biomaterials 73(2) (2005) 223-233.
[30] T. Guo, J. Zhao, J. Chang, Z. Ding, H. Hong, J. Chen, J. Zhang, Porous chitosan-gelatin scaffold containing plasmid DNA encoding transforming growth factor-β1 for chondrocytes proliferation, Biomaterials 27(7) (2006) 1095-1103.
[31] E.S. Bayrak, H. Mehdizadeh, B. Akar, S.I. Somo, E.M. Brey, A. Cinar, Agent-based modeling of osteogenic differentiation of mesenchymal stem cells in porous biomaterials, 2014 36th Annual International Conference of the IEEE Engineering in Medicine and Biology Society, IEEE, 2014, pp. 2924-2927.
[32] S.T. Koshy, D.J. Mooney, Biomaterials for enhancing anti-cancer immunity, Current opinion in biotechnology 40 (2016) 1-8.
[33] A. Sienkiewicz, P. Krasucka, B. Charmas, W. Stefaniak, J. Goworek, Swelling effects in cross-linked polymers by thermogravimetry, Journal of Thermal Analysis and Calorimetry 130(1) (2017) 85-93.
[34] A.J. Parnell, S.J. Martin, C.C. Dang, M. Geoghegan, R.A.L. Jones, C.J. Crook, J.R. Howse, A.J. Ryan, Synthesis, characterization and swelling behaviour of poly(methacrylic acid) brushes synthesized using atom transfer radical polymerization, Polymer 50(4) (2009) 1005-1014.
[35] E.M. Sussman, M.C. Halpin, J. Muster, R.T. Moon, B.D. Ratner, Porous Implants Modulate Healing and Induce Shifts in Local Macrophage Polarization in the Foreign Body Reaction, Annals of Biomedical Engineering 42(7) (2014) 1508-1516.
[36] Y.-C. Chiu, J.C. Larson, A. Isom Jr, E.M. Brey, Generation of porous poly (ethylene glycol) hydrogels by salt leaching, Tissue Engineering Part C: Methods 16(5) (2010) 905-912.

[37] S.B. Lee, Y.H. Kim, M.S. Chong, S.H. Hong, Y.M. Lee, Study of gelatin-containing artificial skin V: fabrication of gelatin scaffolds using a salt-leaching method, Biomaterials 26(14) (2005) 1961-1968.
[38] M. Gravel, R. Vago, M. Tabrizian, Use of natural coralline biomaterials as reinforcing and gas-forming agent for developing novel hybrid biomatrices: microarchitectural and mechanical studies, Tissue Engineering 12(3) (2006) 589-600.
[39] Y. Tang, S. Lin, S. Yin, F. Jiang, M. Zhou, G. Yang, N. Sun, W. Zhang, X. Jiang, In situ gas foaming based on magnesium particle degradation: A novel approach to fabricate injectable macroporous hydrogels, Biomaterials 232 (2020) 119727.
[40] H. Zhong, J. Huang, J. Wu, J. Du, Electrospinning nanofibers to 1D, 2D, and 3D scaffolds and their biomedical applications, Nano Research 15(2) (2022) 787-804.
[41] Z. Fereshteh, Freeze-drying technologies for 3D scaffold engineering, Functional 3D tissue engineering scaffolds, Elsevier2018, pp. 151-174.
[42] C.N. Kelly, A.T. Miller, S.J. Hollister, R.E. Guldberg, K. Gall, Design and structure–function characterization of 3D printed synthetic porous biomaterials for tissue engineering, Advanced healthcare materials 7(7) (2018) 1701095.
[43] F. Bartolomeu, N. Dourado, F. Pereira, N. Alves, G. Miranda, F.S. Silva, Additive manufactured porous biomaterials targeting orthopedic implants: A suitable combination of mechanical, physical and topological properties, Materials Science and Engineering: C 107 (2020) 110342.
[44] H.N. Chia, B.M. Wu, Recent advances in 3D printing of biomaterials, Journal of biological engineering 9(1) (2015) 4.
[45] R. Owen, C. Sherborne, R. Evans, G.C. Reilly, F. Claeyssens, Combined porogen leaching and emulsion templating to produce bone tissue engineering scaffolds, International journal of bioprinting 6(2) (2020).
[46] C. Schubert, M.C. Van Langeveld, L.A. Donoso, Innovations in 3D printing: a 3D overview from optics to organs, British Journal of Ophthalmology 98(2) (2014) 159-161.
[47] A. Bandyopadhyay, S. Bose, S. Das, 3D printing of biomaterials, MRS bulletin 40(2) (2015) 108-115.
[48] N.H.M. Yusoff, L.-R.I. Teo, S.J. Phang, V.-L. Wong, K.H. Cheah, S.-S. Lim, Recent advances in polymer-based 3D printing for wastewater treatment application: an overview, Chemical Engineering Journal 429 (2022) 132311.
[49] C. Buchanan, L. Gardner, Metal 3D printing in construction: A review of methods, research, applications, opportunities and challenges, Engineering Structures 180 (2019) 332-348.
[50] H. Baniasadi, E. Kimiaei, R.T. Polez, R. Ajdary, O.J. Rojas, M. Österberg, J. Seppälä, High-resolution 3D printing of xanthan gum/nanocellulose bio-inks, International Journal of Biological Macromolecules 209 (2022) 2020-2031.
[51] G. Varghese, M. Moral, M. Castro-García, J.J. López-López, J.R. Marín-Rueda, V. Yagüe-Alcaraz, L. Hernández-Afonso, J.C. Ruiz-Morales, J. Canales-Vázquez, Fabrication and characterisation of ceramics via low-cost DLP 3D printing, Boletín de la Sociedad Española de Cerámica y Vidrio 57(1) (2018) 9-18.
[52] J. Creff, R. Courson, T. Mangeat, J. Foncy, S. Souleille, C. Thibault, A. Besson, L. Malaquin, Fabrication of 3D scaffolds reproducing intestinal epithelium topography by high-resolution 3D stereolithography, Biomaterials 221 (2019) 119404.
[53] A.K. Nguyen, R.J. Narayan, Two-photon polymerization for biological applications, Materials Today 20(6) (2017) 314-322.

[54] D. Dean, J. Wallace, A. Siblani, M.O. Wang, K. Kim, A.G. Mikos, J.P. Fisher, Continuous digital light processing (cDLP): Highly accurate additive manufacturing of tissue engineered bone scaffolds: This paper highlights the main issues regarding the application of Continuous Digital Light Processing (cDLP) for the production of highly accurate PPF scaffolds with layers as thin as 60 μm for bone tissue engineering, Virtual and physical prototyping 7(1) (2012) 13-24.
[55] B.J. Lee, K. Hsiao, G. Lipkowitz, T. Samuelsen, L. Tate, J.M. DeSimone, Characterization of a 30 μm pixel size CLIP-based 3D printer and its enhancement through dynamic printing optimization, Additive Manufacturing 55 (2022) 102800.
[56] F. Zheng, B. Derby, J. Wong, Fabrication of microvascular constructs using high resolution electrohydrodynamic inkjet printing, Biofabrication 13(3) (2021) 035006.
[57] W. Jamróz, J. Szafraniec, M. Kurek, R. Jachowicz, 3D printing in pharmaceutical and medical applications–recent achievements and challenges, Pharmaceutical research 35(9) (2018) 176.
[58] D.R. Smalley, C.W. Hull, Method of making a three dimensional object by stereolithography, Google Patents, 1992.
[59] P.J. Bártolo, I. Gibson, History of stereolithographic processes, Stereolithography, Springer2011, pp. 37-56.
[60] F.P. Melchels, J. Feijen, D.W. Grijpma, A review on stereolithography and its applications in biomedical engineering, Biomaterials 31(24) (2010) 6121-6130.
[61] S. Maruo, K. Ikuta, Submicron stereolithography for the production of freely movable mechanisms by using single-photon polymerization, Sensors and Actuators A: Physical 100(1) (2002) 70-76.
[62] L. Crawford, M. Wyatt, J. Bryers, B. Ratner, Biocompatibility evolves: phenomenology to toxicology to regeneration, Advanced healthcare materials 10(11) (2021) 2002153.
[63] L.R. Madden, D.J. Mortisen, E.M. Sussman, S.K. Dupras, J.A. Fugate, J.L. Cuy, K.D. Hauch, M.A. Laflamme, C.E. Murry, B.D. Ratner, Proangiogenic scaffolds as functional templates for cardiac tissue engineering, Proceedings of the National Academy of Sciences 107(34) (2010) 15211-15216.
[64] W. Teng, T.J. Long, Q. Zhang, K. Yao, T.T. Shen, B.D. Ratner, A tough, precision-porous hydrogel scaffold: ophthalmologic applications, Biomaterials 35(32) (2014) 8916-8926.
[65] L. Zhen, S.A. Creason, F.I. Simonovsky, J.M. Snyder, S.L. Lindhartsen, M.M. Mecwan, B.W. Johnson, J. Himmelfarb, B.D. Ratner, Precision-porous polyurethane elastomers engineered for application in pro-healing vascular grafts: Synthesis, fabrication and detailed biocompatibility assessment, Biomaterials 279 (2021) 121174.
[66] H. Gong, M. Beauchamp, S. Perry, A.T. Woolley, G.P. Nordin, Optical approach to resin formulation for 3D printed microfluidics, RSC advances 5(129) (2015) 106621-106632.
[67] M. Pagac, J. Hajnys, Q.-P. Ma, L. Jancar, J. Jansa, P. Stefek, J. Mesicek, A review of vat photopolymerization technology: materials, applications, challenges, and future trends of 3D printing, Polymers 13(4) (2021) 598.
[68] B.D. Ratner, The biocompatibility of implant materials, Host response to biomaterials, Elsevier2015, pp. 37-51.
[69] Z.L. Wescoe, Synthesis of Degradable poly-HEMA Hydrogels for Tissue Engineering, 2018.
[70] G. Chen, A High-resolution 3D Printable Porous Biomaterial, University of Washington2020.

[71] J.R. Tumbleston, D. Shirvanyants, N. Ermoshkin, R. Janusziewicz, A.R. Johnson, D. Kelly, K. Chen, R. Pinschmidt, J.P. Rolland, A. Ermoshkin, Continuous liquid interface production of 3D objects, Science 347(6228) (2015) 1349-1352.
[72] K. Hsiao, B.J. Lee, T. Samuelsen, G. Lipkowitz, J.M. Kronenfeld, D. Ilyn, A. Shih, M.T. Dulay, L. Tate, E.S. Shaqfeh, Single-digit-micrometer-resolution continuous liquid interface production, Science Advances 8(46) (2022) eabq2846.
[73] G. Lipkowitz, T. Samuelsen, K. Hsiao, B. Lee, M.T. Dulay, I. Coates, H. Lin, W. Pan, G. Toth, L. Tate, Injection continuous liquid interface production of 3D objects, Science advances 8(39) (2022) eabq3917.
[74] F.J. O'Brien, Biomaterials & scaffolds for tissue engineering, Materials Today 14(3) (2011) 88–95.
[75] C. Curti, D.J. Kirby, C.A. Russell, Current formulation approaches in design and development of solid oral dosage forms through three-dimensional printing, Progress in Additive Manufacturing 5(2) (2020) 111-123.
[76] E.M. Maines, M.K. Porwal, C.J. Ellison, T.M. Reineke, Sustainable advances in SLA/DLP 3D printing materials and processes, Green Chemistry 23(18) (2021) 6863-6897.
[77] C. Mendes-Felipe, J. Oliveira, I. Etxebarria, J.L. Vilas-Vilela, S. Lanceros-Mendez, State-of-the-art and future challenges of UV curable polymer-based smart materials for printing technologies, Advanced Materials Technologies 4(3) (2019) 1800618.
[78] J. Fu, L. Wang, H. Yu, M. Haroon, F. Haq, W. Shi, B. Wu, L. Wang, Research progress of UV-curable polyurethane acrylate-based hardening coatings, Progress in Organic Coatings 131 (2019) 82-99.
[79] R. Palucci Rosa, G. Rosace, Nanomaterials for 3D printing of polymers via stereolithography: Concept, technologies, and applications, Macromolecular Materials and Engineering 306(10) (2021) 2100345.
[80] G. Burke, D.M. Devine, I. Major, Effect of stereolithography 3D printing on the properties of PEGDMA hydrogels, Polymers 12(9) (2020) 2015.
[81] I. Chiulan, E.B. Heggset, S.I. Voicu, G. Chinga-Carrasco, Photopolymerization of bio-based polymers in a biomedical engineering perspective, Biomacromolecules 22(5) (2021) 1795-1814.
[82] A. Bagheri, J. Jin, Photopolymerization in 3D printing, ACS Applied Polymer Materials 1(4) (2019) 593-611.
[83] D.G. Castner, B.D. Ratner, Proteins controlled with precision at organic, polymeric, and biopolymer interfaces for tissue engineering and regenerative medicine, Principles of Regenerative Medicine (2019) 523-534.
[84] R. Klopfleisch, Macrophage reaction against biomaterials in the mouse model–Phenotypes, functions and markers, Acta biomaterialia 43 (2016) 3-13.
[85] N. Annabi, J.W. Nichol, X. Zhong, C. Ji, S. Koshy, A. Khademhosseini, F. Dehghani, Controlling the Porosity and Microarchitecture of Hydrogels for Tissue Engineering, Tissue Engineering Part B: Reviews 16(4) (2010) 371-383.
[86] F. Bartolomeu, N. Dourado, F. Pereira, N. Alves, G. Miranda, F. Silva, Additive manufactured porous biomaterials targeting orthopedic implants: A suitable combination of mechanical, physical and topological properties, Materials Science and Engineering: C 107 (2020) 110342.
[87] F. Bobbert, K. Lietaert, A.A. Eftekhari, B. Pouran, S. Ahmadi, H. Weinans, A. Zadpoor, Additively manufactured metallic porous biomaterials based on minimal surfaces: A unique

combination of topological, mechanical, and mass transport properties, Acta biomaterialia 53 (2017) 572-584.
[88] J.D. Bryers, C.M. Giachelli, B.D. Ratner, Engineering biomaterials to integrate and heal: the biocompatibility paradigm shifts, Biotechnology and bioengineering 109(8) (2012) 1898-1911.
[89] J.L. Hernandez, K.A. Woodrow, Medical applications of porous biomaterials: features of porosity and tissue-specific implications for biocompatibility, Advanced healthcare materials 11(9) (2022) 2102087.
[90] Â. Semitela, A.F. Girão, C. Fernandes, G. Ramalho, I. Bdikin, A. Completo, P.A. Marques, Electrospinning of bioactive polycaprolactone-gelatin nanofibres with increased pore size for cartilage tissue engineering applications, Journal of Biomaterials Applications 35(4-5) (2020) 471-484.
[91] C.M. Brougham, T.J. Levingstone, N. Shen, G.M. Cooney, S. Jockenhoevel, T.C. Flanagan, F.J. O'Brien, Freeze-drying as a novel biofabrication method for achieving a controlled microarchitecture within large, complex natural biomaterial scaffolds, Advanced healthcare materials 6(21) (2017) 1700598.
[92] R. Trombetta, J.A. Inzana, E.M. Schwarz, S.L. Kates, H.A. Awad, 3D printing of calcium phosphate ceramics for bone tissue engineering and drug delivery, Annals of biomedical engineering 45 (2017) 23-44.
[93] P. Ahangar, M.E. Cooke, M.H. Weber, D.H. Rosenzweig, Current biomedical applications of 3D printing and additive manufacturing, Applied sciences 9(8) (2019) 1713.
[94] P. Yogesh, P. Richa, N.S. Chandrashekhar, K.P. Karunakaran, Layer Separation Mechanisms in DLP 3D Printing, in: M.S. Shunmugam, M. Kanthababu (Eds.) Advances in Additive Manufacturing and Joining, Springer Singapore, Singapore, 2020, pp. 179-187.
[95] T.F. Hady, B. Hwang, A. Pusic, R.L. Waworuntu, M. Mulligan, B. Ratner, J.D. Bryers, Uniform 40-μm-pore diameter precision templated scaffolds promote a pro-healing host response by extracellular vesicle immune communication, Journal of tissue engineering and regenerative medicine 15(1) (2021) 24-36.
[96] A.D. Tjandra, T. Heywood, R. Chandrawati, Trigit: A free web application for rapid colorimetric analysis of images, Biosensors and Bioelectronics: X 14 (2023) 100361.
[97] M. Ibrahim, J. Bond, M.A. Medina, L. Chen, C. Quiles, G. Kokosis, L. Bashirov, B. Klitzman, H. Levinson, Characterization of the Foreign Body Response to Common Surgical Biomaterials in a Murine Model, Eur J Plast Surg 40(5) (2017) 383-392.
[98] G.J. Tortora, B.H. Derrickson, Principles of anatomy and physiology, John Wiley & Sons2018.
[99] X.-M. Wang, Z.-Y. Qiu, H. Cui, Mineralized Collagen Bone Graft Substitutes, Woodhead Publishing2019.
[100] F. Bobbert, A. Zadpoor, Effects of bone substitute architecture and surface properties on cell response, angiogenesis, and structure of new bone, Journal of Materials Chemistry B 5(31) (2017) 6175-6192.
[101] T. Jiao, R. Zhou, J. Jiao, J. Jiao, Q. Lian, Extrusion/Inkjet Printing of Verteporfin-Loaded Bilayer Skin Substitutes for Wound Healing and Structure Reconstruction, Journal of Bionic Engineering (2024).
[102] F. Girard, C. Lajoye, M. Camman, N. Tissot, F. Berthelot Pedurand, B. Tandon, D. Moedder, I. Liashenko, S. Salameh, P.D. Dalton, First Advanced Bilayer Scaffolds for Tailored Skin Tissue Engineering Produced via Electrospinning and Melt Electrowriting, Advanced Functional Materials (2024) 2314757.

[103] A.P. Dhand, M.D. Davidson, H.M. Zlotnick, T.J. Kolibaba, J.P. Killgore, J.A. Burdick, Additive manufacturing of highly entangled polymer networks, Science 385(6708) (2024) 566-572.
[104] A. Ravin, K. Olbrich, L. Levin, A.L. Usala, B. Klitzman, Long-and short-term effects of biological hydrogels on capsule microvascular density around implants in rats, Journal of Biomedical Materials Research: An Official Journal of The Society for Biomaterials, The Japanese Society for Biomaterials, and The Australian Society for Biomaterials and the Korean Society for Biomaterials 58(3) (2001) 313-318.
[105] J.D. Drews, V.K. Pepper, C.A. Best, J.M. Szafron, J.P. Cheatham, A.R. Yates, K.N. Hor, J.C. Zbinden, Y.-C. Chang, G.J. Mirhaidari, Spontaneous reversal of stenosis in tissue-engineered vascular grafts, Science translational medicine 12(537) (2020) eaax6919.
[106] J. Kim, W.A. Li, W. Sands, D.J. Mooney, Effect of pore structure of macroporous poly (lactide-co-glycolide) scaffolds on the in vivo enrichment of dendritic cells, ACS applied materials & interfaces 6(11) (2014) 8505-8512.
[107] W. Li, F. Dai, S. Zhang, F. Xu, Z. Xu, S. Liao, L. Zeng, L. Song, F. Ai, Pore Size of 3D-Printed Polycaprolactone/Polyethylene Glycol/Hydroxyapatite Scaffolds Affects Bone Regeneration by Modulating Macrophage Polarization and the Foreign Body Response, ACS Applied Materials & Interfaces 14(18) (2022) 20693-20707.
[108] Q. Zhang, Z. Xu, X. Zhang, C. Liu, R. Yang, Y. Sun, Y. Zhang, W. Liu, 3D Printed High-Strength Supramolecular Polymer Hydrogel-Cushioned Radially and Circumferentially Oriented Meniscus Substitute, Advanced Functional Materials 32(23) (2022) 2200360.
[109] R. Duan, Y. Wang, D. Su, Z. Wang, Y. Zhang, B. Du, L. Liu, X. Li, Q. Zhang, The effect of blending poly (l-lactic acid) on in vivo performance of 3D-printed poly(l-lactide-co-caprolactone)/PLLA scaffolds, Biomaterials Advances 138 (2022) 212948.
[110] E. Kim, Y.S. Petronyuk, N. Guseynov, S. Tereshchuk, A. Popov, A. Volkov, V. Gorshenev, A. Olkhov, V. Levin, A. Dymnikov, Biocompatibility and bioresorption of 3D-printed polylactide and polyglycolide tissue membranes, Bulletin of Experimental Biology and Medicine 170 (2021) 356-359.
[111] S. Agarwal, S. Saha, V.K. Balla, A. Pal, A. Barui, S. Bodhak, Current developments in 3D bioprinting for tissue and organ regeneration–a review, Frontiers in Mechanical Engineering 6 (2020) 589171.
[112] K. Gaengel, G. Genové, A. Armulik, C. Betsholtz, Endothelial-mural cell signaling in vascular development and angiogenesis, Arteriosclerosis, thrombosis, and vascular biology 29(5) (2009) 630-638.
[113] P.C.S. Bota, A.M.B. Collie, P. Puolakkainen, R.B. Vernon, E.H. Sage, B.D. Ratner, P.S. Stayton, Biomaterial topography alters healing in vivo and monocyte/macrophage activation in vitro, Journal of Biomedical Materials Research Part A 95A(2) (2010) 649-657.
[114] C.R. Arciola, D. Campoccia, L. Montanaro, Implant infections: adhesion, biofilm formation and immune evasion, Nature Reviews Microbiology 16(7) (2018) 397-409.